

File ID 105737
Filename Thesis

SOURCE (OR PART OF THE FOLLOWING SOURCE):

Type Dissertation
Title Cold electroweak baryogenesis and quantum cosmological correlations
Author M.P. van der Meulen
Faculty Faculty of Science
Year 2008
Pages x, 171

FULL BIBLIOGRAPHIC DETAILS:

<http://dare.uva.nl/record/272514>

Copyright

It is not permitted to download or to forward/distribute the text or part of it without the consent of the author(s) and/or copyright holder(s), other than for strictly personal, individual use.

COLD ELECTROWEAK BARYOGENESIS
AND
QUANTUM COSMOLOGICAL CORRELATIONS

COLD ELECTROWEAK BARYOGENESIS
AND
QUANTUM COSMOLOGICAL CORRELATIONS

ACADEMISCH PROEFSCHRIFT

ter verkrijging van de graad van doctor

aan de Universiteit van Amsterdam

op gezag van de Rector Magnificus

prof. dr. D.C. van den Boom

ten overstaan van een door het college voor promoties

ingestelde commissie,

in het openbaar te verdedigen in de Agnietenkapel

op woensdag 7 mei 2008, te 12.00 uur

door

MEINDERT PIETER VAN DER MEULEN

geboren te Gouda

PROMOTIECOMMISSIE

PROMOTOR

prof. dr. J. Smit

OVERIGE LEDEN

prof. dr. ir. F.A. Bais

prof. dr. J. de Boer

prof. dr. E.L.M.P. Laenen

prof. dr. E.P. Verlinde

dr. T. Prokopec

dr. K.E. Schalm

dr. A. Tranberg

FACULTEIT DER NATUURWETENSCHAPPEN, WISKUNDE EN INFORMATICA



This work is part of the research program of the “Stichting voor Fundamenteel Onderzoek der Materie (FOM)”, which is financially supported by the “Nederlandse Organisatie voor Wetenschappelijk Onderzoek (NWO)”.

Cover design and illustrations by Haakon Brouwer (www.haakonbrouwer.com)

PUBLICATIONS

This thesis is based on the following publications:

- M. van der Meulen, D. Sexty, A. Tranberg and J. Smit,
Chern-Simons and winding number in a tachyonic electroweak transition,
JHEP **02** (2006) 029, [[arXiv:hep-ph/0511080](#)].
- M. van der Meulen and J. Smit,
Classical approximation to quantum cosmological correlations,
JCAP **11** (2007) 023, [[arXiv:0707.0842 \[hep-th\]](#)].

CONTENTS

Preface	1
I Cold Electroweak Baryogenesis	5
1 Introduction	7
1.1 Inflation and reheating	7
1.1.1 Inflation	7
1.1.2 Reheating	11
1.2 Baryogenesis	12
1.3 Cold Electroweak Baryogenesis	15
1.4 Outline	17
2 Standard Model	19
2.1 Action	19
2.1.1 Bosons	20
2.1.2 Fermions	21
2.2 Unitarity gauge	24
2.2.1 Higgs field	24
2.2.2 Gauge boson mass eigenstates	24
2.2.3 Fermion mass eigenstates	25
2.3 C and P transformations	26
2.4 Electroweak anomaly	28
2.4.1 Adler-Bell-Jackiw anomaly	28
2.4.2 Electroweak anomaly	29
2.5 Topology in the electroweak theory	31
2.5.1 Chern-Simons number N_{CS}	32
2.5.2 Higgs winding number N_w	33
2.5.3 Changing N_{CS} and N_w	33

3	Chern-Simons and winding number in Cold Electroweak Baryogenesis	35
3.1	Introduction	35
3.2	Winding in the $SU(2)$ Higgs model	37
3.2.1	$SU(2)$ Higgs model	38
3.2.2	Topology in the $SU(2)$ Higgs model	38
3.2.3	Sphaleron	40
3.2.4	Texture	40
3.2.5	Half-knot	41
3.3	Winding in the tachyonic transition	44
3.3.1	Tachyonic transition	44
3.3.2	Winding and Chern-Simons number densities	46
3.3.3	Early half-knots	46
3.3.4	Late half-knots	47
3.4	Numerical simulations	47
3.4.1	Setup	47
3.4.2	Results	48
3.4.3	Distributions and susceptibilities	54
3.5	Summary and discussion	56
4	CP violation	69
4.1	Introduction	69
4.2	CP violation in expansion in fields	70
4.2.1	Expansion in fields	70
4.2.2	CP violation	73
4.2.3	Validity of expansion in fields	74
4.3	CP violation in CEB	75
4.4	Comparison with derivative interaction	76
4.5	Discussion	76
5	Conclusions	79
II	Quantum cosmological correlations	81
6	Introduction	83
6.1	Cosmological perturbation theory	84
6.1.1	Scales	84
6.1.2	Degrees of freedom	85
6.1.3	Observations	87
6.2	Inflationary fluctuations	87
6.2.1	Quantum fluctuations in de Sitter space	87
6.2.2	Single field inflation	88

6.2.3	Multifield inflation	91
7	Classical approximation to quantum cosmological correlations	95
7.1	Introduction	95
7.2	Quantum theory	97
7.2.1	Closed Time Path formalism on a de Sitter background	98
7.2.2	Late times	103
7.3	Classical theory	108
7.3.1	Perturbative calculation of correlation functions	108
7.3.2	Graphical representation	110
7.4	Classical approximation	111
7.4.1	Small internal momenta	112
7.4.2	Large internal momenta	112
7.4.3	Classical approximation at one loop	113
7.4.4	Example	114
7.5	Discussion and conclusions	115
7.5.1	Early time contributions	115
7.5.2	Generalization to derivative interactions	116
7.5.3	Comparison to stochastic approach	117
7.5.4	Application to the curvature perturbation	120
7.5.5	Conclusions	121
8	Conclusions	123
A	Conventions	125
B	Free scalar field on a de Sitter background	127
B.1	Scalar wavefunction	127
B.2	Particle creation	128
B.3	Comparison with thermal field theory	129
C	Amputated diagrams with no external dashed lines	131
D	Correspondence between diagrams in quantum and classical theory	133
E	One loop correction to two point function	135
E.1	Diagrams A and D	135
E.1.1	Amputated diagram for small internal momenta	136
E.1.2	Amputated diagrams for large internal momenta	137
E.1.3	Attaching the external lines	143
E.2	Diagrams B and C	144
E.2.1	Amputated diagrams for small internal momenta	144

Contents

E.2.2	Amputated diagrams for large internal momenta	146
E.2.3	Attaching the external lines	148
Bibliography		149
Summary		163
Samenvatting		167
Dankwoord		171

PREFACE

High energy physics is the field of research in which the fundamental laws of nature are studied: the elementary particles and their interactions. Large accelerators, in which particles collide with speeds close to the speed of light, have given very precise experimental data. This culminated in the Standard Model of particle physics that describes all the known elementary particles and three of the four fundamental interactions between them.

A seemingly unrelated direction of science is cosmology in which space and time on the largest scales are studied with the goal to find out how the universe has become what it is and how it will develop further. Observations in this field have often been plagued by large uncertainties.

However, in the past decades the situation has changed substantially. New technologies, often involving space satellites, have transformed cosmology into a precision science. As such, cosmology provides a new window on high energy physics because many of the problems in cosmology are closely related to high energy physics. Developments in the fields of dark matter, dark energy, density fluctuations and many others do not only advance the field of cosmology but also that of high energy physics.

In this thesis two subjects in theoretical cosmology that are closely related to high energy physics are studied. The goal of the preface is to provide some background information that puts these two subjects in a broader framework. Much more information can be found in standard textbooks, such as references [1, 2, 3].

THE BIG BANG MODEL

According to the Big Bang model the universe is expanding. Initially the temperature and density were high, but due to the expansion the universe cooled down and became more and more dilute. This is widely accepted as a good description of the evolution of the universe. The first observational evidence for the Big Bang model was obtained by Hubble, who found that distant galaxies are moving away from us which indicates that space is expanding.

The process of cooling down triggered a cascade of events. Some of these events are:

- The electroweak phase transition. In this phase transition the electroweak symmetry was broken, which caused the weak interaction (which is responsible for nuclear fission) to be separated from the electromagnetic interaction. It took place at around 10^{-10} seconds after the Big Bang. This phase transition is important for the model that will be studied in part I.
- Nucleosynthesis. Nucleons (protons and neutrons) were bound together to form the nuclei of some of the chemical elements, such as helium, lithium, and others. This process occurred approximately three minutes after the Big Bang. The relative abundances of these elements have been calculated in the context of the Big Bang model, and were found to be consistent with the observed values. Therefore cosmologists are confident that the Big Bang model is valid at least from this moment onward. Any adjustments to the Big Bang model (like inflation, which will be discussed below) should have taken place before nucleosynthesis.
- Photon decoupling and atom formation. Electrons were bound to the nuclei to form neutral atoms. This took place at around 380 000 years after the Big Bang and caused the universe to become transparent. The radiation that was emitted at this moment is the Cosmic Microwave Background (CMB) radiation. This radiation is observed by satellite and balloon experiments which give us the earliest picture of the universe that we have. From this picture we know that the temperature of the universe at the time of photon decoupling was nearly the same in all directions. The observations of small fluctuations in the temperature have accelerated many developments in cosmology in the past 15 years. The CMB has yielded two Nobel prizes: in 1978 to Penzias and Wilson for its discovery, and in 2006 to Mather and Smoot for the measurements of the CMB using the COBE satellite [4].

INFLATION

The classic Big Bang model is very successful, but it also has some inherent problems. One of them is the flatness problem. From observations we know that the universe is to a good approximation flat (the spatial curvature vanishes), but according to the theory of general relativity this is not a stable situation: if the spatial curvature deviates only a small amount from zero, it will grow quickly. The only possible explanation for the current flatness of the universe is that the spatial curvature was initially extremely close to zero. However, such an initial condition requires a high degree of fine tuning.

The flatness problem and other problems can be solved by introducing a period of inflation, which is a period in which the universe is expanding at an accelerated rate (in contrast to the decelerating expansion in the classic Big Bang model). For example, for

the flatness problem one can show that during inflation the curvature is quickly driven to zero. Therefore a period of inflation can provide the desired initial conditions for a subsequent Big Bang phase.

At the end of inflation the universe is empty and cold. In order to return to a Big Bang phase the universe should be ‘reheated’. To not be in conflict with other observations, the reheating temperature should at least be above the temperature of nucleosynthesis.

Inflation plays an important role in current research in theoretical cosmology and also in this thesis.

BARYOGENESIS

Because the universe is empty at the end of inflation there are no baryons (which are the most important constituents of the matter we observe) and also no anti-baryons. Therefore the total baryon number B , which is the difference between the numbers of baryons and anti-baryons, is equal to zero.

In the current universe however we observe only matter and nearly no anti-matter. Thus B is nonzero, and there must have been a process after inflation (and before nucleosynthesis) in which this asymmetry was generated. This process is called baryogenesis. It is a quite nontrivial process, which is illustrated by the fact that up to now we have never witnessed a baryon number changing event in the laboratory. Many models of baryogenesis have been proposed in the past.

In the first part of this thesis a specific model is studied: *Cold Electroweak Baryogenesis*. It combines a model of inflation with a model of baryogenesis which takes place just after inflation, during the reheating process (which is called preheating in this particular model).

DENSITY FLUCTUATIONS

The solution to the flatness problem and the other problems of the classic Big Bang model was the original motivation for inflation. Nowadays the biggest virtue of inflation is considered to be the fact that it provides an explanation for the origin of the density fluctuations. These density fluctuations are the seeds from which the large scale structure (stars, galaxies, etc.) in the current universe has grown. They have been observed in the CMB with increasing precision by the COBE [4] and WMAP [5] satellites and other experiments.

The statistical properties of the fluctuations are characterized by their correlation functions. Because these correlation functions depend on what happened during inflation,

observations of the correlation functions provide a window into the physics of inflation. This is not only interesting from the point of view of cosmology, but also from the perspective of high energy physics, because inflation may have occurred at energy scales that are much higher than can ever be reached in the laboratory.

In the second part of this thesis we study the calculation of the cosmological correlation functions from inflation in quantum field theory. Many calculations have been done using classical field theory, and we estimate to what extent this gives a good approximation to the quantum calculations.



Part I

Cold Electroweak Baryogenesis

CHAPTER 1

INTRODUCTION

The origin of the matter–anti-matter asymmetry is a long-standing problem in cosmology. Over the course of time many baryogenesis models have been proposed, involving different branches of high energy physics such as quantum gravity, Grand Unifying Theories, supersymmetry, neutrino physics, and also electroweak physics. Models in the last class are called electroweak baryogenesis. In this part we study a variant of this class of models, namely Cold Electroweak Baryogenesis (CEB). It features inflation at the electroweak scale and, after this, electroweak symmetry breaking while the universe is still cold. During the symmetry breaking process, baryogenesis can take place.

In this chapter CEB is introduced, after (very) short reviews of inflation model building and baryogenesis.

1.1 INFLATION AND REHEATING

Some basic features of inflation model building and of reheating are reviewed. See for extensive reviews e.g. references [6, 7, 8].

1.1.1 INFLATION

In a spatially homogeneous and flat universe, the metric is of the Friedmann-Robertson-Walker (FRW) form:

$$ds^2 = -dt^2 + a(t)^2 d\mathbf{x}^2, \tag{1.1}$$

where a is the scale factor and \mathbf{x} is a comoving coordinate. Inflation is defined by the condition that there is accelerated expansion

$$\ddot{a} > 0, \quad (1.2)$$

where a dot denotes differentiation with respect to time t . In general relativity accelerated expansion can be caused by vacuum energy. The simplest way to introduce vacuum energy is by a cosmological constant, but then the phase of accelerated expansion would never end. Therefore one introduces a scalar field σ , called the inflaton, with a potential $V(\sigma)$ that can act as vacuum energy. The action is

$$S = \int d^4x \sqrt{-g} \left(\frac{1}{2} M_{\text{pl}}^2 R - \frac{1}{2} \partial_\mu \sigma \partial^\mu \sigma - V(\sigma) \right), \quad (1.3)$$

where M_{pl} is the reduced Planck mass defined by $M_{\text{pl}}^2 = 1/8\pi G_N$ with G_N the Newton constant. The classical equations of motion for a and σ can be derived from the action (1.3) which leads for spatially homogeneous σ to

$$3M_{\text{pl}}^2 H^2 = \frac{1}{2} \dot{\sigma}^2 + V(\sigma), \quad (1.4)$$

$$\dot{H} = -\frac{\dot{\sigma}^2}{2M_{\text{pl}}^2}, \quad (1.5)$$

$$0 = \ddot{\sigma} + 3H\dot{\sigma} + V'(\sigma), \quad (1.6)$$

where $H = \dot{a}/a$ is the Hubble constant, and where a prime denotes differentiation with respect to σ , so $V'(\sigma) = dV(\sigma)/d\sigma$. The third equation follows from the first two. From the second equation (1.5) one derives that there is accelerated expansion if $H^2 > \dot{\sigma}^2/2M_{\text{pl}}^2$.

Slow-roll parameters. One often uses slow-roll parameters to determine whether an inflaton potential V is suitable for (a considerable amount of) inflation. The first two slow-roll parameters are defined as

$$\epsilon \equiv \frac{1}{2} \left(\frac{M_{\text{pl}} V'}{V} \right)^2 \approx \frac{1}{2} \frac{\dot{\sigma}^2}{H^2 M_{\text{pl}}^2}, \quad (1.7)$$

$$\eta \equiv \frac{M_{\text{pl}}^2 V''}{V} \approx -\frac{\ddot{\sigma}}{H\dot{\sigma}} + \frac{1}{2} \frac{\dot{\sigma}^2}{H^2 M_{\text{pl}}^2}, \quad (1.8)$$

where we have used the equations of motion (1.4)-(1.6) to obtain the approximate expressions. For inflation the slow-roll parameters must be small: $\epsilon \ll 1$, $|\eta| \ll 1$ (slow-roll conditions).

E-folds. The amount of expansion between initial time t_i and final time t_f can be expressed by the number of e-folds $N(t_i, t_f)$, which is the logarithm of the fraction of the scale factors at the two times:

$$N(t_i, t_f) \equiv \ln \frac{a(t_f)}{a(t_i)} = \int_{t_i}^{t_f} H(t) dt. \quad (1.9)$$

During slow-roll inflation, we can write

$$H dt = \frac{H}{\dot{\sigma}} d\sigma \approx -\frac{V}{M_{\text{pl}}^2 V'} d\sigma = \mp \frac{1}{\sqrt{2\epsilon} M_{\text{pl}}} d\sigma, \quad (1.10)$$

where the sign depends on the direction in which σ rolls. From this expression it is clear that a smaller ϵ and a larger shift of σ during inflation lead to a larger number of e-folds. Typically it is assumed that the minimal required number of e-folds is approximately 50 to 60. However this number depends on some assumptions such as the scale at which inflation occurs; for low scale inflation this number can be as small as $N \approx 25$ [7].

Power spectrum. An important feature of inflation is that it can explain the origin of the density fluctuations that have led to the structure in the universe. This subject will be introduced in more detail in chapter 6. Here we just give the observational constraint on the most important characteristic of these fluctuations, namely the power spectrum of a quantity called the curvature perturbation ζ . In first approximation it is given by

$$\mathcal{P}_\zeta = \frac{1}{24\pi^2 M_{\text{pl}}^4} \frac{V}{\epsilon}, \quad (1.11)$$

which is to be evaluated at the time of horizon exit of the observable modes (see also chapter 6). This power spectrum is nearly flat (independent of k). The deviation from flatness is quantified by the spectral index, defined by

$$n - 1 \equiv \frac{d \ln \mathcal{P}_\zeta}{d \ln k} \approx -6\epsilon + 2\eta, \quad (1.12)$$

which is also evaluated at horizon exit. The values that follow from observations are [9]

$$\mathcal{P}_\zeta \approx 24.10^{-10}, \quad n \approx 0.95, \quad (1.13)$$

at the so-called pivot scale $k_{\text{pivot}} = 0.002/\text{Mpc}$.

Example: chaotic inflation. To illustrate the concepts introduced above, we consider here chaotic inflation [10], which is the simplest possible inflation model. It has a potential $V(\sigma) = m_\sigma^2 \sigma^2/2$. The slow-roll parameters (1.7) and (1.8) are given by

$$\epsilon = 2 \frac{M_{\text{pl}}^2}{\sigma^2}, \quad \eta = 2 \frac{M_{\text{pl}}^2}{\sigma^2}. \quad (1.14)$$

One finds from equations (1.9) and (1.10) that from the point that the inflaton field is $\sigma \approx \sqrt{4N}M_{\text{pl}}$, approximately N e-folds of inflation will follow. At this point, the slow-roll parameters are

$$\epsilon = \eta \approx \frac{1}{2N}, \quad (1.15)$$

and the power spectrum (1.11) is

$$\mathcal{P}_\zeta \approx \frac{N^2 m_\sigma^2}{6\pi^2 M_{\text{pl}}^2}. \quad (1.16)$$

Using $N = 50$ and the observational value (1.13) for the power spectrum, one obtains that m_σ should be of the order of $10^{-5}M_{\text{pl}}$. Then the energy density at the beginning of inflation is roughly $10^{-8}M_{\text{pl}}^4$. This is smaller than the Planck density and one does not expect that quantum gravity corrections are important. However this model is not well motivated from the point of view particle physics, because nonrenormalizable terms cannot be neglected for field values larger than M_{pl} . This is a typical problem for large field models with only one field. In small field models, and in models with multiple fields, this problem can be avoided.

Example: hybrid inflation. By introducing extra fields one can invent many more possible inflation models. An example with one extra field is hybrid inflation [11, 12, 13]. Consider the potential

$$V(\sigma, \phi) = V(\sigma) + V_0 + \frac{1}{2}(\lambda_{\sigma\phi}\sigma^2 - \mu^2)\phi^2 + \frac{\lambda}{4!}\phi^4, \quad (1.17)$$

where $V(\sigma)$ is a potential that supports inflation. $V(\sigma, \phi)$ is sketched in figure 1.1. Inflation takes place when σ takes values in the narrow, trough-like region at $\sigma > \mu/\sqrt{\lambda_{\sigma\phi}}$. The mass term of the effective potential for ϕ is positive and ϕ will have a vanishing expectation value. The period of inflation is effectively single field inflation and the power spectrum and slow-roll parameters are determined by the potential $V(\sigma) + V_0$. When the σ field rolls down and becomes smaller than $\mu/\sqrt{\lambda_{\sigma\phi}}$, the effective mass term of ϕ becomes negative and ϕ will start to roll down. Inflation will end at this point (if it has not ended before). The field ϕ is often called the waterfall field.

When ϕ rolls down there is often spontaneous symmetry breaking which can lead to the generation of topological defects.

This model can be adjusted such that the inflaton field rolls from small values towards larger values. Such a model is called ‘inverted hybrid inflation’ and is also used for CEB.

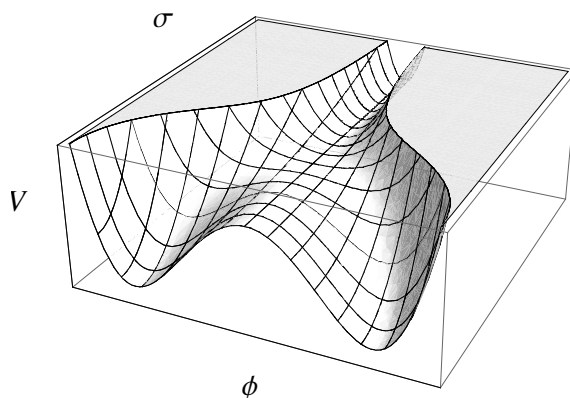


Figure 1.1: Sketch of the potential $V(\sigma, \phi)$ of hybrid inflation, as given in equation (1.17).

1.1.2 REHEATING

At the end of inflation the universe is empty and at zero temperature. To return to the Big Bang model, the energy in the inflaton field should somehow be transferred to the fields of the Standard Model.

In the original reheating scenario [14, 15, 16, 17, 18] the energy transfer occurs by the decay of inflaton particles into other particles. When the decay rate of the inflaton is higher than the Hubble rate H of the expansion of the universe, this process can generate a thermal state with a temperature that is called the reheating temperature.

There are many more possible mechanisms to drain the energy away from the inflaton field, often nonperturbative in nature. In some cases these mechanisms can transfer the energy much more quickly than in the original reheating scenario. Usually this does not directly result in a thermal state. Therefore these scenarios with fast energy transfers go under the name of preheating.

Several variations of preheating are possible. One of them, called resonant preheating [19, 20, 21, 22], is based on the coherent oscillation of the inflaton field about its vacuum. For suitable parameter values of the couplings of the inflaton field to other fields, there can be resonant particle production in certain momentum bands of the other fields. This can lead to a very efficient (partly) energy transfer from the inflaton field to the other fields.

Another preheating scenario is tachyonic preheating [23, 24, 25, 26, 27], that occurs in hybrid inflation models. In this case the energy is in the waterfall field and when it rolls down, it will transfer the energy to other fields. In [25] it was found that this occurs very rapidly, after only a few oscillations about the vacuum.

1.2 BARYOGENESIS

The observed baryon asymmetry of the universe is [28, 9]

$$\eta = \frac{n_b - n_{\bar{b}}}{n_\gamma} = (6.11 \pm 0.19) \times 10^{-10}, \quad (1.18)$$

where n_b , $n_{\bar{b}}$ and n_γ are the number densities of baryons, anti-baryons and photons. This number is constant as long as the evolution of the universe is adiabatic and a successful model of baryogenesis should be able to reproduce this asymmetry. In this section the basic conditions that a baryogenesis model should satisfy are discussed and electroweak baryogenesis is introduced. See [29, 30, 31, 32, 33] for reviews on (electroweak) baryogenesis.

THE SAKHAROV CONDITIONS AND THE STANDARD MODEL

It has long been known that any process of baryogenesis has to satisfy the three Sakharov conditions [34]:

- Violation of baryon number B (which is the number of baryons minus the number of anti-baryons) conservation. It is obvious that to create a baryon asymmetry, B must not be conserved.
- Violation of C and CP symmetries, where C is charge conjugation and P is parity transformation. If C is not violated ($[H, C] = 0$), we have:

$$\begin{aligned} \langle B \rangle(t) &= \text{Tr}(\rho(t)B) = \text{Tr}(e^{iHt}\rho(0)e^{-iHt}B) \\ &= \text{Tr}(C^{-1}Ce^{iHt}\rho(0)e^{-iHt}B) = -\langle B \rangle(t), \end{aligned} \quad (1.19)$$

and therefore $\langle B \rangle(t) = 0$. Here ρ is a general density matrix, and we have used $[\rho(0), C] = 0$ (the initial state is symmetric under C), the cyclic property of traces, and the fact that baryons are odd under the charge transformation: $CBC^{-1} = -B$ (this holds even for neutral baryons, see section 2.3). The same reasoning goes for CP , where one uses that baryons are even under parity conjugation $PBP^{-1} = B$.

- Deviation from thermal equilibrium. If the process would be in equilibrium, nothing would change and no baryons would be created.

These conditions are a first test for any model of baryogenesis. Of course, for such a model to be really responsible for the asymmetry (1.18) there are additional constraints: the right amount of asymmetry should be created, and the asymmetry should not be washed out by processes that take place at a later time (or the right amount should remain after a partial wash-out).

Many models for baryogenesis have been proposed. Often these models use physics beyond the Standard Model, i.e. particles and interactions that are not described by the Standard Model and that have not (yet) been observed, e.g. because the particles are too heavy to be created in particle colliders up to now. A popular way to extend the Standard Model is by introducing supersymmetry. This leads to many new interactions, that can both violate B conservation and C and CP symmetry. Another interesting possibility is to extend the lepton sector of the Standard Model, which makes it possible to have baryogenesis through leptogenesis [35].

It is intriguing that the Standard Model itself satisfies all the three Sakharov conditions [36]. In a different order than above:

- Deviation from equilibrium can occur during the electroweak phase transition¹. The core of the Standard Model is the electroweak theory (see chapter 2). This theory has a gauge symmetry that is spontaneously broken at low temperatures by the expectation value of the Higgs field. At high temperatures the symmetry is restored. Therefore when the universe cools down, there is a phase transition to the broken symmetry phase, at which moment there can be deviation from equilibrium. Models in which baryogenesis takes place during this electroweak phase transition fall in the class of electroweak baryogenesis models.
- Violation of B conservation. In the Standard Model baryon number is violated by a subtle quantum effect known as the electroweak anomaly (see section 2.4). One can assign a Chern-Simons number N_{CS} to a configuration of the electroweak gauge fields at a certain time. According to the electroweak anomaly a change in N_{CS} is related to a change in the baryon number B . In the broken phase there is an energy barrier that prevents N_{CS} from being easily changed. This is called the sphaleron barrier, after the configuration on the top of this barrier. It explains why we do not observe baryon violation in the laboratory. But in the symmetric phase, N_{CS} and B can easily be changed.
- C and CP violation. In the fermion sector of the Standard Model C and CP symmetries are violated. The latter effect is caused by the mixing of the three generations [37] (see also section 2.3). For the quarks the mixing is parameterized by the Cabibbo-Kobayashi-Maskawa (CKM) matrix, and for the leptons by the the Maki-Nakagawa-Sakata (MNS) matrix. The complex phase factors in these matrices cause CP violation.

However, electroweak baryogenesis using only Standard Model physics turns out not to work for two reasons: the deviation from equilibrium during the electroweak phase transition is not strong enough, and also the CP violation is estimated to be much too small.

¹The expansion of the universe also brings the universe out of equilibrium. However at electroweak scales, the expansion rate (1.4) is $H \approx 10^{-15}$ GeV and its effect is negligible.

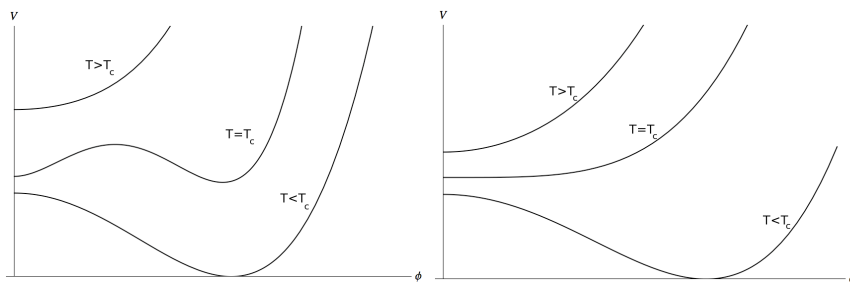


Figure 1.2: Sketch of the effective potentials $V(\phi, T)$ for temperatures above, at and below the critical temperature T_c , for a first order phase transition (left) and a smooth crossover (right).

We discuss these issues below.

THE ELECTROWEAK PHASE TRANSITION

The nature of the electroweak phase transition depends on the parameters of the theory, in particular on the Higgs mass m_H . Numerical simulations [38, 39, 40, 41, 42, 43, 44] have shown that there is a first order phase transition if $m_H \lesssim 72$ GeV. For a larger Higgs mass there is no phase transition but a smooth crossover.

If the phase transition is of first order, the effective potential for the Higgs field depends on the temperature as sketched in the left-hand side of figure 1.2: for decreasing temperatures a separate minimum develops that first represents a false vacuum, but becomes the true vacuum at temperatures below the critical temperature T_c . The phase transition proceeds by the formation of bubbles of the broken vacuum state that grow quickly for $T < T_c$. At the bubble walls there is a strong deviation from equilibrium.

In case of a smooth crossover, the effective Higgs potential depends on the temperature as in the right-hand side of figure 1.2: the minimum slowly moves from zero to nonzero values, and there is never a period in which there is a strong deviation from equilibrium.

The lower bound on the Higgs mass from the LEP experiment at CERN is $m_H > 114$ GeV [45]. Therefore the electroweak phase transition is a smooth crossover and the deviation from equilibrium is not enough to produce the baryon asymmetry (1.18).

CP VIOLATION

The other issue is that the CP violation from the fermion sector in the Standard Model is estimated to be much too small [46, 47]. It is believed to be proportional to

$$J \frac{(m_t^2 - m_c^2)(m_t^2 - m_u^2)(m_c^2 - m_u^2)(m_b^2 - m_s^2)(m_b^2 - m_d^2)(m_s^2 - m_d^2)}{\Lambda^{12}}, \quad (1.20)$$

where the m_i are the quark masses, Λ is an energy scale, and J is the Jarlskog invariant, which is the simplest rephasing invariant quantity that can be constructed from the CKM matrix V [48, 28]:

$$J = \sin^2 \theta_1 \sin \theta_2 \sin \theta_3 \cos \theta_1 \cos \theta_2 \cos \theta_3 \sin \delta = (3.08_{-0.18}^{+0.16}) \times 10^{-5}, \quad (1.21)$$

where the θ_i and δ are angles in the Kobayashi-Maskawa parameterization of V . The energy scale Λ is put in to construct a dimensionless number. One usually takes $\Lambda = 10^2$ GeV for the energy scale of the electroweak phase transition, which results² in an estimate of 10^{-19} . It is hard to imagine how such a small CP violating effect can lead to the asymmetry (1.18) which is of order 10^{-10} .

Of course it is still possible to extend the Standard Model such that both problems, the lack of deviation from equilibrium and the small CP violating effect, are avoided and baryogenesis can still take place during the electroweak phase transition. For example one can add another Higgs doublet [49, 50], consider supersymmetric extensions of the Standard Model (see citations in [33]), or consider corrections from nonrenormalizable operators [51]. We will consider yet another possibility: CEB.

1.3 COLD ELECTROWEAK BARYOGENESIS

THE ORIGINAL MODEL

CEB [52, 53] is a model that combines inflation and electroweak baryogenesis. It consists of the Standard Model together with one extra scalar field σ that plays the role of the inflaton field. σ is coupled to the Higgs field ϕ such that they together form a hybrid inflation model (1.17), where ϕ plays the role of the waterfall field. Hence during inflation the mass term of the Higgs potential has a positive sign, but as the inflaton rolls down and becomes smaller the sign changes and the Higgs field starts to roll down. This induces a process of tachyonic preheating. During this process the universe is strongly out of equilibrium and baryogenesis can take place.

²We use $m_u = 0.003$, $m_d = 0.006$, $m_s = 0.103$, $m_c = 1.24$, $m_b = 4.2$, $m_t = 175$ GeV.

If it works, this model is interesting for a number of reasons. First it combines inflation and baryogenesis in one model and it only needs one extra field apart from the Standard Model for this³. Hence this single extra field would simultaneously solve two important problems in cosmology.

Second it is interesting from the point of view of inflation model building because it has inflation at a much lower scale than most inflation models (see for example also [54, 55]). We will not pursue this direction further.

Third CEB is interesting from the point of view of baryogenesis model building, because it is a completely different model of electroweak baryogenesis than the models that existed before. This is the aspect we will be studying in the first part of this thesis.

DEVELOPMENT OF THE MODEL

After the first proposals in [52, 53] this model has been developed further. In [56] it was noticed that quantum corrections spoil the potential such that inflation is no longer possible. To avoid this problem an inverted hybrid inflation model was proposed in which the inflaton runs away from the origin and in which the quantum corrections are under control. Furthermore, two possible mechanisms for baryon production were mentioned in this paper. One is based on resonant oscillations about the new vacuum, and the other is based on the formation of topological defects.

In [57] this inverted hybrid inflation model was further worked out and its parameters were constrained by the WMAP data. The result is that the model, with fine-tuned parameters, is still allowed by observations. The potential used in [57] is

$$V(\sigma, \phi) = V_0 - \frac{1}{2}\alpha_2\sigma^2 + \frac{1}{4}\alpha_4\sigma^4 - \frac{1}{5}\alpha_5\sigma^5 + \frac{1}{6}\alpha_6\sigma^6 + \frac{1}{2}\left(\lambda_{\sigma\phi}\sigma^2\phi^2 - \frac{1}{2}\mu^2\right)\phi^2 + \frac{1}{4}\lambda_\phi(\phi^2)^2, \quad (1.22)$$

which has nonrenormalizable couplings and is therefore not valid up to arbitrary scales.

Further studies, also using numerical simulations, were done in [27, 58, 59, 60, 61, 62, 63, 64], where [62] is reproduced in chapter 3 of this thesis. These studies a.o. confirmed that there is baryon production, that an asymmetry can be created if the Lagrangian is CP violating, and investigated the dependence of the asymmetry on the parameters, the mechanism of baryon production, and the dependence on the speed at which the effective Higgs potential changes. Recently the generation of magnetic fields in this model was studied in [65].

³Note however that later versions of the model have nonrenormalizable couplings, as discussed below, and will therefore need a UV completion not much above the electroweak scale.

1.4 OUTLINE

In part I two aspects of CEB are studied: the baryon production mechanism and the CP violation. Because CEB relies so strongly on the Standard Model, we first review some relevant aspects of the (electroweak sector of the) Standard Model in chapter 2, including the CKM matrix, the electroweak anomaly and the Chern-Simons and Higgs winding numbers. Then in chapter 3 the mechanism is studied by which the Chern-Simons number changes, building further on the work of [61]. Here a simplified model is used in which the inflaton field is left out, and the transition is triggered by an instantaneous change of the sign of the Higgs mass term. We find that configurations with a small Higgs field in the center, called half-knots, play a central role in the process of changing the Chern-Simons number. This work has been published in [62].

In chapter 4 the CP violating effect in the Standard Model is studied by integrating out the fermions. In an expansion in fields of the resulting bosonic effective action we find that the first CP violating term is indeed proportional to the factor (1.20). We argue that the resulting estimate is valid in CEB and that therefore the strength of the CP violating effect is too small to be responsible for the observed asymmetry (1.18). We conclude in chapter 5.

CHAPTER 2

STANDARD MODEL

The Standard Model of particle physics was developed in the early 1970s and describes three of the four known fundamental interactions and all the known elementary particles. It consists of the electroweak theory describing the electromagnetic and the weak interactions, and Quantum Chromodynamics (QCD) that describes the strong interaction. These interactions are mediated by gauge bosons. The interaction that is not included in the Standard Model is gravity. The elementary fermionic particles of the Standard Model are the quarks (that make up the baryons) and the leptons. The predictions of the Standard Model are in agreement with all experimental data to date.

Because of its importance for CEB, we review here a few relevant aspects of the Standard Model, in particular on the electroweak sector. More complete reviews can be found in textbooks and lecture notes, see e.g. references [66, 67, 68, 69].

First we give the action of the Standard Model in section 2.1, and its formulation in the unitarity gauge in section 2.2. We leave out the leptons and take only the quarks into account. In section 2.3 the charge conjugation and parity transformations are reviewed. Then the electroweak anomaly, responsible for baryon violation in the Standard Model, is briefly reviewed in section 2.4. Finally we discuss the role of topological field configurations in section 2.5.

2.1 ACTION

The Standard Model is a chiral gauge theory with gauge group $SU(3) \times SU(2) \times U(1)$. The matter fields are chiral fermions that couple to the gauge fields. The $SU(2) \times U(1)$

subgroup corresponds to the electroweak theory, which also contains a scalar field, the Higgs field. The $SU(3)$ subgroup corresponds to QCD.

We write the action of the Standard Model as

$$S_{\text{SM}} = \int d^4x \mathcal{L}_{\text{SM}}, \quad \mathcal{L}_{\text{SM}} = \mathcal{L}_G + \mathcal{L}_H + \mathcal{L}_F + \mathcal{L}_Y, \quad (2.1)$$

where \mathcal{L}_G describes the gauge fields, \mathcal{L}_H the Higgs field, \mathcal{L}_F the fermions and \mathcal{L}_Y the Yukawa interaction between the fermions and the Higgs field. We describe the former two terms in subsection 2.1.1 and the latter two in subsection 2.1.2.

2.1.1 BOSONS

GAUGE FIELDS

The gauge fields of the Standard Model are the $U(1)$ field B_μ , the $SU(2)$ fields A_μ^a , and the $SU(3)$ fields G_μ^k . The Lagrangian density of the gauge sector of the Standard Model is given by (the sign is the consequence of our conventions, see Appendix A):

$$-\mathcal{L}_G = \frac{1}{4} B_{\mu\nu} B^{\mu\nu} + \frac{1}{4} A_{\mu\nu}^a A^{a,\mu\nu} + \frac{1}{4} G_{\mu\nu}^k G^{k,\mu\nu}, \quad (2.2)$$

with

$$B_{\mu\nu} = \partial_\mu B_\nu - \partial_\nu B_\mu, \quad (2.3)$$

$$A_{\mu\nu}^a = \partial_\mu A_\nu^a - \partial_\nu A_\mu^a + g_2 \epsilon_{abc} A_\mu^b A_\nu^c, \quad (2.4)$$

$$G_{\mu\nu}^k = \partial_\mu G_\nu^k - \partial_\nu G_\mu^k + g_3 f_{klm} G_\mu^l G_\nu^m, \quad (2.5)$$

where g_2 and g_3 are the coupling constants of $SU(2)$ and $SU(3)$ respectively, and ϵ_{abc} , f_{abc} are the structure constants of these groups.

HIGGS FIELD

The Higgs field ϕ is a scalar field that transforms as a doublet under the $SU(2)$ group, and can therefore be written as

$$\phi = \begin{pmatrix} \varphi_u \\ \varphi_d \end{pmatrix}, \quad (2.6)$$

where the subscripts u and d denote up and down. The Higgs Lagrangian density is

$$-\mathcal{L}_H = (D_\mu \phi)^\dagger D^\mu \phi + V(\phi), \quad V(\phi) = V_0 - \mu^2 \phi^\dagger \phi + \lambda (\phi^\dagger \phi)^2. \quad (2.7)$$

The covariant derivative is

$$D_\mu \phi = \left(\partial_\mu - \frac{i}{2} g_1 B_\mu - i g_2 \frac{\tau^a}{2} A_\mu^a \right) \phi, \quad (2.8)$$

where g_1 is the $U(1)$ coupling constant, and τ^a are the Pauli matrices. The Higgs field does not couple to the $SU(3)$ gauge fields.

The minimum of the potential $V(\phi)$ is at $\phi^\dagger \phi = v^2/2$, with $v = \sqrt{\mu^2/\lambda}$, which causes spontaneous breaking of the $SU(2) \times U(1)$ gauge symmetry. This leads to effective mass terms for gauge bosons and fermions, as we will see in section 2.2.

2.1.2 FERMIONS

CHIRAL FERMIONS

The Standard Model is a chiral gauge theory, which means that fermions of different chirality couple differently to the gauge fields. Chiral fermions are described by Weyl spinors, which are eigenspinors of γ_5 (see Appendix A for conventions on γ matrices):

$$\gamma_5 \psi_R = \psi_R, \quad \gamma_5 \psi_L = -\psi_L, \quad (2.9)$$

where the subscripts R and L denote right- and left-handed. For later reference it is useful to define the chiral projectors

$$P_R = \frac{1}{2} (1 + \gamma_5), \quad P_L = \frac{1}{2} (1 - \gamma_5), \quad (2.10)$$

such that

$$P_R \psi = \psi_R, \quad P_L \psi = \psi_L, \quad \bar{\psi} P_R = \bar{\psi}_L, \quad \bar{\psi} P_L = \bar{\psi}_R, \quad (2.11)$$

where ψ is a Dirac spinor.

Apart from the kinetic and Yukawa terms that are discussed below, chiral fermions can also have Majorana mass terms if they are not charged under any gauge group. These terms may occur in the lepton sector of the Standard Model but not in the quark sector. Therefore we will not consider them here. Note that there are no Dirac mass terms for chiral fermions.

KINETIC TERM \mathcal{L}_F

The fermions of the Standard Model are the quarks and the leptons. In this thesis we consider only the quark sector¹. The quarks of the Standard Model are the right-handed

¹In the full quantum theory it is not possible to leave out the leptons because anomalies would make the Standard Model inconsistent.

	$\frac{Y}{2}$	T_2^a	T_3^k
$u_{R,g}$	2/3	0	$\lambda^k/2$
$d_{R,g}$	-1/3	0	$\lambda^k/2$
$q_{L,g}$	1/6	$\tau^a/2$	$\lambda^k/2$

Table 2.1: The quark fields of the Standard Model with their hypercharges Y and the generators T_2^a and T_3^k of their representations under $SU(2)$ and $SU(3)$. τ^a and λ^k are the generators of the fundamental representations of $SU(2)$ and $SU(3)$ respectively.

fields $u_{R,g}$, $d_{R,g}$ and the left-handed field $q_{L,g}$, where g is a generation index that runs from one to three. The kinetic term (which includes the interactions with the gauge fields via the covariant derivative) is given by

$$-\mathcal{L}_F = \bar{u}_{R,g}\gamma^\mu D_\mu u_{R,g} + \bar{d}_{R,g}\gamma^\mu D_\mu d_{R,g} + \bar{q}_{L,g}\gamma^\mu D_\mu q_{L,g}, \quad (2.12)$$

where the covariant derivative is

$$D_\mu\psi = \left(\partial_\mu - ig_1 \frac{Y}{2} B_\mu - ig_2 T_2^a A_\mu^a - ig_3 T_3^k G_\mu^k \right) \psi, \quad (2.13)$$

where ψ is to be substituted by $u_{R,g}$, $d_{R,g}$ or $q_{L,g}$. The hypercharge Y , and the generators T_2^a and T_3^k depend on the species and are given in table 2.1.

It will be convenient to combine all the quark fields into one doublet:

$$q_g = \begin{pmatrix} u_g \\ d_g \end{pmatrix} = q_{L,g} + \begin{pmatrix} u_{R,g} \\ d_{R,g} \end{pmatrix}. \quad (2.14)$$

The gauge fields can then be coupled to only the right- or left-handed parts of q_g by using the projectors P_L and P_R . The kinetic term (2.12) is then written as

$$-\mathcal{L}_F = \bar{q}_g \gamma^\mu D_\mu q_g, \quad (2.15)$$

where the covariant derivative is

$$D_\mu q_g = \left\{ \partial_\mu - ig_1 \left(\begin{pmatrix} 2/3 & 0 \\ 0 & -1/3 \end{pmatrix} P_R + \begin{pmatrix} 1/6 & 0 \\ 0 & 1/6 \end{pmatrix} P_L \right) B_\mu + \right. \\ \left. - ig_2 \frac{\tau^a}{2} A_\mu^a P_L - ig_3 \frac{\lambda^k}{2} G_\mu^k \right\} q_g, \quad (2.16)$$

where the matrices in $SU(2)$ space have been explicitly written out for the B_μ term. Note that there are no chiral projectors P_L and P_R for the $SU(3)$ gauge fields.

YUKAWA INTERACTIONS

The chiral quark fields can have Yukawa interactions with the Higgs field. In this section we construct all the allowed interactions for the fields $u_{R,g}$, $d_{R,g}$ and $q_{L,g}$. At the end of this section we will rewrite the result in terms of the field q_g of equation (2.14).

Yukawa interactions couple left-handed spinors to right-handed spinors. The number of possible interaction terms is strongly constrained by the condition of gauge invariance. To get a term that is invariant under the $SU(2)$ symmetry, the field q_L must couple to the Higgs field, either as $\bar{q}_L \phi$, or as $\bar{q}_L \tilde{\phi}$ (or hermitian conjugates), where

$$\tilde{\phi} = i\tau^2 \phi^* = \begin{pmatrix} \varphi_d^* \\ -\varphi_u^* \end{pmatrix}. \quad (2.17)$$

To make the terms invariant under the $U(1)$ group, one needs to count hypercharges. Those of the quarks are given in table 2.1. The Higgs field ϕ has $Y = 1$ and $\tilde{\phi}$ has $Y = -1$. It follows that the only gauge invariant combinations are

$$\left(\bar{q}_L \tilde{\phi}\right) u_R, \quad \text{and} \quad \left(\bar{q}_L \phi\right) d_R \quad (2.18)$$

and hermitian conjugates. Finally there is nothing that prevents the generations from mixing, which results in

$$-\mathcal{L}_Y = \left(\bar{q}_{L,g} \tilde{\phi}\right) F_{gg'}^u u_{R,g'} + \left(\bar{q}_{L,g} \phi\right) F_{gg'}^d d_{R,g'} + h.c., \quad (2.19)$$

where F^u and F^d are matrices in generation space.

Just as we did above for the kinetic term, we can write the Yukawa interaction in terms of the field q_g . To this end it is useful to introduce the notation

$$\Phi = \begin{pmatrix} \tilde{\phi} \phi \\ \phi \phi \end{pmatrix} = \begin{pmatrix} \varphi_d^* & \varphi_u \\ -\varphi_u^* & \varphi_d \end{pmatrix}, \quad (2.20)$$

and to combine the F^u and F^d matrices into a bigger matrix

$$F = \begin{pmatrix} F^u & 0 \\ 0 & F^d \end{pmatrix}. \quad (2.21)$$

The field q_g and the matrix F live in a six dimensional space with $SU(2)$ indices and generation indices (we suppress the $SU(3)$ indices). We call this isogeneration space. Φ also lives in this space; it is identity for the generation subspace. The Yukawa term (2.19) is then written as

$$-\mathcal{L}_Y = \bar{q} \Phi F P_R q + h.c., \quad (2.22)$$

where we suppressed all the indices.

2.2 UNITARITY GAUGE

The Higgs field plays an important role in the Standard Model: it has a non-vanishing vacuum expectation value which causes spontaneous breaking of the $SU(2) \times U(1)$ gauge symmetry. As a consequence gauge bosons and fermions can obtain masses. This is not at all clear from the formulation of the previous section. In this section the action of the Standard Model is reformulated by fixing the gauge in the unitarity gauge and by transforming the gauge bosons and the fermions to their mass eigenstates. The resulting interactions will be used in chapter 4.

2.2.1 HIGGS FIELD

In the unitarity gauge, the gauge is fixed such that the Higgs field (2.6) has $\varphi_u = 0$ and φ_d is real. Expanding about the (tree level) vacuum gives

$$\phi = \frac{1}{\sqrt{2}} \begin{pmatrix} 0 \\ v + h \end{pmatrix}, \quad (2.23)$$

where v is the vacuum expectation value, and h is a real field with mass

$$m_H = \sqrt{2\lambda} v, \quad (2.24)$$

which is obtained from the potential $V(\phi)$ in the Lagrangian density (2.7).

2.2.2 GAUGE BOSON MASS EIGENSTATES

The vacuum expectation value in (2.23) leads to quadratic terms for the gauge fields from the kinetic term $(D_\mu \phi)^\dagger D^\mu \phi$ in the Lagrangian density (2.7). These terms mix the different gauge fields, but they can be diagonalized by transforming the gauge fields to their mass eigenstates:

$$\begin{pmatrix} Z_\mu^0 \\ A_\mu \end{pmatrix} = \begin{pmatrix} \cos \theta_W & -\sin \theta_W \\ \sin \theta_W & \cos \theta_W \end{pmatrix} \begin{pmatrix} A_\mu^3 \\ B_\mu \end{pmatrix} \quad (2.25)$$

$$W_\mu^\pm = \frac{1}{\sqrt{2}} (A_\mu^1 \mp i A_\mu^2). \quad (2.26)$$

where θ_W is the Weinberg angle, which satisfies $\tan \theta_W = g_1/g_2$. The masses of the transformed fields are

$$m_W = \frac{1}{2} g_2 v, \quad m_Z = m_W / \cos \theta_W, \quad m_A = 0. \quad (2.27)$$

The massless boson A_μ is identified with the photon.

Note that in the unitarity gauge (2.23) the Higgs field has only one degree of freedom left; the other three have been ‘eaten’ by the massive gauge bosons.

The covariant derivative (2.16) acting on the quark field q can be rewritten in terms of the gauge boson mass eigenstates. Using the definition of the electric charge

$$e = g_1 \cos \theta_W = g_2 \sin \theta_W, \quad (2.28)$$

one obtains

$$D_\mu q_g = \left\{ \partial_\mu - ieA_\mu \begin{pmatrix} 2/3 & 0 \\ 0 & -1/3 \end{pmatrix} - i \frac{e}{\sqrt{2} \sin \theta_W} \begin{pmatrix} 0 & W_\mu^+ \\ W_\mu^- & 0 \end{pmatrix} P_L + \right. \\ \left. - i \frac{e \tan \theta_W}{6} Z_\mu^0 \begin{pmatrix} -4P_R - (1 - \frac{3}{\tan^2 \theta_W})P_L & 0 \\ 0 & 2P_R - (1 + \frac{3}{\tan^2 \theta_W})P_L \end{pmatrix} + \right. \\ \left. - ig_3 \frac{\lambda^k}{2} G_\mu^k \right\} q_g, \quad (2.29)$$

where the chiral projectors have disappeared in the interactions with the photon A_μ .

2.2.3 FERMION MASS EIGENSTATES

In the unitarity gauge, Φ becomes proportional to unity: $\Phi = \varphi_d 1$. The Yukawa interaction (2.22) is then

$$-\mathcal{L}_Y = \varphi_d \bar{q} (FP_R + F^\dagger P_L) q. \quad (2.30)$$

By transforming the quark field q such that F becomes real and diagonal, this term becomes a mass term for $\varphi_d \rightarrow v/\sqrt{2}$.

To find the necessary transformation rules, we write the matrix F^u in a polar decomposition as $P^u U^u$, with $P^u = \sqrt{F^u F^{u\dagger}}$ and $U^u = (P^u)^{-1} F^u$. The matrix P^u is positive definite and hermitian and can be written as $V^u D^u V^{u\dagger}$ with D^u a real (and positive) diagonal matrix. The matrices V^u and U^u are unitary. Together we have

$$F^u = V^u D^u V^{u\dagger} U^u, \quad F^d = V^d D^d V^{d\dagger} U^d, \quad (2.31)$$

where we have applied the same reasoning to F^d . Hence if we transform the quark field by

$$q_{L,g} \rightarrow \begin{pmatrix} V_{gg'}^u & 0 \\ 0 & V_{gg'}^d \end{pmatrix} q_{L,g'}, \quad q_{R,g} \rightarrow \begin{pmatrix} U_{gg'}^{u\dagger} V_{g'g''}^u & 0 \\ 0 & U_{gg'}^{d\dagger} V_{g'g''}^d \end{pmatrix} q_{R,g''}, \quad (2.32)$$

the Yukawa interaction (2.30) becomes

$$-\mathcal{L}_Y = \varphi_d \bar{q} D q, \quad D = \begin{pmatrix} D^u & 0 \\ 0 & D^d \end{pmatrix}, \quad (2.33)$$

which is a mass term for $\varphi_d \rightarrow v/\sqrt{2}$. The mass eigenstates u_g are called the up, charm and top quark (for generation indices g from one to three), and the mass eigenstates d_g are called the down, strange and bottom quark. The (diagonal) elements of D are the Yukawa coupling constants $\lambda_u, \lambda_c, \lambda_t, \lambda_d, \lambda_s$ and λ_b .

The transformations (2.32) do not commute with all the fermion-gauge interactions. Inspection of the covariant derivative (2.29) shows that the term with the W^\pm is affected, and becomes

$$\bar{q} \gamma^\mu \left(-i \frac{e}{\sqrt{2} \sin \theta_W} \begin{pmatrix} 0 & W_\mu^+ V \\ W_\mu^- V^\dagger & 0 \end{pmatrix} P_L \right) q, \quad (2.34)$$

where $V = V^{u\dagger} V^d$ is the Cabibbo-Kobayashi-Maskawa (CKM) matrix. The other terms of the covariant derivative (2.29) are unaffected by the transformations (2.32). For later reference it will be convenient to use the notation

$$\tilde{\tau}^+ = \frac{e}{\sqrt{2} \sin \theta_W} \begin{pmatrix} 0 & V \\ 0 & 0 \end{pmatrix}, \quad \tilde{\tau}^- = \frac{e}{\sqrt{2} \sin \theta_W} \begin{pmatrix} 0 & 0 \\ V^\dagger & 0 \end{pmatrix}, \quad (2.35)$$

such that the interaction term between the quark field q and W^\pm (2.34) is written as

$$-i \bar{q} \gamma^\mu (W_\mu^+ \tilde{\tau}^+ + W_\mu^- \tilde{\tau}^-) P_L q. \quad (2.36)$$

The CKM matrix V is a unitary matrix that has nine parameters (for three generations). Three of these parameters are real rotation angles (from the real subgroup $O(3)$). The other six parameters are complex phase factors. One can rotate away five of these phases by global transformations $q_{L,g} \rightarrow e^{i\alpha} q_{L,g}$ (because six fields have five relative phases). Therefore the CKM matrix contains four observable parameters, one of which is a complex phase factor.

2.3 C AND P TRANSFORMATIONS

For baryogenesis it is essential that charge (C) and charge-parity (CP) symmetries are broken. In this section we recall how the C and P transformations act on the various fields, and apply these transformations to a few relevant operators, in order to show that C and CP are indeed not symmetries of the Standard Model.

THE TRANSFORMATIONS

A scalar field ϕ transforms as

$$C\phi(t, \mathbf{x})C^{-1} = \phi(t, \mathbf{x})^*, \quad (2.37)$$

$$P\phi(t, \mathbf{x})P^{-1} = \phi(t, -\mathbf{x}). \quad (2.38)$$

A vector field A_μ transforms as

$$CA_\mu(t, \mathbf{x})C^{-1} = -A_\mu(t, \mathbf{x})^*, \quad (2.39)$$

$$PA_\mu(t, \mathbf{x})P^{-1} = -(-1)_\mu A_\mu(t, -\mathbf{x}), \quad (2.40)$$

where $(-1)_\mu$ is -1 for $\mu = 0$ and 1 for $\mu = 1, 2, 3$ (there is no summation over the μ indices). From these transformation rules it follows that the corresponding field strength $F_{\mu\nu}$ transforms as

$$CF_{\mu\nu}(t, \mathbf{x})C^{-1} = -F_{\mu\nu}(t, \mathbf{x})^*, \quad (2.41)$$

$$PF_{\mu\nu}(t, \mathbf{x})P^{-1} = (-1)_\mu(-1)_\nu F_{\mu\nu}(t, -\mathbf{x}). \quad (2.42)$$

As a consequence $\int F_{\mu\nu}F^{\mu\nu}$ is invariant under C (where we use that this term is real) and P , and $\int \epsilon^{\mu\nu\alpha\beta}F_{\mu\nu}F_{\alpha\beta}$ is invariant under C but changes sign under P transformations.

A fermion field ψ transforms as

$$C\psi(t, \mathbf{x})C^{-1} = -\beta\mathcal{C}\psi^*(t, \mathbf{x}) = (\bar{\psi}C^{-1})^T, \quad (2.43)$$

$$P\psi(t, \mathbf{x})P^{-1} = \beta\psi(t, -\mathbf{x}), \quad (2.44)$$

from which one can derive for $\bar{\psi}$

$$C\bar{\psi}(t, \mathbf{x})C^{-1} = -(\mathcal{C}\psi(t, \mathbf{x}))^T, \quad (2.45)$$

$$P\bar{\psi}(t, \mathbf{x})P^{-1} = \bar{\psi}(t, -\mathbf{x})\beta. \quad (2.46)$$

The definitions of the matrices β and \mathcal{C} are given in Appendix A.

APPLICATIONS

Next we apply these transformations to a few relevant operators.

Baryon number. Baryons are bound states of three quarks. The baryon current is therefore defined by

$$3j_B^\mu \equiv j_q^\mu = i\bar{q}\gamma^\mu q, \quad (2.47)$$

where there is summation over the (implicit) group and generation indices. It transforms as

$$Cj_B^\mu(t, \mathbf{x})C^{-1} = -j_B^\mu(t, \mathbf{x}), \quad Pj_B^\mu(t, \mathbf{x})P^{-1} = -(-1)^\mu j_B^\mu(t, -\mathbf{x}), \quad (2.48)$$

Thus the baryon number $B = \int d^3x j_B^0$ is odd under C and even under P .

Quark interactions. Next we consider the interaction terms of the quarks. The quark-Higgs interaction in the unitarity gauge and in terms of the fermion mass eigenstates (2.33) is invariant under C and P (after integration over spacetime). The interactions with the W^\pm fields in (2.36) transform as:

$$C \left\{ \bar{q} \gamma^\mu \begin{pmatrix} 0 & W_\mu^+ V \\ W_\mu^- V^\dagger & 0 \end{pmatrix} P_L q \right\} C^{-1} = \bar{q} \gamma^\mu \begin{pmatrix} 0 & W_\mu^+ V^* \\ W_\mu^- V^T & 0 \end{pmatrix} P_R q, \quad (2.49)$$

$$P \left\{ \bar{q} \gamma^\mu \begin{pmatrix} 0 & W_\mu^+ V \\ W_\mu^- V^\dagger & 0 \end{pmatrix} P_L q \right\} P^{-1} = \bar{q} \gamma^\mu \begin{pmatrix} 0 & W_\mu^+ V \\ W_\mu^- V^\dagger & 0 \end{pmatrix} P_R q, \quad (2.50)$$

where we have used that $W_\mu^{\pm*} = W_\mu^\mp$. Hence both C and P symmetries are violated. Under the combined CP transformation the only change is that the CKM matrix V is complex conjugated. Because the V is complex, there is CP violation.

The other quark-gauge interactions only interchange P_L and P_R under both C and P transformations and are invariant under the combined CP transformation.

2.4 ELECTROWEAK ANOMALY

After having established that the Standard Model violates C and CP symmetries, we proceed to another essential ingredient for baryogenesis: violation of baryon number conservation. In the Standard Model this happens via the electroweak anomaly [70]. This is a subtle quantum effect and is closely related to the Adler-Bell-Jackiw (ABJ) anomaly, which is well covered in textbooks (e.g. [66, 68]).

In this section we review the ABJ anomaly very briefly (see the aforementioned textbooks for more details), and then explain in more detail how the electroweak anomaly equation can be derived from the standard ABJ anomaly result.

2.4.1 ADLER-BELL-JACKIW ANOMALY

Consider massless Quantum Electrodynamics (QED) with action

$$S = \int d^4x \bar{\psi} \gamma^\mu (\partial_\mu - ieA_\mu) \psi. \quad (2.51)$$

At the classical level the currents

$$j^\mu = i\bar{\psi} \gamma^\mu \psi, \quad j_5^\mu = i\bar{\psi} \gamma^\mu \gamma_5 \psi, \quad (2.52)$$

are conserved:

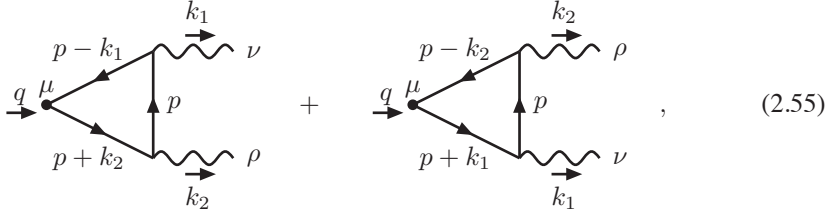
$$\partial_\mu j^\mu = 0, \quad \partial_\mu j_5^\mu = 0, \quad (2.53)$$

as can easily be checked by using the classical equations of motion. The conservation of the current j^μ corresponds to a $U(1)$ symmetry (which is gauged), and of the current j_5^μ to an axial $U(1)$ symmetry. However in the presence of an electromagnetic field the latter symmetry can be broken by a quantum effect, which is called the ABJ anomaly [71, 72].

The anomaly can be proven in a number of ways. We will consider the divergence of the expectation value of j_5^μ in the presence of gauge fields:

$$\int d^4x e^{-iq \cdot x} \langle k_1, k_2 | j_5^\mu(x) | 0 \rangle = (2\pi)^4 \delta^4(k_1 + k_2 - q) \epsilon_\nu^*(k_1) \epsilon_\rho^*(k_2) \mathcal{M}^{\mu\nu\rho}(k_1, k_2), \quad (2.54)$$

where $\epsilon_\nu(k_1)$ and $\epsilon_\rho(k_2)$ are polarization vectors of the electromagnetic field. The amplitude $\mathcal{M}^{\mu\nu\rho}$ is given by the triangle diagrams



$$+ \quad (2.55)$$

which are equal to

$$(-1) \int \frac{d^4p}{(2\pi)^4} \text{Tr} \left[\gamma^\mu \gamma_5 \frac{-(\not{p} - \not{k}_1)}{(p - k_1)^2 - i\epsilon} e \gamma^\nu \frac{-\not{p}}{p^2 - i\epsilon} e \gamma^\rho \frac{-(\not{p} + \not{k}_2)}{(p + k_2)^2 - i\epsilon} \right] + (k_1 \leftrightarrow k_2, \nu \leftrightarrow \rho). \quad (2.56)$$

The divergence of the expectation value (2.54) can be calculated (after careful regularization) and is

$$\int d^4x e^{-iq \cdot x} \langle k_1, k_2 | \partial_\mu j_5^\mu(x) | 0 \rangle = \frac{e^2}{2\pi^2} \epsilon^{\alpha\nu\beta\rho} k_{1\alpha} \epsilon_\nu^*(k_1) k_{2\beta} \epsilon_\rho^*(k_2) \delta^4(k_1 + k_2 - q). \quad (2.57)$$

It can be shown by considering higher loop diagrams and other matrix elements that there are no other contributions. One concludes that the ABJ anomaly equation is

$$\partial_\mu j_5^\mu = -\frac{e^2}{8\pi^2} F_{\mu\nu} \tilde{F}^{\mu\nu}, \quad (2.58)$$

with $\tilde{F}^{\mu\nu} = \frac{1}{2} \epsilon^{\mu\nu\alpha\beta} F_{\alpha\beta}$. Note that both sides of this equation are quantum operators. The anomaly only affects the axial current j_5^μ and not the vector current j^μ such that the gauge symmetry is not broken.

2.4.2 ELECTROWEAK ANOMALY

In the electroweak theory the effect is basically the same, albeit slightly more complicated because of the chiral nature of this theory. As a consequence quark number (and

therefore baryon number) conservation is violated by the anomaly. Here we calculate the divergence of the quark current in the presence of gauge fields of the Standard Model by making use of the ABJ calculation above.

We use the formulation of the Standard Model as in section 2.1 and not the gauge fixed formulation of section 2.2. So the quark-gauge interactions follow from the covariant derivative (2.16). The quark current is defined in (2.47) and the relevant expectation value is

$$\int d^4x e^{-iq \cdot x} \langle k_1, \nu, a; k_2, \rho, b | j_Q^\mu(x) | 0 \rangle = (2\pi)^4 \delta^4(k_1 + k_2 - q) \epsilon_\nu^{a*} \epsilon_\rho^{b*} \mathcal{M}^{\mu\nu\rho, ab}(k_1, k_2). \quad (2.59)$$

where ϵ_ν^a is the polarization vector corresponding to the field B_ν (in this case there is only one $U(1)$ field and no index a), A_ν^a or G_ν^a . The amplitude $\mathcal{M}^{\mu\nu\rho, ab}$ is

$$(-1) \int \frac{d^4p}{(2\pi)^4} \text{Tr} \left[\gamma^\mu \frac{-(\not{p} - \not{k}_1)}{(p - k_1)^2 - i\epsilon} \Gamma^{\nu, a} \frac{-\not{p}}{p^2 - i\epsilon} \Gamma^{\rho, b} \frac{-(\not{p} + \not{k}_2)}{(p + k_2)^2 - i\epsilon} \right] + \\ (k_1 \leftrightarrow k_2, a \leftrightarrow b, \nu \leftrightarrow \rho), \quad (2.60)$$

where the field q is running around in the loop and the trace is over Dirac, group and generation indices. The vertices $\Gamma^{\mu, a}$ follow from the covariant derivative (2.16), and are

$$U(1) : \Gamma^\mu = g_1 \gamma^\mu \left(\begin{pmatrix} 2/3 & 0 \\ 0 & -1/3 \end{pmatrix} P_R + \begin{pmatrix} 1/6 & 0 \\ 0 & 1/6 \end{pmatrix} P_L \right), \quad (2.61)$$

$$SU(2) : \Gamma^{\mu, a} = g_2 \gamma^\mu \frac{\tau^a}{2} P_L, \quad (2.62)$$

$$SU(3) : \Gamma^{\mu, a} = g_3 \gamma^\mu \frac{\lambda^a}{2}. \quad (2.63)$$

For different combinations of external gauge fields we can relate expression (2.60) to the one of the ABJ anomaly (2.56). If the two external gauge fields are from different groups, the expression vanishes because of the trace over the gauge indices. Moreover, if there is no projector P_L or P_R at all in (2.60), the expression vanishes too (by Furry's theorem), which is the reason that the $SU(3)$ fields do not contribute to the electroweak anomaly.

Consider first the case of two $U(1)$ fields B_μ . Because $P_L P_R = 0$ and $P_L^2 = P_L$, $P_R^2 = P_R$, the contributions are

$$g_1^2 \left(\begin{pmatrix} (1/6)^2 & 0 \\ 0 & (1/6)^2 \end{pmatrix} P_L, \quad \text{and} \quad g_1^2 \left(\begin{pmatrix} (2/3)^2 & 0 \\ 0 & (-1/3)^2 \end{pmatrix} P_R. \quad (2.64)$$

The first contribution relates to the ABJ expression by a factor:

$$-\frac{1}{2} \times n_g \times 3_{SU(3)} \times 2 \times (1/6)^2 \times \frac{g_1^2}{e^2}, \quad (2.65)$$

and the second by a factor

$$\frac{1}{2} \times n_g \times 3_{SU(3)} \times \left(\frac{4}{9} + \frac{1}{9}\right) \times \frac{g_1^2}{e^2}, \quad (2.66)$$

where the factors $-1/2$ and $1/2$ come from P_L and P_R , and where n_g is the number of generations, which is equal to three in the Standard Model. These factors add up to $3n_g g_1^2/4$, so that the contribution to $\partial_\mu j_Q^\mu$ is

$$-3n_g \frac{g_1^2}{32\pi^2} B_{\mu\nu} \tilde{B}^{\mu\nu}. \quad (2.67)$$

Next consider the case of two $SU(2)$ fields A_μ . Again there is a P_L projector that gives a factor $-1/2$. Furthermore there is a trace over two Pauli-matrices, which is $\text{Tr}(\tau^a \tau^b) = \delta^{ab}/2$. Together this contribution relates to the ABJ expression by a factor

$$-\frac{1}{2} \times n_g \times 3_{SU(3)} \times \frac{\delta^{ab}}{2} \times \frac{g_2^2}{e^2}. \quad (2.68)$$

In this nonabelian case there are also contributions from matrix elements with three or four external gauge fields. These contributions add up to the gauge invariant result

$$3n_g \frac{g_2^2}{32\pi^2} A_{\mu\nu}^a \tilde{A}^{a,\mu\nu}. \quad (2.69)$$

In total the electroweak anomaly equation is (note that the baryon current is one third of the quark current)

$$\partial_\mu j_B^\mu = n_g \left(\frac{g_2^2}{32\pi^2} A_{\mu\nu}^a \tilde{A}^{a,\mu\nu} - \frac{g_1^2}{32\pi^2} B_{\mu\nu} \tilde{B}^{\mu\nu} \right). \quad (2.70)$$

As in the ABJ case the anomaly does not affect the currents that couple to the gauge fields.

The anomaly in the lepton current can be calculated in the same way and turns out to be equal to the one in the baryon current. Therefore the difference between baryon number and lepton number $B - L$ is conserved also in the quantum theory. The sum $B + L$ is however not conserved.

2.5 TOPOLOGY IN THE ELECTROWEAK THEORY

At the classical level the right-hand side of the anomaly equation (2.70) has a topological interpretation, which is discussed in this section. The Chern-Simons number of the gauge fields and the related Higgs winding number are introduced, and the conditions under which they are integer winding numbers are discussed.

2.5.1 CHERN-SIMONS NUMBER N_{CS}

In this section we consider only the $SU(2)$ gauge fields A_μ^a , which corresponds to setting $g_1 = 0$. The anomaly equation then becomes

$$\partial_\mu j_B^\mu = n_g \frac{g_2^2}{32\pi^2} A_{\mu\nu}^a \tilde{A}^{a,\mu\nu}. \quad (2.71)$$

The right-hand side of the anomaly equation is, just like the left-hand side, a total derivative:

$$\frac{g_2^2}{32\pi^2} A_{\mu\nu}^a \tilde{A}^{a,\mu\nu} = \partial_\mu j_{\text{CS}}^\mu, \quad (2.72)$$

where the Chern-Simons current is defined by

$$j_{\text{CS}}^\mu = \frac{1}{16\pi^2} \epsilon^{\mu\nu\alpha\beta} \text{Tr} \left(A_\nu A_{\alpha\beta} + i \frac{2}{3} A_\nu A_\alpha A_\beta \right), \quad (2.73)$$

and we use the notation $A_\mu = g_2 \frac{\tau^a}{2} A_\mu^a$ and $A_{\mu\nu} = g_2 \frac{\tau^a}{2} A_{\mu\nu}^a$.² Thus the Chern-Simons number is

$$N_{\text{CS}} = \int d^3x j_{\text{CS}}^0 = -\frac{1}{16\pi^2} \epsilon^{ijk} \text{Tr} \left(A_i A_{jk} + i \frac{2}{3} A_i A_j A_k \right), \quad (2.74)$$

with the convention $\epsilon^{0123} = -1$. Both the Chern-Simons current and the Chern-Simons number are not gauge invariant.

If both sides of the anomaly equation (2.71) are integrated over all space, and over time from initial time t_i up to final time t_f , one obtains the relation

$$B(t_f) - B(t_i) = n_g (N_{\text{CS}}(t_f) - N_{\text{CS}}(t_i)), \quad (2.75)$$

with $B = \int d^3x j_B^0$ and where we have assumed that the currents vanish at spatial infinity. Hence baryons can be produced by changing the Chern-Simons number of the gauge fields. Because the right-hand side of the anomaly equation (2.71) is gauge invariant, the difference of the Chern-Simons numbers is also gauge invariant.

Under certain conditions, the Chern-Simons number is integer because it is a winding number. These conditions are that the field strength vanishes ($A_{\mu\nu} = 0$) and that space has the topology of a three sphere S^3 . If the field strength vanishes, the vector potential is pure gauge:

$$A_\mu = iU \partial_\mu U^{-1}, \quad U \in SU(2). \quad (2.76)$$

Therefore A_μ is completely determined by U and is a map from S^3 to $SU(2) \cong S^3$. Such maps fall in homotopy classes that are characterized by the integer winding number

$$-\frac{1}{24\pi^2} \int d^3x \epsilon^{ijk} \text{Tr}(U \partial_i U^{-1} U \partial_j U^{-1} U \partial_k U^{-1}). \quad (2.77)$$

²In chapter 3 the conventions are slightly different: the coupling is called g instead of g_2 and it is absorbed in the definition of A_μ^a (such that $A_\mu = A_\mu^a \tau^a / 2$). Moreover $A_{\mu\nu}$ is there called $F_{\mu\nu}$.

For $A_{jk} = 0$ the Chern-Simons number (2.74) is equal to this winding number, which shows that it is integer under the mentioned conditions.

2.5.2 HIGGS WINDING NUMBER N_w

One can also assign a winding number to the Higgs field. It is convenient to use the matrix notation of the Higgs field (2.20):

$$\Phi = \begin{pmatrix} \tilde{\phi} \\ \phi \end{pmatrix} = \frac{\rho}{\sqrt{2}}\Omega, \quad (2.78)$$

with $\rho^2 = 2(\varphi_u^*\varphi_u + \varphi_d^*\varphi_d)$ and with $\Omega \in SU(2)$. The Lagrangian density (2.7) is then written as

$$-\mathcal{L}_H = \frac{1}{2}\text{Tr} \left((D_\mu\Phi)^\dagger D^\mu\Phi \right) + \lambda \left(\frac{1}{2}\text{Tr} (\Phi^\dagger\Phi) - \frac{v^2}{2} \right)^2, \quad (2.79)$$

where the covariant derivative is $D_\mu\Phi = (\partial_\mu - iA_\mu)\Phi$.

Analogously to the winding number (2.77), we define the Higgs winding number as

$$N_w = -\frac{1}{24\pi^2} \int d^3x \epsilon^{ijk} \text{Tr}(\Omega\partial_i\Omega^{-1}\Omega\partial_j\Omega^{-1}\Omega\partial_k\Omega^{-1}), \quad (2.80)$$

which is only well defined if $\rho \neq 0$ everywhere in space, and which is not gauge invariant under ‘large’ gauge transformations. Note that, different from the Chern-Simons number, the Higgs winding number is also integer if the Higgs field is not in vacuum (as long as $\rho \neq 0$). But similar to the Chern-Simons number, the Higgs winding number is only guaranteed to be integer if space has the topology of a three sphere S^3 .

2.5.3 CHANGING N_{CS} AND N_w

Suppose that space has the topology of a three sphere S^3 . Then in vacuum both N_{CS} and N_w are integer. In fact, from the covariant derivative term in (2.79) one sees that in vacuum $\Omega = U$ and therefore that $N_{CS} = N_w = n$.

To go to another vacuum with $N_{CS} = N_w = n \pm 1$, the system has to pass through a non-vacuum state. The energy barrier in between the different vacua has (locally) the shape of a saddle, and the configuration at the lowest point on top of the barrier is called the sphaleron [73, 74]. It has $N_{CS} = n \pm 1/2$, and N_w is not defined because $\rho = 0$ in the center of this configuration. Because of this barrier, the tunneling amplitude from one vacuum to the other is strongly suppressed at low temperatures (compared to the electroweak scale), which explains why baryon number violation is not observed in the laboratory. However at high temperatures there are fluctuations over the barrier and baryon number can easily be changed.

In reality we do not know the global topology of the universe. However the sphaleron configuration is a local configuration, that will not be influenced by the global topology of the universe (as long as the universe is much larger than the inverse electroweak scale). Therefore N_{CS} and N_{w} will still change by integers, even if the topology of the universe is not S^3 .

We will discuss more configurations that change N_{CS} and N_{w} in chapter 3.

CHAPTER 3

CHERN-SIMONS AND WINDING NUMBER IN COLD ELECTROWEAK BARYOGENESIS

3.1 INTRODUCTION

Baryogenesis, the creation of the baryon asymmetry in the universe, is a long-standing problem in cosmology. It dates back to 1967 when Sakharov suggested that the baryon asymmetry is not an initial condition of the universe, but might be created later in a process based on particle physics [34]. This idea has gained support from the inflationary scenario, since inflation is supposed to have diluted any pre-existing asymmetry. Sakharov formulated his well-known conditions for baryogenesis: baryon number conservation, C , and CP must be violated, and a state of non-equilibrium must prevail.

Of the many particle physics scenarios that have been proposed in the past decades implementing such a process, electroweak baryogenesis [29, 30, 75] is interesting in that it suggested the possibility to explain the baryon asymmetry using mostly Standard Model physics. In this scenario the baryon number violation is caused by the anomaly that relates a change in baryon number B to a change in Chern-Simons number N_{CS} of the electroweak gauge fields:

$$\Delta B = 3\langle\Delta N_{CS}\rangle. \quad (3.1)$$

Furthermore the Standard Model violates C , it has a CP violating phase in the CKM quark mixing matrix, and the out-of-equilibrium conditions can be provided by an elec-

troweak phase transition. This phase transition was supposed to be caused by the lowering temperature of the universe, and to be sufficiently out of equilibrium it had to be of first order. However subsequent work has shown that for the experimentally allowed range of the Higgs mass, the electroweak phase transition is only a crossover (see e.g. [76]). It is widely believed that a crossover transition is too close to equilibrium for creation of the asymmetry. Furthermore, the CKM CP violation has been found to be much too small [47, 77, 78].

A few years ago, new scenarios were proposed [52, 53], in which electroweak baryogenesis takes place during a *tachyonic transition*. In such a transition the effective mass term in the Higgs potential starts being positive, and can change sign due to the coupling to an inflaton field, as in hybrid inflation [13]. The accompanying instability can lead to strongly out-of-equilibrium conditions with large occupation numbers in the Higgs and gauge fields, during which the energy in the Higgs field is transferred to the other fields by wave-like ‘rescattering’. The process is called tachyonic preheating [25]. During the transition there can be substantial changes in the Chern-Simons number, and also the baryon number via the anomaly equation (3.1). The universe was assumed to be cold after electroweak-scale inflation, so initially the transition takes place at practically zero temperature.

In subsequent papers the scenario was further refined and tested. Considerations of quantum corrections led to a change of model to inverted hybrid inflation [56], in which the inflaton rolls away from the origin instead of towards it. In [57] it was shown how WMAP data constrain the parameters of a model and it was noted that it might be falsified by the LHC. The transition was studied by analytic and numerical methods [79, 58, 59, 60, 61], and the magnitude of the asymmetry generated by a form of CP violation was computed in [58, 61].

The CP violating term in the Lagrangian that was used in [61] does not occur in the Standard Model. Of course, one is also interested in the CP violation from the CKM matrix. As mentioned above, this CP violation has been estimated to be much too small for baryogenesis [47, 77, 78], but these estimates do not seem to apply to a tachyonic transition at zero temperature. In fact, it has been suggested [80] that the effect might be much larger in this case. It is therefore important to make sure whether the CP violation of the Standard Model is sufficient to produce the baryon asymmetry.

Trying to investigate this problem by numerical simulation with three generations of fermions is a practically impossible task. Instead we have in mind a more tractable approach: if the changes of N_{CS} occur in a certain type of local field configuration, we could estimate the produced asymmetry by simulating only this local configuration. There is reason to believe that the change of N_{CS} indeed occurs in local configurations: in [60] evidence is found for local structures in numerical simulations, and in [53, 56] it is suggested that topological defects called textures play a role in this process. The presence of a

texture depends on the winding number of the Higgs field N_w . In the vacuum $N_{CS} = N_w$. A texture is a configuration which has winding number different from the Chern-Simons number. It is unstable and can decay either by changing the winding number or the Chern-Simons number. In [81, 82] a scenario for electroweak baryogenesis is investigated in which the change of Chern-Simons number occurs during the decays of textures. The textures were supposed to be formed directly after a first order electroweak phase transition, and the produced asymmetry was estimated by simulating a *single* texture and its decays. Such an approach was investigated further in ref. [83], where it was concluded that it is unlikely to be successful and that the asymmetry depends on too many variables to bypass a fully-fledged numerical simulation. We believe this conclusion is not so clear-cut and consider it worthwhile to understand more fully the mechanism that changes Chern-Simons numbers in tachyonic transitions.

In this chapter we study the production of winding and Chern-Simons number in a tachyonic transition. We shall argue that instead of textures, related configurations with half-integer winding number are important. We call such configurations half-knots.¹ These typically occur in regions where the Higgs magnitude has a small minimum. They can be stabilized when the Chern-Simons number density adjusts to the winding number density and the Higgs field relaxes towards its ground state, leaving a blob-like half-knot both in winding number and in Chern-Simons number. Half-knots have a rather high winding number density in their center and can be visualized in numerical simulations. We present some examples in detail.

In section 3.2 we review the Chern-Simons number, winding number and winding configurations in this model. Next we turn to the tachyonic transition and discuss our expectations with respect to the half-knots in this transition, in section 3.3. In section 3.4 we present the results of the numerical simulations, and we discuss the results in section 3.5.

3.2 WINDING IN THE $SU(2)$ HIGGS MODEL

In this section we review some topological features of the $SU(2)$ Higgs model, since it is the part of the Standard Model that plays a dominant role in the tachyonic transition. First we introduce the model and define the Higgs winding number and the Chern-Simons number. Then we discuss topological defects that may play a role in the transition: textures, sphalerons and half-knots.

¹The word half-knot appeared earlier in [84].

3.2.1 $SU(2)$ HIGGS MODEL

The action is given by

$$S = - \int d^4x \left[\frac{1}{2g^2} \text{Tr} F_{\mu\nu} F^{\mu\nu} + \frac{1}{2} \text{Tr} [(D_\mu \Phi)^\dagger D^\mu \Phi] + \lambda \left(\frac{1}{2} \text{Tr} [\Phi^\dagger \Phi] - \frac{v^2}{2} \right)^2 \right], \quad (3.2)$$

where the field strength is $F_{\mu\nu} = \partial_\mu A_\nu - \partial_\nu A_\mu - i[A_\mu, A_\nu]$, the vector potential can be written as $A_\mu = A_\mu^a \tau^a / 2$, and the covariant derivative acting on the Higgs field is $D_\mu \Phi = (\partial_\mu - iA_\mu) \Phi$. We use a metric with signature $(-1,1,1,1)$ and for the Higgs field we use the matrix notation:

$$\Phi = \begin{pmatrix} \varphi_d^* & \varphi_u \\ -\varphi_u^* & \varphi_d \end{pmatrix} = \frac{\rho}{\sqrt{2}} \Omega, \quad \rho^2 = 2(\varphi_u^* \varphi_u + \varphi_d^* \varphi_d), \quad \Omega(x) \in SU(2). \quad (3.3)$$

We call ρ the Higgs length. The Higgs and W masses are given by $m_H = \sqrt{2\lambda} v$ and $m_W = gv/2$, we also use the notation

$$\mu = \sqrt{\lambda v^2}. \quad (3.4)$$

As part of an extended theory, the mass term $-\lambda v^2 \frac{1}{2} \text{Tr} \Phi^\dagger \Phi$ is to be replaced by an effective mass term

$$\mu_{\text{eff}}^2 \frac{1}{2} \text{Tr} \Phi^\dagger \Phi, \quad (3.5)$$

where μ_{eff}^2 depends on time through the coupling to another field (inflaton). Initially it is positive, and when it changes to negative the tachyonic transition starts. Eventually μ_{eff}^2 will relax to the Standard Model value

$$\mu_{\text{eff}}^2 \rightarrow -\lambda v^2 = -\mu^2. \quad (3.6)$$

The rate of change of μ_{eff} depends on further details of the theory.

Throughout this chapter we use the so-called ‘temporal gauge’ $A_0 = 0$, which still leaves the freedom to do time-independent gauge transformations.

3.2.2 TOPOLOGY IN THE $SU(2)$ HIGGS MODEL

The non-conservation of baryon number in the Standard Model follows from the anomaly in the divergence of the baryon current,

$$\partial_\mu j_B^\mu = 3q, \quad (3.7)$$

$$q = \frac{1}{32\pi^2} \epsilon^{\kappa\lambda\mu\nu} \text{Tr} F_{\kappa\lambda} F_{\mu\nu} = \partial_\mu j_{\text{CS}}^\mu. \quad (3.8)$$

Here 3 is the number of generations and j_{CS}^μ is the Chern-Simons current; q is sometimes called the topological charge density, since, for classical fields, and in Euclidean space-time, its integral over a four-dimensional manifold without boundary is an integer, the topological charge. Taking the expectation value of (3.7) in the initial (Heisenberg) state and integrating between (real) times 0 and t gives

$$B(t) - B(0) = \int_0^t dx^0 \int d^3x \langle 3q \rangle = 3(N_{\text{CS}}(t) - N_{\text{CS}}(0)), \quad (3.9)$$

with $B = \langle \int d^3x J_B^0 \rangle$ the baryon number and

$$N_{\text{CS}} = \int d^3x j_{\text{CS}}^0, \quad j_{\text{CS}}^0 = -\frac{1}{16\pi^2} \epsilon^{jkl} \text{Tr} \left[A_j \left(F_{kl} + i\frac{2}{3} A_k A_l \right) \right], \quad (3.10)$$

the Chern-Simons number operator. We assumed that $\int d^3x \partial_k \langle j_{\text{CS}}^k \rangle$ vanishes, e.g. in a model with periodic boundary conditions, or because the fields vanish sufficiently fast at spatial infinity.

At this stage the Chern-Simons number and current are still operators, whereas the baryon number B is a c-number in the way we have written it. In the following we shall make a classical approximation (see section 3.3), and therefore we assume from now on that all fields are classical. Note that $N_{\text{CS}}(t)$ and $N_{\text{CS}}(t) - N_{\text{CS}}(0)$ are in general not integers.

The winding number of the Higgs field is given by

$$N_w = \int d^3x n_w, \quad (3.11)$$

$$n_w = \frac{1}{24\pi^2} \epsilon^{ijk} \text{Tr} [\partial_i \Omega \Omega^{-1} \partial_j \Omega \Omega^{-1} \partial_k \Omega \Omega^{-1}], \quad (3.12)$$

where Ω is given implicitly by (3.3); this is a valid definition as long as $\rho \neq 0$ everywhere. Classical vacuum configurations are given by

$$\Phi = \frac{v}{\sqrt{2}} \Omega, \quad A_j = -i\partial_j \Omega \Omega^{-1}, \quad \Omega \in SU(2). \quad (3.13)$$

Here Ω is arbitrary. It is easy to check that in the vacuum (3.13) the winding number density n_w equals the Chern-Simons number density j_{CS}^0 .

The winding number (3.11) and Chern-Simons number (3.10) are not gauge-invariant; they change by an integer under so-called large gauge transformations. As a consequence a vacuum configuration can have any integer winding number and Chern-Simons number, as long as they are equal $N_{\text{CS}} = N_w$. Under gauge transformations N_{CS} and N_w change by the same amount, so that the difference $N_w - N_{\text{CS}}$ is gauge-invariant. The change in time of N_{CS} as defined by the integral over q in (3.9) is also gauge invariant.

In the following we briefly discuss two well-known configurations that can play a role in changing the Chern-Simons and/or the winding number, namely the sphaleron and the texture.

3.2.3 SPHALERON

A sphaleron transition is a change from a vacuum with winding numbers $N_{CS} = N_w = n$, to another vacuum with $N_{CS} = N_w = n \pm 1$. It has been shown [73, 74] that the system must pass an energy barrier. The static and unstable configuration at the minimum barrier height is called a sphaleron, and its energy is the sphaleron energy. This configuration has vanishing Higgs length in the center, so that the winding number is not defined: it jumps by an integer exactly at the transition. The Chern-Simons number of a sphaleron is precisely $1/2$ (up to an integer).

The sphaleron energy E_{sph} is proportional to v/g , and approximately 10 TeV. Because of this high energy barrier, tunneling through the barrier (which corresponds to an instanton-like event) is strongly suppressed. Therefore the baryon number is effectively conserved at low temperatures. At higher temperatures the suppression is weaker because of thermal fluctuations over the barrier. It is also useful to interpret this in terms of an effective temperature dependent Higgs length $\langle \rho \rangle < v$ and an effective barrier height $\propto \langle \rho \rangle / g$. Above the electroweak phase transition temperature $\langle \rho \rangle$ vanishes and sphaleron transitions occur unsuppressed. During a tachyonic electroweak transition there are also frequent fluctuations over the barrier, as observed numerically in the susceptibility $\langle N_{CS}^2(t) \rangle$ [60, 61].

3.2.4 TEXTURE

Without gauge fields, a texture is a configuration with a nonzero winding number N_w , with the Higgs length equal to the vacuum value everywhere, and with only gradient energy. According to Derrick's theorem [85] such a configuration is unstable because its energy can be lowered indefinitely by shrinking it. Numerical simulations show that textures shrink quickly, and it was argued in [84] that in the end the configuration loses its winding number and decays into outgoing waves (see also [86] for work on collapsing textures).

For the $SU(2)$ Higgs model a natural extension of a texture is a gauged texture: a configuration with Chern-Simons number different from the winding number: $N_{CS} - N_w = \pm 1$. One can think of an initial configuration in which the gauge fields are pure-gauge with integer Chern-Simons number and Higgs length equal to the vacuum value. Just as in the global case, a gauged texture is unstable. There are basically two ways in which it can decay [81, 82]: when its size is smaller than approximately $1/m_W$, it decays by changing the winding number, and when it is larger it decays by changing the Chern-Simons number. In either case $N_{CS} - N_w \rightarrow 0$ and the configuration can spread indefinitely into outgoing waves.

3.2.5 HALF-KNOT

Although the total winding number in a finite volume with periodic boundary conditions is integer, in practice there is no reason to find local configurations with nearly integer winding number or Chern-Simons number. This is because there is no mechanism that would create such configurations, as there is, for example, energy minimization for monopoles. Consequently the winding number density can be spread out over the volume. However as we will argue below, there will be high winding number density regions where the Higgs length is very small. The total winding number in such a region is typically not integer, but close to $1/2$, which is why we call these configurations half-knots.

ONE DIMENSION

We illustrate this idea first in the simpler but analogous one dimensional case with a complex scalar field Φ and global symmetry group $U(1)$,

$$\Phi = \frac{1}{\sqrt{2}} (\phi_1 + i\phi_2) = \frac{\rho}{\sqrt{2}} \Omega, \quad \Omega \in U(1). \quad (3.14)$$

The winding number density is ($x \equiv x^1$)

$$n_w = -\frac{i}{2\pi} \Omega^* \partial_x \Omega = \frac{1}{2\pi\rho^2} (\phi_1 \partial_x \phi_2 - \phi_2 \partial_x \phi_1). \quad (3.15)$$

In a coordinate patch where we can write $\Omega(x) = \exp[i\omega(x) + \text{const.}]$ we also have $n_w = \frac{1}{2\pi} \partial_x \omega$.

In order to gain some intuition, let us consider the following simple form

$$\phi_1(x) = \cos(x) - .95, \quad \phi_2(x) = \sin(x), \quad (3.16)$$

for which the Higgs length ρ has a minimum when x is close to zero. This configuration is shown in a parametric plot in figure 3.1 at the end of this chapter. In this plot the Higgs length ρ is the distance from the origin, and the change of phase corresponds to the ‘winding’ of the curve around the origin. When there is a small Higgs length, the phase changes quickly (in this case approximately by an amount $+\pi$) and there is a high winding number density. We can see this also in figure 3.2, where the Higgs length squared ρ^2 and the winding number density are plotted. We call such a region with small Higgs length and large winding number density a *half-knot*. Note that the total winding number is integer (in this case $+1$), but that only part of the winding number density is concentrated in a small region. The rest of it is distributed approximately homogeneously over the rest of space.

We can formalize the half-knot by approximating ϕ_1 and ϕ_2 locally (around $x = 0$) by a linear form

$$\phi_\alpha = c_\alpha + d_\alpha x, \quad \alpha = 1, 2. \quad (3.17)$$

This corresponds to approximating the circle near the origin by a straight line, and gives

$$n_w = \frac{1}{2\pi\rho^2} (c_1 d_2 - c_2 d_1), \quad (3.18)$$

$$\rho^2 = c_\alpha c_\alpha + 2c_\alpha d_\alpha x + d_\alpha d_\alpha x^2, \quad (3.19)$$

and a contribution to the winding number

$$N_w^{\text{peak}} \equiv \int_{-\infty}^{\infty} dx n_w = \frac{1}{2} \text{sgn}(c_1 d_2 - c_2 d_1) = \pm \frac{1}{2}. \quad (3.20)$$

We have extended the integral to $\pm\infty$, but of course, the linear approximation breaks down somewhere and the integral is to be interpreted as the contribution from a peak in the winding density.

THREE DIMENSIONS

In this subsection we introduce half-knots for the three dimensional case. As in the one dimensional case we parameterize the Higgs field by real fields

$$\Phi = \frac{1}{\sqrt{2}} (\phi_4 1 + i\phi_a \tau^a), \quad (3.21)$$

A simple example is a configuration that can locally be approximated by Fourier modes:

$$\phi_\alpha(x) = \sin(\mathbf{x} \cdot \mathbf{k}_\alpha - \epsilon_\alpha), \quad \alpha = 1, \dots, 4. \quad (3.22)$$

The Higgs length $\sqrt{\phi_\alpha \phi_\alpha}$ will be small near the origin if all the $\epsilon_\alpha \ll 1$. In order to get a local minimum and not a long streamline of small Higgs length, the vectors \mathbf{k}_α should span three dimensional space. In figure 3.3 we plotted the Higgs length and the winding number density as a function of $x = x^1$ and $y = x^2$, in a slice through $z = x^3 = 0.05$, for the case

$$\mathbf{k}_1 = (1, 0, 0), \quad \mathbf{k}_2 = (0, 1, 0), \quad \mathbf{k}_3 = (0, 0, 1), \quad \mathbf{k}_4 = (0, 0, 1), \quad \epsilon_1 = \epsilon_2 = \epsilon_3 = 0.1, \quad \epsilon_4 = 0. \quad (3.23)$$

The integrated winding number in a box $x, y, z \in [-0.5, 0.5]$ around the peak is found to be 0.43, and it does not depend strongly on the integration volume.

The 3D half-knot may be formalized similar to the 1D case by using a linear approximation in a region where the Higgs length ρ is small (on the scale of m_H),

$$\phi_\alpha(\mathbf{x}) = c_\alpha + d_{\alpha k} x^k. \quad (3.24)$$

Then the winding number density is given by

$$n_w = \frac{1}{12\pi^2\rho^4} \epsilon_{jkl}\epsilon_{\alpha\beta\gamma\delta} \partial_j\phi_\alpha \partial_k\phi_\beta \partial_l\phi_\gamma \phi_\delta, \quad (3.25)$$

and in the linear approximation this gives

$$n_w = \frac{1}{2\pi^2\rho^4} \det M, \quad (3.26)$$

where M is the 4×4 matrix consisting of the column vectors $d_{\alpha 1}, d_{\alpha 2}, d_{\alpha 3}, c_\alpha$,

$$\det M = (1/6)\epsilon_{jkl}\epsilon_{\alpha\beta\gamma\delta} d_{\alpha j} d_{\beta k} d_{\gamma l} c_\delta. \quad (3.27)$$

The integral over the winding density can be done by shifting coordinates, $\mathbf{x} \rightarrow \mathbf{x}'$,

$$x^k = x'^k - g^{kl} d_{\alpha l} c_\alpha, \quad (3.28)$$

where g^{kl} is the inverse of f_{kl} defined by

$$f_{kl} = d_{\alpha k} d_{\alpha l}, \quad g^{kl} f_{lm} = \delta_m^k. \quad (3.29)$$

In terms of the shifted coordinates we have

$$\phi_\alpha = c'_\alpha + d_{\alpha k} x'^k, \quad c'_\alpha = c_\alpha - d_{\alpha k} g^{kl} d_{\beta l} c_\beta, \quad c'_\alpha d_{\alpha k} = 0, \quad (3.30)$$

and the length of the Higgs field is given by

$$\rho^2 = c'_\alpha c'_\alpha + f_{kl} x'^k x'^l. \quad (3.31)$$

The winding number of the half-knot equals

$$\int d^3x n_w = \frac{1}{2} \text{sgn} \det M = \pm \frac{1}{2}. \quad (3.32)$$

Since f_{kl} is a positive matrix, the center (maximum winding-number density) of the half-knot is at $\mathbf{x}' = 0$, and it has an ellipsoidal shape (surface of constant n_w). Its energy density has a constant contribution from the gradients, $\frac{1}{2}\partial_k\phi_\alpha\partial_k\phi_\alpha = \frac{1}{2}d_{\alpha k}d_{\alpha k}$, whereas the contribution from $\frac{1}{4}\lambda(\rho^2 - v^2)^2$ drops off away from the center.

When ρ vanishes in the center as a consequence of dynamics, so when the vector c_α vanishes, the winding number may or may not flip sign, depending on how the vector c_α recovers from zero. A pure-Higgs half-knot can decay by spreading. With a gauge field present, the Chern-Simons number may adjust to the winding number locally, such that the difference between winding and Chern-Simons number essentially vanishes.

Half-knots occur generically near the moment textures decay by changing their winding number, or near sphaleron transitions, because at these moments the Higgs length vanishes at a point. But half-knots are more general, for example, they occur in random field configurations, e.g. initial conditions for classical evolution. It is not clear yet at this stage that they are relevant, but in the simulations we will see that they are.

3.3 WINDING IN THE TACHYONIC TRANSITION

In this section we discuss the evolution of winding number and Chern-Simons number in a fast tachyonic transition. First we will review the relevant features of such a transition. After that we will discuss the importance of half-knots and differentiate between early and late half-knots.

3.3.1 TACHYONIC TRANSITION

At the onset of the tachyonic transition, when the effective mass parameter μ_{eff}^2 of the Higgs field changes sign, the universe is assumed to be in a homogeneous state with $\langle \Phi \rangle \approx 0$. As $\mu_{\text{eff}}^2 \rightarrow -\mu^2$, the Higgs potential becomes unstable near the origin and the low momentum modes of Φ grow very fast. Since the couplings in the Standard Model are fairly weak, it makes sense to study this process neglecting interactions. In this approximation the Fourier modes of the Higgs field satisfy

$$\ddot{\Phi}_\alpha(\mathbf{k}, t) + [\mu_{\text{eff}}^2(t) + \mathbf{k}^2]\Phi_\alpha(\mathbf{k}, t) = 0, \quad (3.33)$$

which can be solved exactly for the initial stage where $\mu_{\text{eff}}^2 \approx -M^3 t$ [87, 79] (choosing $t = 0$ as the onset of the transition). It turns out that the unstable field modes, i.e. the modes with $\mathbf{k}^2 < -\mu_{\text{eff}}^2$ grow very fast; the number of unstable modes also grows when $-\mu_{\text{eff}}^2$ increases.

INTERACTIONS

An estimate for the moment that interactions set in is given by the time that the average Higgs field reaches the point where the second derivative of the potential vanishes. This is around $m_{\text{H}} t = 4.8$ for an instantaneous quench and $m_{\text{H}}/m_W = \sqrt{2}$ [61]. There are both self-interactions of the Higgs field and interactions with the gauge field. The self-interactions slow down the growth of the Higgs field, and eventually lead to an oscillation near the vacuum state. The interactions with the gauge fields lead to a strong growth of the gauge fields [59, 60]. The oscillation of the Higgs field is damped by the interactions, and when more fields are added in a realistic situation, this suppression is expected to be even stronger. Eventually the energy will be distributed over all modes, and the system thermalizes.

INSTANTANEOUS QUENCH

As in [58, 59, 61], we make in this chapter the approximation that the change of the potential is instantaneous in order to obtain the most dramatic effects,

$$\begin{aligned}\mu_{\text{eff}}^2(t) &= +\mu^2, t < 0, \\ &= -\mu^2, t > 0.\end{aligned}\tag{3.34}$$

Moreover we do not consider the inflaton field in our simulations. In this quenching approximation the modes of the Higgs field grow exponentially fast [58, 61]:

$$\Phi_\alpha(\mathbf{k}, t) \propto \exp[\sqrt{\mu^2 - \mathbf{k}^2} t].\tag{3.35}$$

CLASSICAL APPROXIMATION

Another approximation that we use is the classical approximation. Intuitively one can see that the fields can be considered to be classical, because the Bose fields grow exponentially fast and the occupation numbers are therefore quickly much larger than one. For the gauge field the occupation numbers become substantial only after the Higgs current in its equation of motion has grown sufficiently large, which typically takes a few m_{H}^{-1} units of time [59]. The approximation is implemented as follows [58, 61]. Before the instantaneous quench the fields are in the zero-temperature ground state corresponding to positive $\mu_{\text{eff}}^2 = \mu^2$. With neglected interactions this corresponds to a Gaussian distribution, which can be followed until it becomes classical and a switch to classical evolution can be made. However, because quantum and classical evolution are formally the same for Gaussian systems (so systems without interactions), this switch can already be made directly after the quench at time zero. The classical evolution is computed from the fully non-linear equations of motion, including the interactions. Making the switch early on also enables a more gradual inclusion of the effect of the interactions. We draw a number of Higgs field configurations from the classical part of the Gaussian distribution, and take these configurations as initial conditions for the system after the quench. For simplicity, the initial gauge potentials are set to zero, whereas the $SU(2)$ electric fields are calculated from Gauss' law [61]. Then we evolve each of these configurations according to the classical equations of motion. In the end we compute expectation values by averaging over the initial distribution.

The classical approximation for a tachyonic transition has been compared with quantum methods like the 2PI-method in [88], and it turned out that the two approximations agreed for the times and couplings used here, giving further support for both.

3.3.2 WINDING AND CHERN-SIMONS NUMBER DENSITIES

In the initial conditions for the tachyonic transition the gauge fields are negligible, and since the gauge potentials are zero in our implementation, the Chern-Simons number density is zero. The Higgs field initially has fluctuations around zero and therefore it has nonzero winding number density. Since the initial conditions are random, the winding number density will be randomly distributed over the volume. The total winding number in the volume will be integer and does not have to be zero.

When the system thermalizes and the temperature decreases, the Chern-Simons number will approach the winding number. If the winding number would not change during the process, the Chern-Simons number, approaching the initial winding number, would be determined by the initial conditions, and CP violating interactions could not influence the final outcome.

In reality the winding number does change during the process, and this makes it possible that CP violation creates an asymmetry. The winding number can change when the Higgs length becomes zero in a point, and as we argued in the previous section there will be half-knots around such points. There are two periods when the Higgs has a chance to be small and change of winding is likely to occur: early in the transition when the Higgs field starts from a small fluctuation, and later on, when the Higgs length bounces back due to its self-interaction, or just any interactions, e.g. scattering of non-linear waves.

In both periods half-knots will occur; we call them early and late half-knots respectively.

3.3.3 EARLY HALF-KNOTS

In the initial conditions of the tachyonic transition, the Higgs field has small fluctuations around zero. The number density of minima of the Higgs length is, depending on the initial conditions, roughly proportional to k_{\max}^3 where k_{\max} is the largest wavenumber that is initialized. Because of the peculiar feature of the tachyonic transition that modes grow faster as their wavelengths are larger, this number density of minima will quickly decrease. Hence initially there are many half-knots, but their number quickly decreases.

Some half-knots will manage to survive longer. When a half-knot still exists when the gauge fields start to become important, the Chern-Simons number density in these regions can adjust to the winding number density. When the Chern-Simons number becomes approximately equal to the winding number in a blob, the covariant derivative $D_i \Phi$ becomes small, the gradient energy diminishes and the half-knot becomes stable.

The early half-knots are perhaps not so important for baryogenesis. In principle CP violation could cause an imbalance in the formation and decay of the number of half-knots and anti-half-knots. However in this early period there are no interactions yet, and

CP violation cannot have acted. Also when the early half-knots stabilize and survive CP violation is not important because then the winding number does not change. So we expect that we should look at the late half-knots for possible effects of CP violation.

3.3.4 LATE HALF-KNOTS

The Higgs length can also become small later in the transition. For example this can happen when the Higgs field bounces back in its potential, or because of interactions in general. In this case there will be late half-knots in which the winding can change. Because interactions are important to create these half-knots, also CP violating interactions can influence this process. There may also be longer lived half-knots, not stabilized by the gauge fields, whose probability to decay is influenced by the stronger CP violation at later times.

3.4 NUMERICAL SIMULATIONS

In this section we first describe briefly the setup of our simulations, and then present the results.

3.4.1 SETUP

In [61] numerical simulations were described with the $SU(2)$ Higgs model, using the approximations described in section 3.3.1, and with an extra CP violating term in the action. For the present work we extended the computer code of [61] to be able to observe the winding number density and a local quantity n_{CS} closely related to the Chern-Simons number density (see below). We do not use the CP violation of the code of [61] because at this point we are interested in the mechanism of winding number and Chern-Simons number production, and not yet in the creation of the asymmetry.

The simulation was performed on a 60^3 lattice, with periodic boundary conditions and with a lattice spacing of $0.35 m_H^{-1}$, such that the physical volume was $L^3 = (21 m_H^{-1})^3$. The initial conditions mentioned in 3.3.1 are the “just-a-half” initial conditions as defined in [58, 61]. Effectively this means that only the growing modes, with momentum k smaller than μ , are initialized with probability given by the vacuum state. Furthermore we took $\lambda/g^2 = 1/4$, which is equivalent to $m_H/m_W = \sqrt{2}$. (We shall also present some results for $m_H/m_W = 2$.) For the determination of the initial conditions, which are set by quantum fluctuations, we also have to fix g^2 . We chose $g^2 = 4/9$. See [61] for more details on the numerical implementation.

The density n_{CS} is defined as

$$n_{\text{CS}}(\mathbf{x}, t) = \int_0^t dt' q(\mathbf{x}, t'), \quad (3.36)$$

where q is the gauge-invariant topological charge density given in (3.8). Since $q = \partial_\mu j_{\text{CS}}^\mu$ and the Chern-Simons current is zero for our initial conditions,

$$n_{\text{CS}}(\mathbf{x}, t) = j_{\text{CS}}^0(\mathbf{x}, t) + \partial_k \int_0^t dt' j_{\text{CS}}^k(\mathbf{x}, t'). \quad (3.37)$$

So n_{CS} differs from j_{CS}^0 by a divergence and they both integrate to N_{CS} . In the following we shall call n_{CS} the Chern-Simons density, for simplicity, but it should be kept in mind that it is not equal to j_{CS}^0 .

3.4.2 RESULTS

ONE TYPICAL TRAJECTORY

In order to investigate classical field configurations we look at single trajectories. In this subsection we consider one typical trajectory.

Total N_w and N_{CS} as function of time in a typical run. The variables considered in [61] were the spatial average of the Higgs length squared

$$\overline{\rho^2} = L^{-3} \int d^3x \rho^2, \quad (3.38)$$

the winding number N_w and the Chern-Simons number N_{CS} . In figure 3.4 we show the evolution of these variables in time for our typical trajectory, from $m_{\text{H}}t = 0$ up to $m_{\text{H}}t = 30$. The winding number N_w fluctuates initially, and later stays put at an integer. The initial fluctuations indicate that there must be zeroes in the Higgs length. In the continuum these fluctuations would be between integers (a ‘devil’s staircase’), but here they appear as smoothed out by the lattice discretization.

We also see that the Chern-Simons number starts only when the average Higgs length is already rather large, and that at the later times $N_{\text{CS}} \approx N_w$. (Occasionally we also have seen trajectories for which the two differed at $m_{\text{H}}t = 30$ by a number of order 1, and only at much later times N_{CS} approached N_w (sometimes this took as long as $m_{\text{H}}t \approx 500$)).

3D pictures of n_w and n_{CS} . Next we look at the densities of the winding number and Chern-Simons number in this trajectory. Figure 3.5 displays the winding number density

in the three dimensional simulation volume from times $m_{\text{H}t} = 1$ to $m_{\text{H}t} = 15$. Note that the box has periodic boundary conditions. Red indicates positive density, blue negative. In the beginning there are many ‘blobs’ in winding number density. We will argue below for two specific cases that these blobs are half-knots with a small Higgs length ρ in their center. Sometimes they change sign. The number of blobs decreases first until approximately time $m_{\text{H}t} = 9$, then it increases until approximately $m_{\text{H}t} = 13$ after which it decreases again. Some of the early blobs that are there already from the beginning survive all the time. The blobs that appear after time $m_{\text{H}t} = 9$ seem to be uncorrelated to the blobs that were there before. We call these new blobs the late blobs.

In figure 3.6 the Chern-Simons number density is shown from times $m_{\text{H}t} = 7$ to $m_{\text{H}t} = 15$. Before $m_{\text{H}t} = 7$ the Chern-Simons number density is negligibly small. Also in the Chern-Simons number density there are blobs. These blobs are correlated with the winding number blobs.

Small Higgs length means a lot of winding. We argued above that regions with small Higgs length have typically a large winding number density. This is confirmed in the simulations. In figure 3.7 the absolute value of the winding number density $|n_{\text{w}}|$ is plotted versus the normalized Higgs length $(\rho/v)^2$ for each point on the lattice. The configuration of the typical trajectory at time $m_{\text{H}t} = 6$ is used, when the gauge fields are still unimportant. We see that $|n_{\text{w}}|$ and $(\rho/v)^2$ are correlated such that, when the Higgs length on a lattice point is small, the winding number density is typically large.

A consequence of this correlation is that when the average Higgs length is small, there will typically be more winding blobs. We saw this already in the three dimensional pictures of the winding number density: there were less winding blobs around time $m_{\text{H}t} = 8$, when the average Higgs length is large. We can show this more quantitatively, by plotting [89] $\int d^3x |n_{\text{w}}|$ in figure 3.8. We see in this figure that the peak in $\int d^3x |n_{\text{w}}|$ at $m_{\text{H}t} \approx 20$ is much smaller than the corresponding one at $m_{\text{H}t} \approx 12$. This agrees with the fact that there are much less lattice points with small Higgs length at $m_{\text{H}t} = 20$. We can also see this from the histograms in figure 3.9. Below we will refer to blobs that are created in the n th minimum of the Higgs length as n th generation blobs.

Correlation between winding number and Chern-Simons number. Because the Higgs and gauge fields interact, n_{w} and n_{CS} are correlated. This could already be seen in the three dimensional pictures, but we can also calculate the correlation

$$C(\mathbf{r}, t) = \frac{\int d^3x [n_{\text{CS}}(\mathbf{x}, t) - \overline{n_{\text{CS}}}(t)][n_{\text{w}}(\mathbf{x} + \mathbf{r}, t) - \overline{n_{\text{w}}}(t)]}{\sqrt{\int d^3x [n_{\text{CS}}(\mathbf{x}, t) - \overline{n_{\text{CS}}}(t)]^2} \sqrt{\int d^3y [n_{\text{w}}(\mathbf{y}, t) - \overline{n_{\text{w}}}(t)]^2}}, \quad (3.39)$$

where the ‘over-bar’ denotes the spatial average, as in (3.38). This correlator is plotted versus $r = |\mathbf{r}|$ at various times in figure 3.10. It shows a spatial correlation developing on

distances of order m_H^{-1} , modulated in time and showing a tendency to diminish at later times.

It is also instructive to plot its value at $r = 0$ versus time, see figure 3.11. We see that the correlation $C(\mathbf{0}, t)$ develops already at early times, it peaks at times $m_H t \approx 12$ and 16, and there is a rapid drop after the first peak. This drop occurs when the average Higgs length has become small after its first maximum, and $\int d^3x |n_w|$ is on the rise again (cf. figure 3.7). We interpret this as being caused by the creation of many new winding blobs when the Higgs length is small again, for which n_w is still uncorrelated with n_{CS} . When $C(\mathbf{0}, t)$ peaks for a second time the average Higgs length is large again and $\int d^3x |n_w|$ is low. We suspect that this is because the winding blobs that still exist when the average Higgs length is large, exist already for some time and the Chern-Simons number density has had some time to adjust. Later on the correlation decreases, which is presumably caused by random fluctuations.

In the following two subsections we zoom in on two blobs, first on an early blob and then on a late survivor.

EARLY BLOB

For the early blob we take the one indicated by the arrow in figure 3.12. Let us first look at the distributions of the Higgs length and the winding number density in this blob. In a vertical slice in the xz -directions through the center of the blob, the Higgs length and the winding number density are plotted in figure 3.13, at time $m_H t = 2$. The Higgs length has a minimum and the winding number has a large peak at this minimum. These figures look very similar to the analytical example in figure 3.3.

Next we have calculated the sums of some quantities in a ball around the center of the blob. For this we had to determine the position of the center, which is slightly ambiguous. We did it by defining the center as the point where the winding number density is maximal. The position of the center can change a bit at different times, so we determined the center at each time step. In the left panel of figure 3.14 we show the integrated winding number density

$$N_w^{\text{ball}} = \int_{\text{ball}} d^3x n_w, \quad (3.40)$$

integrated Chern-Simons number density

$$N_{CS}^{\text{ball}} = \int_{\text{ball}} d^3x n_{CS}, \quad (3.41)$$

and the volume-averaged Higgs length

$$\overline{\rho^2}^{\text{ball}} = \int_{\text{ball}} d^3x \rho^2 / \int_{\text{ball}} d^3x 1, \quad (3.42)$$

for a ball of radius 6 lattice units, corresponding to $2.1 m_H^{-1}$, as a function of time. For reference the Higgs length averaged over the full simulation volume is also shown.

The winding number in the ball first decreases until $m_H t = 5$, then increases until $m_H t = 10$ and afterwards stays approximately constant near a value of 0.3. The Chern-Simons number becomes visible from $m_H t \approx 8$ onwards, has a small peak and stays constant near 0.2 after $m_H t \approx 13$. The winding number and Chern-Simons number end up being close to each other. The average Higgs length in the ball grows only much later than the one in the full volume, and also oscillates with a somewhat higher frequency. It also exhibits much less damping, which is suggestive of oscillons [90, 91].² We will comment later on the dip in the winding number at time $m_H t = 5$.

The right panel of figure 3.14 shows the energy in the same ball with radius $2.1 m_H^{-1}$. We display the excess energy above the average energy relative to the sphaleron energy, i.e. $\int_{\text{ball}} d^3x (\epsilon - \bar{\epsilon})/E_{\text{sph}}$, where ϵ is the energy density and $\bar{\epsilon}$ its average over the total volume. The average energy density is simply that of the origin of the Higgs potential, $\bar{\epsilon} = m_H^4/16\lambda$, and the sphaleron energy for $m_H = \sqrt{2} m_W$ is $E_{\text{sp}} \approx 3.78 (4\pi m_W/g^2)$ (see e.g. [92]), and so $\int_{\text{ball}} d^3x \bar{\epsilon}/E_{\text{sp}} \approx 0.29$. Hence, the sphaleron energy in this plot is at 0.71.

We show the total energy in the ball as well as its contributions from the Higgs and the gauge fields (the contribution from the covariant derivative is allocated to the Higgs fields). We see that the gauge fields contribute most to the energy. It is remarkable that the peak in the total energy occurs at a time where the average Higgs length in the ball has its first maximum, that the peak is significantly higher than the sphaleron energy, and that the energy has already fallen back to the average already shortly after $m_H t = 15$. Evidently, a strong energy flow into and out of the ball is taking place. At the later times $N_{\text{CS}}^{\text{ball}}$ has roughly the same value as $N_{\text{w}}^{\text{ball}}$.

To see how these results depend on the radius of the ball we show in figure 3.15 the winding number and Chern-Simons number in balls with increasing radii, from 3 up to 15 lattice units. They clearly depend on the radius, and for the larger balls $N_{\text{w}}^{\text{ball}}$ increases above 1/2. This may be caused by another blob of the same sign that is close (cf. figure 3.5, e.g. at time $m_H t = 15$ the distance between the centers of the two blobs is about 13 lattice units).

Here we return to the dip that we observed at $m_H t = 5$ in figure 3.14. From figure 3.15 we see that the dip is also there for larger radii of the ball; apparently the winding number is not flowing out of the ball, but is really decreasing. In the continuum this can only occur when the Higgs length ρ is exactly zero somewhere. But on the lattice we will

²The Higgs mode of the ideal oscillon found [91] for $m_H = 2 m_W$ oscillates at a slightly lower frequency than $m_H/2\pi$ but in our case the effective Higgs mass will be lowered by a non-zero effective temperature in the bulk.

miss already a significant amount of winding number when the spatial size of the winding number peak becomes smaller than a lattice unit. Hence we interpret the observed dip as a lattice artefact, signaling a half-knot in the center of which the Higgs length decreases (which makes the peak sharper) until $m_{\text{H}}t = 5$, and increases again after that.

Further insight can be obtained from the profiles of the Higgs length and the winding-number density around the center of the blob, $\rho(r)$ and $n_{\text{w}}(r)$. They are plotted in figures 3.16 and 3.17, for times $m_{\text{H}}t = 1$ to 10. The profiles are determined by averaging at fixed distances r from the center over all directions. For the position of the center we used the same values as in figure 3.14.

From the Higgs length profiles we see that, while the Higgs length in the bulk grows steadily from the beginning, in the center of the blob it remains very small up to time $m_{\text{H}}t \approx 6$, and starts to grow only after that. At the latest time $\rho(r)$ looks like an oscillation about the equilibrium value. The winding number density profile is already well defined at time $m_{\text{H}}t = 1$. It then shrinks and becomes steeper towards the center, $m_{\text{H}}t = 2$ and 3. This shrinking and steepening appears to get blurred by lattice artefacts at $m_{\text{H}}t = 4, 5, 6$ (note that the profiles here are shown on a much smaller scale than the ρ -profile in figure 3.16), and as mentioned earlier, we believe this is the reason for the dip in $N_{\text{w}}^{\text{ball}}$ at $m_{\text{H}}t = 5$. From time $m_{\text{H}}t = 10$ the winding number profile broadens.

We conclude that we have witnessed the formation of a half-knot, that nearly decayed by shrinking, but got ‘saved’ by the gauge field adjusting its Chern-Simons number density and diminishing the Higgs gradient density $|D_i\Phi|^2$. Remarkably, this adjustment goes together with a big jump in gauge-field energy. At later times the well-dressed blob carries no excess energy, and the process has led to a local change in the total Chern-Simons number.

LATE TRANSITION

Above we have seen (in the three dimensional pictures 3.5, 3.6 and the $|n_{\text{w}}|$ graph 3.8) that new blobs are created when the average Higgs length is small. Sometimes the winding number N_{w} changes in such a blob. Here we present an example of such a late blob in which the winding number changes. It comes from another trajectory than the one used before. Figure 3.18 shows the evolution of $\overline{\rho^2}$, N_{w} and N_{CS} in this run up to time $m_{\text{H}}t = 30$. Note that the winding number changes from -1 to 0 between $m_{\text{H}}t = 23$ and $m_{\text{H}}t = 24$. This change takes place in the blob that we are going to consider.

Figure 3.19 shows 3D plots of the winding and Chern-Simons number densities at times $m_{\text{H}}t = 23$ and 24. The change of the winding number occurs in the blob that changes sign at the top of the box. At the same position there is a positive Chern-Simons number density both before and after the change of winding number.

In figure 3.20 the Higgs length and the winding number density in a horizontal slice through the blob are shown for times $m_H t = 23$ and $m_H t = 24$. There is a pronounced minimum in the Higgs length at the place of the peak in the winding number density. The latter changes quite abruptly from negative to positive.

Next we plot N_w^{ball} , $N_{\text{CS}}^{\text{ball}}$ and $\overline{\rho^2}^{\text{ball}}$ for a ball of radius 6 in lattice units ($2.1m_H^{-1}$) as a function time in the left panel of figure 3.21. The average Higgs length in the ball is approximately in anti-phase with the average Higgs length in the full volume, and there appears to be no damping, suggesting as in figure 3.14 a connection with the oscillon phenomenon [90, 91]. The winding number flips sign around $m_H t = 2$ and becomes negative. Then it makes limited excursions, even at the times where there are large peaks in $\overline{\rho^2}^{\text{ball}}$, but between times $m_H t = 23$ and $m_H t = 24$ it makes a rapid jump by about $+0.6$, a substantial part of 1 for this relatively small ball. At this point $\overline{\rho^2}^{\text{ball}}$ has a minimum. The Chern-Simons number of the ball does not follow the winding number very much. It shows mild negative peaks at $m_H t = 9$ and 18, shortly before the peaks in $\overline{\rho^2}^{\text{ball}}$, and between $m_H t = 18$ and 30 it gradually increases by about 0.6 (about the same as the jump in N_w^{ball} at $m_H t = 23$). In the right panel of figure 3.21 the total energy in the ball and the contributions from the gauge and the Higgs fields are plotted versus time. As in figure 3.14, we display the excess energy above the average, and with respect to the sphaleron energy. The contribution from the gauge fields is again dominant in the first two peaks (which coincide with the peaks in $\overline{\rho^2}^{\text{ball}}$), but at $m_H t = 23$ (where $\overline{\rho^2}^{\text{ball}}$ has a minimum) the Higgs energy clearly dominates. There is a moderate rise of the energy between $m_H t = 22$ and 27. Given that the subtracted energy is about $0.29 E_{\text{sp}}$, its maximum value is about 15% higher than the sphaleron energy. The N_w^{ball} and $N_{\text{CS}}^{\text{ball}}$ data for balls with increasing radii are given in figure 3.22. The result is comparable to the early blob: both the winding number and the Chern-Simons number increase with increasing radius, indicating that there is not a sharp boundary of the blob. However, the sharp rise in N_w^{ball} between $m_H t = 23$ and 24, and the steady increase of $N_{\text{CS}}^{\text{ball}}$ after $m_H t = 18$, are present for all ball radii.

Figures 3.23 and 3.24 show the profiles of the Higgs length and the winding number density, from times $m_H t = 19$ to $m_H t = 27$. The Higgs length at the center is decreasing and apparently developing a zero at time $m_H t = 23$, when the winding number changes, and after that it increases again. The winding profile becomes very steep around this time, as we saw also in figure 3.20. Lattice artefacts do not seem to be prominent in this case. Afterwards the winding density spreads and becomes very small.

The transition at $m_H t = 23$ bears the hallmarks of a sphaleron transition: a gradual $O(1)$ increase in N_{CS} and an $O(1)$ jump in N_w , which occur locally in a blob, in the center of which ρ goes through zero, together with a gradual increase in $N_{\text{CS}}^{\text{ball}}$ and a switch of sign in N_w^{ball} . The energy at that time in the ball of radius $2.1 m_H^{-1}$ ($1.5 m_W^{-1}$) is also reasonably close to the sphaleron value ($\approx 0.9 E_{\text{sp}}$). The properties of the subsequent

maximum at $m_H t = 27$ look rather similar to the two earlier ones, in its dominance of the gauge-field energy and the accompanying maxima in $\overline{\rho^2}^{\text{ball}}$.

3.4.3 DISTRIBUTIONS AND SUSCEPTIBILITIES

Here we present some quantitative results for the late distribution of winding numbers, and for the growth of the Chern-Simons susceptibility $\langle N_{\text{CS}}^2 \rangle$ during the transition. The winding-number distribution is expected to be Gaussian for large volumes, but its volume dependence may contain non-trivial deviations. The rate of change of the Chern-Simons susceptibility has been interpreted as an effective sphaleron rate and used [60] to estimate the asymmetry induced by CP violation. In this section we also show results for mass ratio $m_H = 2m_W$, in addition to the value $m_H = \sqrt{2}m_W$ used throughout this article. We vary m_H/m_W by varying the Higgs self coupling λ while keeping fixed the gauge coupling g^2 , the volume in Higgs mass units, $(m_H L)^3$, and the lattice spacing in Higgs mass units, am_H .

WINDING DISTRIBUTION

Figure 3.25 shows the normalized distribution of winding numbers at $m_H t = 50$ obtained from a sample of about 2000 initial conditions for each parameter set. Three fits to the data are shown as well, one based on a Gaussian and two models based on generation via winding blobs. In a first approximation we treat such blobs as being dilute and independent, which means that in a sufficiently large volume the probability for n blobs is $p_n = cr^n/n!$, where c is a normalization constant following from $\sum_n p_n = 1$. For $n = 1, 2, \dots$ this gives $c = e^{-r}$, and r is the average number of blobs, which is proportional to the volume.

From a Kibble mechanism viewpoint one might expect each blob to contribute one unit to the winding number. For n blobs there may be k blobs contributing $+1$ and $n - k$ blobs contributing -1 , such that the winding number is $N = k(+1) + (n - k)(-1) = 2k - n$. Assuming a probability a for $+1$ and $(1 - a)$ for -1 , the probability for winding number N would be given by

$$P_N = \sum_{n=0}^{\infty} p_n \sum_{k=0}^n \binom{n}{k} \delta_{2k-n, N} a^k (1-a)^{n-k} = e^{-r} \left(\frac{a}{1-a} \right)^{N/2} I_N(2r\sqrt{a(1-a)}), \quad (3.43)$$

where I_N is the usual Bessel function. In our case of no CP violation, $a = 1/2$, and

$$P_N^{(1)}(r) = e^{-r} I_N(r). \quad (3.44)$$

For $r \gg 1$ this becomes indistinguishable from a Gaussian,

$$P_N^{\text{Gauss}}(\sigma) = \frac{1}{\sqrt{2\pi\sigma^2}} e^{-N^2/2\sigma^2}, \quad (3.45)$$

with $\sigma \approx r$.

However, we have argued and presented evidence that in a tachyonic quench the initial winding blobs are half-knots, some of which become stabilized by the gauge field and pick up a Chern-Simons number equal to their winding number $\pm 1/2$. So their initial winding number is conserved, although they later decay by spreading. This suggests that we modify the above model by taking into account the half integer winding of the blobs. Since the total winding number is integer, we could modify the above reasoning by assuming that in case n is odd, there is a compensating contribution $\pm 1/2$ somewhere in the volume, writing $N = k(+1/2) + (n - k)(-1/2) \pm 1/2$, with equal probability $1/2$ for the \pm sign. The even- n contribution to P_N is unmodified. This gives

$$P_N^{(1/2)}(r) = e^{-r} \left[I_{2N}(r) + \frac{1}{2} I_{2N+1}(r) + \frac{1}{2} I_{2N-1}(r) \right]. \quad (3.46)$$

Alternatively, we can model the compensating $\pm 1/2$ contribution by a half-knot and only allow even n , such that $p_n \rightarrow r^n/n! \cosh r$, which leads to the simpler form

$$P_N^{(1/2)}(r) = I_{2N}(r) / \cosh(r). \quad (3.47)$$

The distributions P_N are normalized, $\sum_{N=-\infty}^{\infty} P_N = 1$.

The χ^2 values of the fit presented in the upper plot of figure 3.25 for the half-knot based model of equation (3.47) is clearly lower than the integer model and also the Gaussian model. For the model of equation (3.46) the result is comparable. For the lower plot the integer-knot model gives a better fit but the difference with the half-knot model is not significant ($\chi^2/\text{d.o.f.} = 1.3$ vs. 1.1). This we consider additional support for the relevance of half-knots in the tachyonic transition.

CHERN-SIMONS SUSCEPTIBILITY

Figure 3.26 shows the time dependence of $\langle N_{\text{CS}}^2 \rangle$ for the mass ratios $m_{\text{H}}/m_W = \sqrt{2}$ and 2. Both curves show an initial rapid rise, and the $\sqrt{2}$ case shows a deep dip near $m_{\text{H}}t = 13$. This is about the time where the average Higgs length also has its first minimum (actually approximately one m_{H}^{-1} unit later). At this time $\int d^3x |n_w|$ has risen again substantially (figure 3.8), and there is evidently no instantaneous connection with the winding number. The dip is much less pronounced (and shifted) for mass-ratio 2 case, presumably due to the stronger coupling λ , which implies a smaller initial energy density ($m_{\text{H}}^4/16\lambda$). We have seen that the dip in the average Higgs length is also less deep in

this case. This suggests fewer second-generation winding blobs, which may explain the quicker flattening of $\langle N_{CS}^2 \rangle$, compared to the $\sqrt{2}$ case. Correspondingly, the effective sphaleron rate $d\langle N_{CS}^2 \rangle/dt$ (e.g. averaged over an oscillation) will be substantial over a larger time span when m_H/m_W decreases.

An alternative interpretation for the first minimum in the susceptibility could be given in terms of N_{CS} bouncing back from a barrier in the potential of its effective equation of motion. The ρ -dependence of this barrier may even lead to resonant behavior [58, 61].

3.5 SUMMARY AND DISCUSSION

In the theory of baryogenesis the change of the Chern-Simons number of the $SU(2)$ gauge field plays an important role, and we studied the mechanism by which this can occur in a tachyonic electroweak transition. The tachyonic instability occurs initially in the Higgs field, and because of its coupling to the gauge field through the covariant derivative, one expects a correlation between the Chern-Simons number and the Higgs winding number. We argued that in a tachyonic transition there will be many places where the Higgs length is small in a typical field configuration. These places are important since the winding number can change when the Higgs length goes through zero, possibly under influence of CP violation, and this may also induce a change in the Chern-Simons number. On the other hand, small Higgs lengths imply small Higgs currents, which may limit their influence in the equation of motion of the gauge field. Regions with small Higgs length have in general a large winding-number density which is why we call them winding blobs.

The integrated winding number in these blobs does not need to be integer, and the basic objects have winding number close to $\pm 1/2$, the half-knots. When the dynamics causes the Higgs length to vanish in the center of a half-knot, its winding number may flip sign. Half-knot configurations occur also naturally during sphaleron transitions and decaying textures losing their winding number, since these have a moment at which the Higgs length vanishes at a point in space. The pure-Higgs half-knots can evaporate by increasing the Higgs length in the center, but they may also get ‘dressed’ by the gauge field adjusting its Chern-Simons number density locally to the winding. The configuration may then decay by spreading into the environmental fluctuations, and the half-knots have acted like local seeds of Chern-Simons number change.

We observed the winding blobs in numerical simulations of the tachyonic transition in the $SU(2)$ Higgs model. Because of their large winding number density, they are easy to spot. We indeed observed a strong correlation between the half-knot winding density with the Chern-Simons number density.³ The picture sketched above was supported by

³We recall that in our numerical simulation we actually used n_{CS} , which is a gauge-invariant modification of j_{CS}^0 with the same total Chern-Simons number.

the behavior of the integrated winding and Chern-Simons densities in small balls, as well as the radial profiles of the spherically averaged densities. Our findings for the profiles are similar to the one shown in [60].

We also analyzed an example of a realistic sphaleron transition. This occurred quite late in a blob that survived a relatively long time, showing signs of stability reminiscent of oscillons [90, 91]. In the present case we do not expect such objects to live very long as they will be destroyed by thermal fluctuations.

We found that the winding blobs can be divided into two classes. The early blobs are remnants from the initial conditions, and can sometimes survive when they are stabilized by the gauge fields. The late blobs occur when the Higgs length bounces back to small values, and there can be second, third, . . . , generations, especially for smaller Higgs self-couplings. Most of the early blobs are probably not important for CP violation, because interactions become important too late for them. CP violation can however affect the late blobs.

The distribution of Chern-Simons numbers is expected to be approached by the distribution of winding numbers when the volume becomes large. We studied the winding number distribution and found that it could be fitted by models based on half-knots, better than by a model based on integer components and even marginally better than a Gaussian, although for large volumes all the model-distributions are expected to become indistinguishable from a Gaussian.

Finally we presented new results on the susceptibility of Chern-Simons numbers, which has been used in estimates of the baryon asymmetry [60]. Some aspects of its dependence on the Higgs self-coupling could be interpreted in terms of generations of half-knots, but a detailed understanding is difficult. Nevertheless, we expect that the increased understanding obtained in this chapter is of use for modeling cold electroweak baryogenesis.

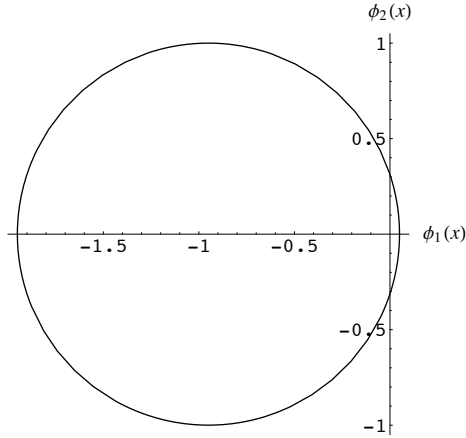


Figure 3.1: Parametric plot of $\phi_2(x)$ versus $\phi_1(x)$ for $x \in [-\pi, \pi]$, for the configuration of equation 3.16.

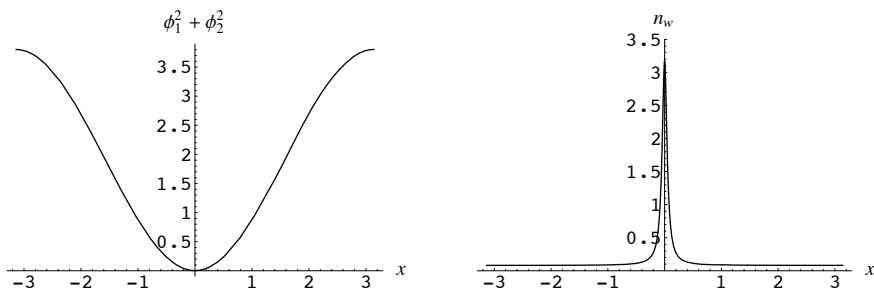


Figure 3.2: The Higgs length ρ^2 and the winding number density n_w for the configuration of equation (3.16) as function of x .

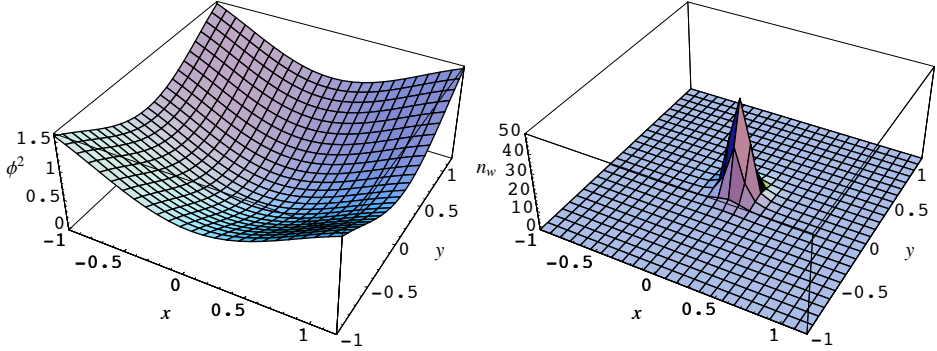


Figure 3.3: The Higgs length ρ^2 (left) and the winding number density n_w (right) for the configuration (3.22), (3.23), as function of x and y , with $z = 0.05$.

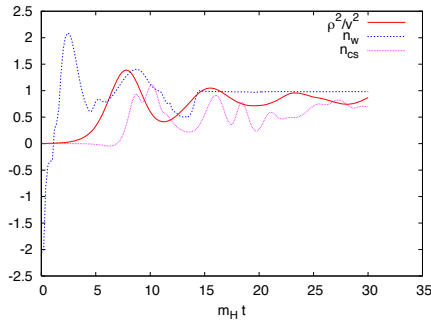


Figure 3.4: Results of a typical run for times $m_H t = 0$ to $m_H t = 30$. Plotted are $\overline{\rho^2}/v^2$, the total winding number N_w and total Chern-Simons number N_{CS} .

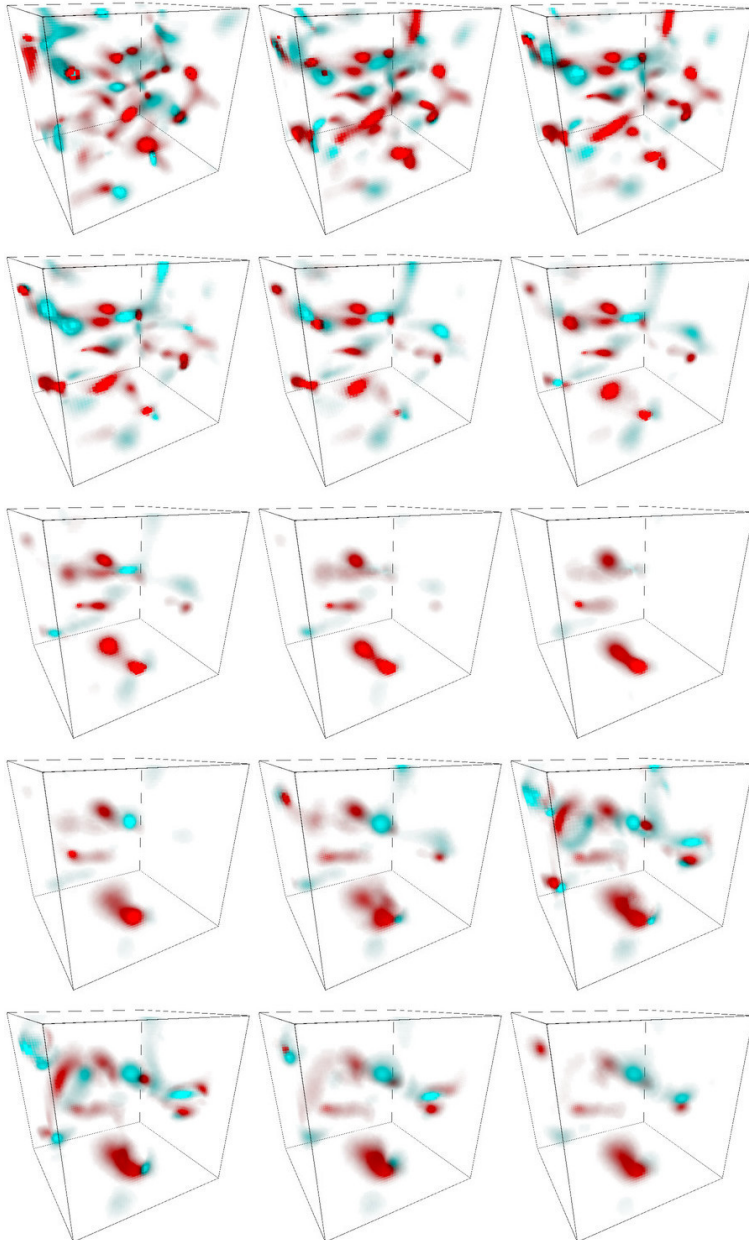


Figure 3.5: Winding number density n_w from $m_{Ht} = 1$ to $m_{Ht} = 15$. Red is positive, blue is negative.

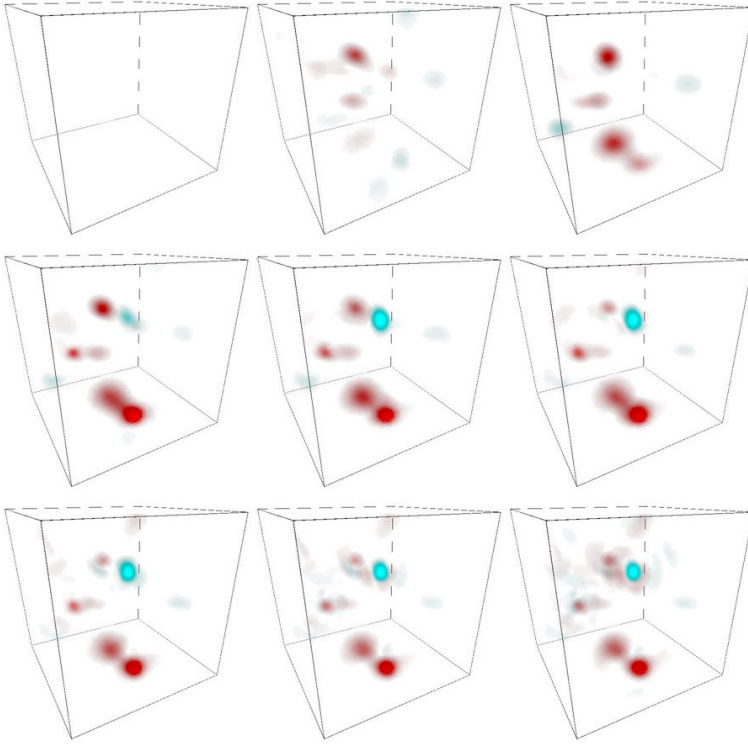


Figure 3.6: Chern-Simons number density n_{CS} from $m_{HT} = 7$ to $m_{HT} = 15$. Before $m_{HT} = 7$ the Chern-Simons number density is negligibly small. Red is positive, blue is negative.

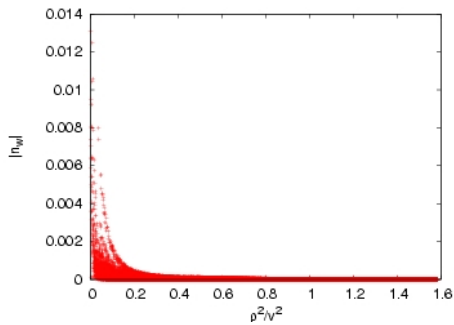


Figure 3.7: The absolute value of the winding number density $|n_w|$ versus the Higgs length for all lattice points in the simulation volume, at time $m_{HT} = 6$.

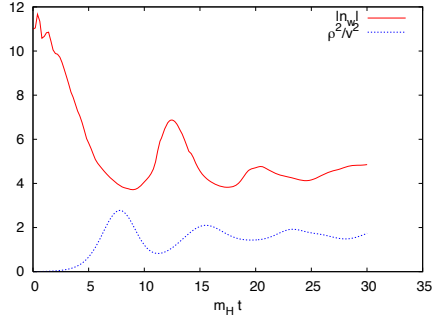


Figure 3.8: The integral $\int d^3x |n_w|^2$ and the spatial average of the squared Higgs length versus $m_H t$.

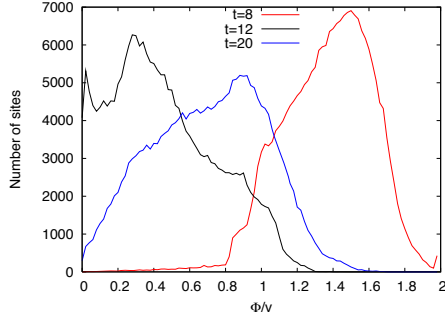


Figure 3.9: Histograms that display the distribution of the Higgs length on the lattice at times $m_H t = 8, 12$ and 20 .

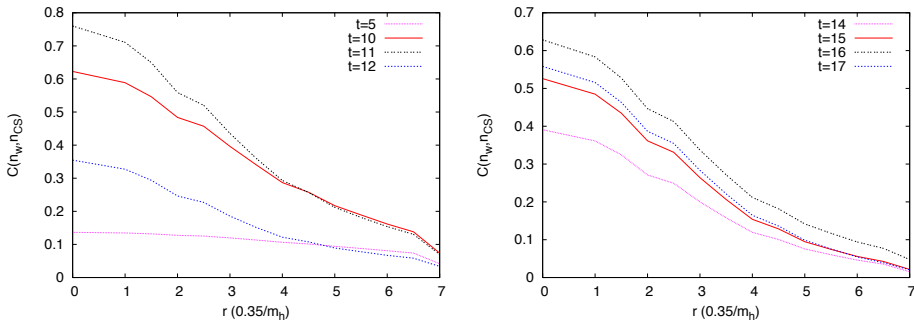


Figure 3.10: The correlation $C(\mathbf{r}, t)$ between n_{CS} and n_w , defined in (3.39), versus $r = |\mathbf{r}|$ at various times.

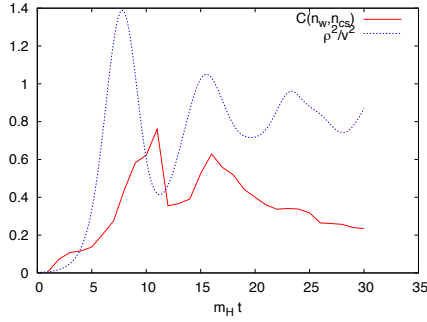


Figure 3.11: The correlation $C(0, t)$ versus time.

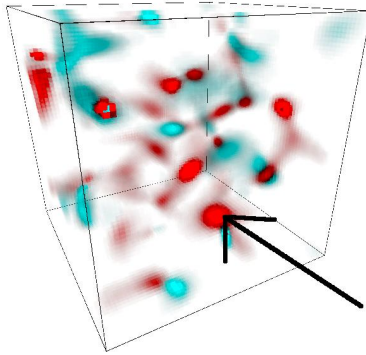


Figure 3.12: The winding number density at time $m_H t = 1$ of the same run as used before. The blob that we consider in this section is indicated by the arrow.

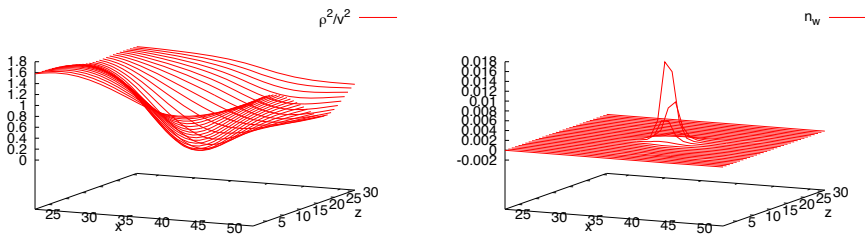


Figure 3.13: Left the Higgs length (vertical) at time $m_H t = 2$ is plotted for a slice through the blob, as function of the x and z coordinates (a vertical slice). Right the winding number density at time $m_H t = 2$ is plotted for the same slice through the blob.

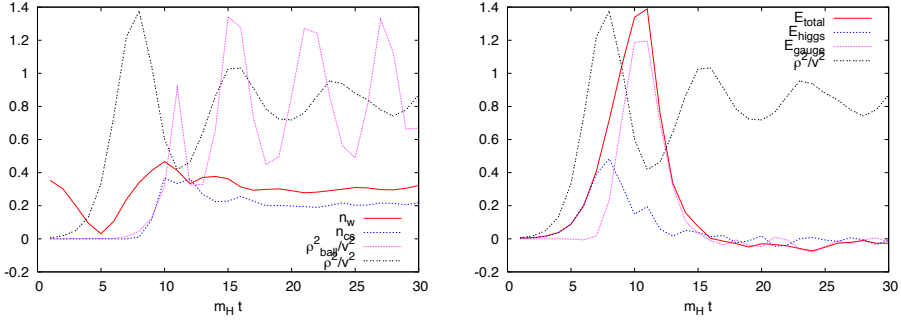


Figure 3.14: Left: N_w^{ball} , $N_{\text{CS}}^{\text{ball}}$ and $\overline{\rho^2}^{\text{ball}}$, for a ball with a radius of 6 lattice units ($2.1 m_{\text{H}}^{-1}$) around the center of the blob. Right: excess energy, $[\int_{\text{ball}} d^3x (\epsilon - \bar{\epsilon})]/E_{\text{sph}}$, in the same ball and its contributions from the Higgs field and the gauge fields.

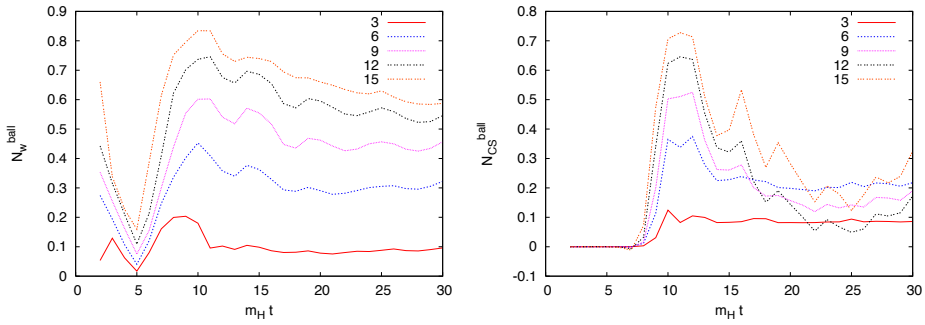


Figure 3.15: N_w^{ball} (left) and $N_{\text{CS}}^{\text{ball}}$ (right) for balls with varying radii, increasing from 3 lattice distances up to 15 lattice distances.

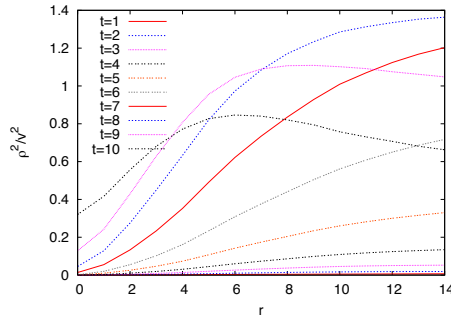


Figure 3.16: Profiles of the normalized Higgs length $\rho^2(r)/v^2$ for times $m_{\text{H}}t = 1$ to $m_{\text{H}}t = 10$. On the horizontal axis is the distance from the center, r , in lattice units ($0.35 m_{\text{H}}^{-1}$).

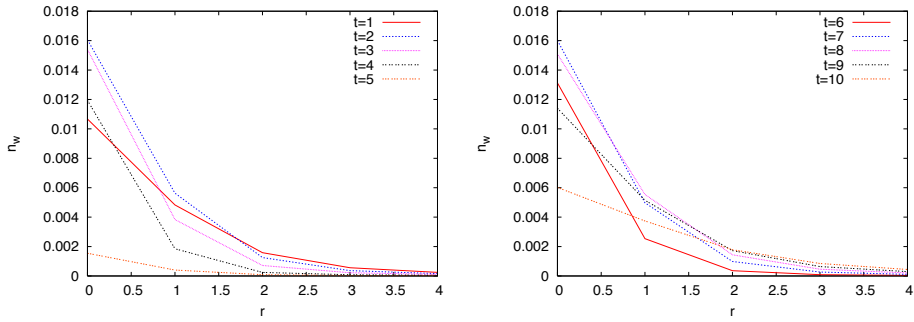


Figure 3.17: As in figure 3.16 for $n_w(r)$ for times $m_{\text{H}}t = 1$ to $m_{\text{H}}t = 5$ (left) and until $m_{\text{H}}t = 10$ (right).

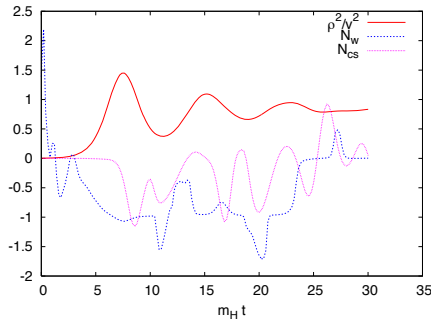


Figure 3.18: The analog of figure 3.4 for the trajectory with a late transition, $\overline{\rho^2}/v^2$, total winding number N_w and total Chern-Simons number N_{CS} .

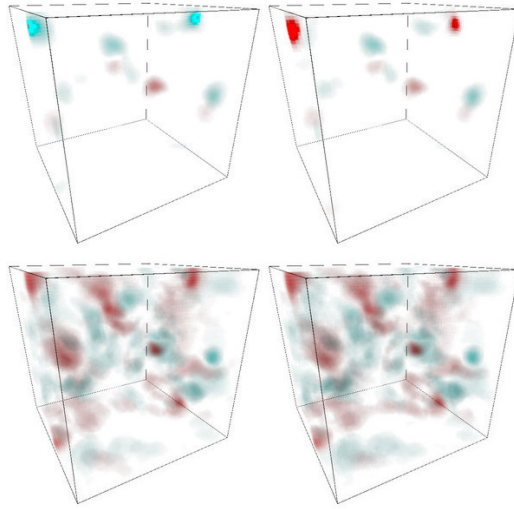


Figure 3.19: 3D plot for the winding number density (upper two figures) and Chern-Simons number density (lower two figures) at times $m_{\text{H}t} = 23$ (left) and $m_{\text{H}t} = 24$ (right).

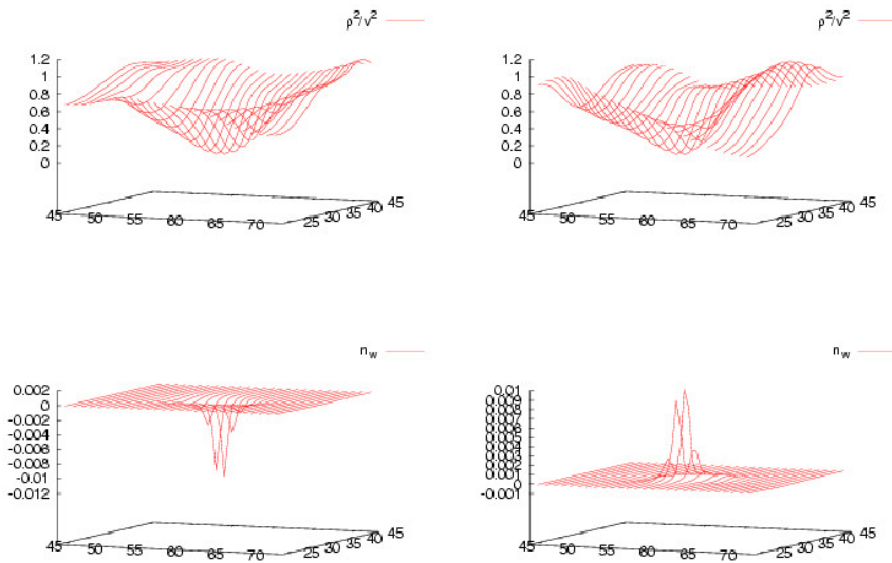


Figure 3.20: Upper plots: Higgs length as function of the x and z coordinates through the blob. Left is at time $m_{\text{H}t} = 23$, right at time $m_{\text{H}t} = 24$. Lower plots: the corresponding winding number density.

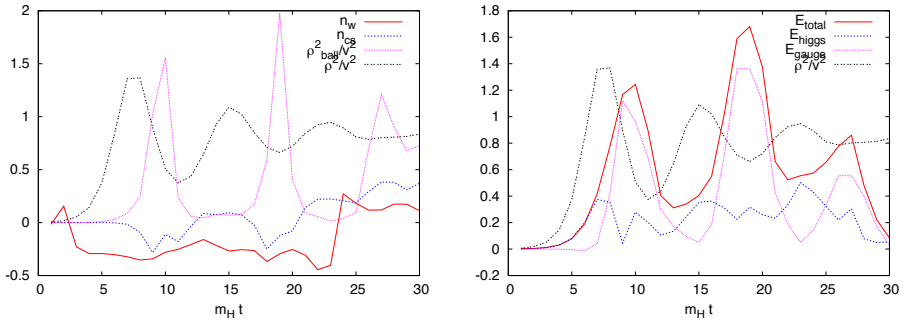


Figure 3.21: The analogue of figure 3.14: Left: N_w^{ball} , $N_{\text{CS}}^{\text{ball}}$ and $\overline{\rho^2}^{\text{ball}}$, for a ball with a radius of 6 lattice units ($2.1 m_H^{-1}$) around the center of the blob. Right: excess energy, $[\int_{\text{ball}} d^3x (\epsilon - \bar{\epsilon})]/E_{\text{sph}}$, in the same ball and its contributions from the Higgs field and the gauge fields.

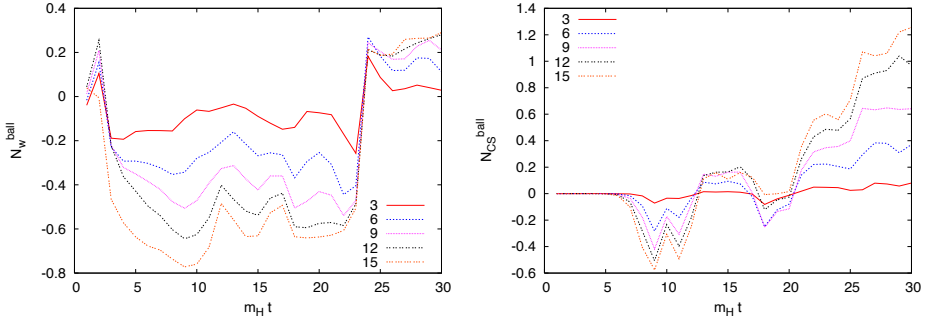


Figure 3.22: The analog of figure 3.15: N_w^{ball} (left) and $N_{\text{CS}}^{\text{ball}}$ (right) for balls with varying radii, increasing from 3 to 15 lattice units.

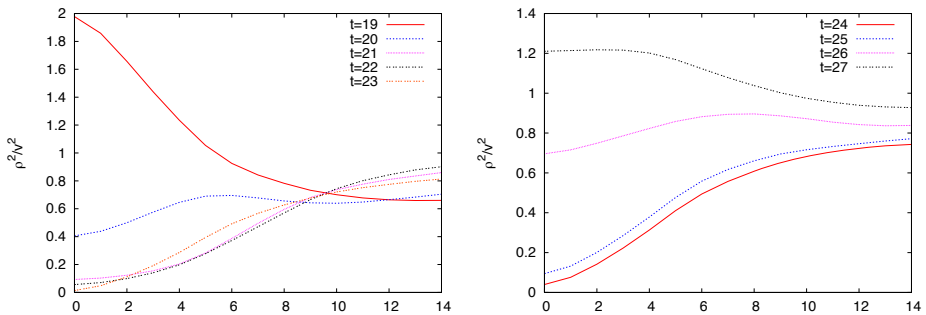


Figure 3.23: Profiles of the normalized Higgs length $\rho^2(r)/v^2$ for times $m_H t = 19$ to $m_H t = 23$ (left) and to $m_H t = 27$ (right). On the horizontal axis is the distance from the center r in lattice units ($0.35 m_H^{-1}$).

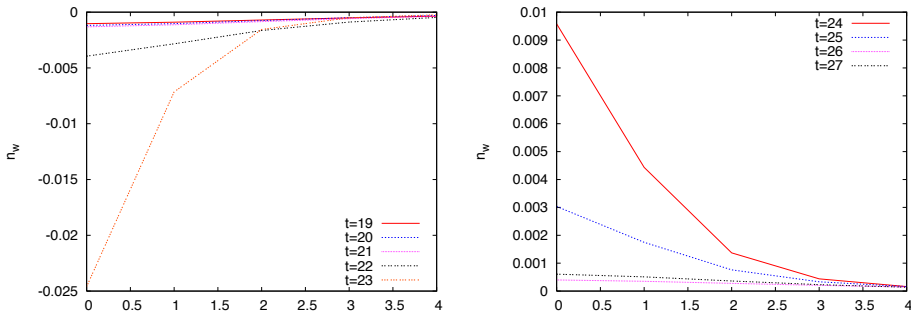


Figure 3.24: As in figure 3.23 for $n_w(r)$.

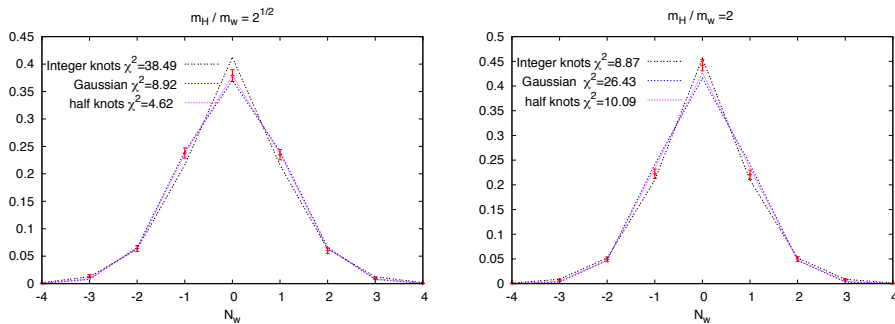


Figure 3.25: Normalized distribution of winding numbers at $m_H = 30$ for $m_H = \sqrt{2} m_W$ and $m_H = 2 m_W$. The fitted distributions are based on equations (3.43) and (3.44) (integer knots), (3.45) (Gaussian) and (3.47) (half-knots).

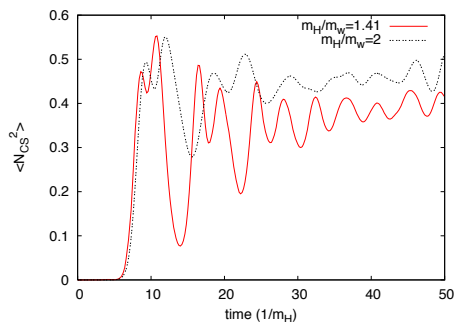


Figure 3.26: Chern-Simons susceptibility $\langle N_{CS}^2(t) \rangle$ for $m_H = \sqrt{2} m_W$ and $m_H = 2 m_W$.

CHAPTER 4

CP VIOLATION

4.1 INTRODUCTION

In the previous chapter the baryon production mechanism in CEB was studied in detail. Another essential ingredient for baryogenesis is *CP* violation, which is the subject of this chapter. The goal is to estimate the size of *CP* violation from the CKM matrix in CEB.

In conventional electroweak baryogenesis models baryon production takes place at the temperature of the electroweak phase transition ($T_{\text{EW}} \sim 10^2$ GeV). Using this temperature in the estimate (1.20) one finds that the size of *CP* violation is much too small to account for the baryon asymmetry of the universe. However, CEB takes place at (initially) zero temperature and it is not clear how to interpret equation (1.20) for this model (see also [80]).

In this chapter we consider the *CP* violating imprint from the CKM matrix on the boson fields of the Standard Model by integrating out the quarks. The resulting effective action can be expanded in various ways: in a heat kernel expansion (see [93] for a recent related approach), a derivative expansion [80], or an expansion in fields [46, 47]. We use an expansion in fields and determine at which order the first *CP* violating term occurs. Furthermore we apply this to CEB, and compare with the derivative expansion.

4.2 CP VIOLATION IN EXPANSION IN FIELDS

Consider the Lagrangian density of the Standard Model (2.1), and integrate out the quarks to obtain the effective action S_{eff} :

$$e^{iS_{\text{eff}}} = \int \mathcal{D}\bar{q}\mathcal{D}q e^{i \int d^4x \mathcal{L}_{SM}}, \quad (4.1)$$

In this section we will consider the expansion of S_{eff} in the fields W^\pm and φ_d , and analyze the CP violating contributions in this expansion. We work in the unitarity gauge as described in section 2.2, and do not consider the Z^0 , A and G^k fields (but see the comment at the end of section 4.2.2).

4.2.1 EXPANSION IN FIELDS

The expansion of the effective action S_{eff} in W^\pm and φ_d in momentum space is

$$\begin{aligned} & \frac{1}{n!n!(2m)!} \sum_{n,m} \int \left(\prod_{i=1}^{2n} \frac{d^4k_i}{(2\pi)^4} \right) \left(\prod_{j=1}^{2m} \frac{d^4q_j}{(2\pi)^4} \right) (2\pi)^4 \delta^4 \left(\sum_{i=1}^{2n} k_i + \sum_{j=1}^{2m} q_j \right) \\ & W_{\mu_1}^+(k_1) W_{\mu_2}^-(k_2) W_{\mu_3}^+(k_3) \cdots W_{\mu_{2n}}^-(k_{2n}) \varphi_d(q_1) \cdots \varphi_d(q_{2m}) \\ & \Gamma_{n,m}^{\mu_1 \cdots \mu_{2n}}(k_1, \dots, k_{2n}; q_1, \dots, q_{2m}), \quad (4.2) \end{aligned}$$

where the effective vertex functions are

$$\begin{aligned} & (2\pi)^4 \delta^4 \left(\sum_{i=1}^{2n} k_i + \sum_{j=1}^{2m} q_j \right) \Gamma_{n,m}^{\mu_1 \cdots \mu_{2n}}(k_1, \dots, k_{2n}; q_1, \dots, q_{2m}) = \\ & \frac{\delta^{2n+2m} S_{\text{eff}}}{\delta W_{\mu_1}^+(k_1) \cdots \delta W_{\mu_{2n}}^-(k_{2n}) \delta \varphi_d(q_1) \cdots \delta \varphi_d(q_{2m})}. \quad (4.3) \end{aligned}$$

As will become clear below, there must be an equal number of W^+ and W^- fields, and also the Higgs fields φ_d must come in even numbers. Because the gauge is fixed, the individual terms in the expansion are not gauge invariant. However, the full effective action is gauge invariant.

1PI DIAGRAMS

The effective vertex functions Γ can be represented by sums of 1PI diagrams that consist of a quark loop with bosonic external lines. Diagrams with more loops would require

internal boson lines, and do not occur because the bosons are not integrated out. Consider the contributions

(4.4)

where the diagram on the right-hand side is only different from the one on the left-hand side by the reversed fermion arrow (and the corresponding sign change of p). The curved dashed lines indicate more external lines that have not been drawn. There are other diagrams (with different orderings of the external lines) that contribute, but we will not consider these.

Using the interactions (2.33) and (2.36), the diagram on the left-hand side of (4.4) translates to

$$\begin{aligned}
 & - \int \frac{d^4 p}{(2\pi)^4} \text{Tr} \left(\tilde{\tau}^+ \gamma^{\mu_1} P_L \frac{(\not{p} - \not{k}_1)}{(p - k_1)^2} D \frac{(\not{p} - \not{k}_1 - \not{q}_1)}{(p - k_1 - q_1)^2} D \times \right. \\
 & \qquad \qquad \qquad \left. \frac{(\not{p} - \not{k}_1 - \not{q}_1 - \not{q}_2)}{(p - k_1 - q_1 - q_2)^2} \tilde{\tau}^- \gamma^{\mu_2} P_L \dots \right) \quad (4.5)
 \end{aligned}$$

where the trace is over the Dirac-indices, group indices and generation indices. The trace over $SU(3)$ indices is trivial and gives a factor three. The trace over the Dirac indices and the trace over isogeneration indices can be taken apart, such that equation (4.5) becomes

$$-3 \int \frac{d^4 p}{(2\pi)^4} \Delta_{n, \{m_1, \dots, m_{2n}\}}^{\mu_1 \dots \mu_{2n}} (P_L) M_{n, \{m_1, \dots, m_{2n}\}}, \quad (4.6)$$

with $m_1 = 1$ for this particular case, and where we have defined

$$\begin{aligned}
 \Delta_{n, \{1, \dots, m_{2n}\}}^{\mu_1 \dots \mu_{2n}} (X) = \\
 \text{Tr}_D \left(\gamma^{\mu_1} X \frac{(\not{p} - \not{k}_1)}{(p - k_1)^2} \frac{(\not{p} - \not{k}_1 - \not{q}_1)}{(p - k_1 - q_1)^2} \frac{(\not{p} - \not{k}_1 - \not{q}_1 - \not{q}_2)}{(p - k_1 - q_1 - q_2)^2} \gamma^{\mu_2} \dots \right) \quad (4.7)
 \end{aligned}$$

$$M_{n, \{m_1, \dots, m_{2n}\}} = \text{Tr}_{\text{ig}} (\tilde{\tau}^+ \mathcal{D} \tilde{\tau}^- \dots), \quad (4.8)$$

where Tr_D stands for the trace over Dirac indices, X is a matrix with Dirac indices, Tr_{ig} is the trace over isogeneration space indices, and $\mathcal{D} = D^2$. The dependence of Δ on the external momenta is suppressed. The subscript $n, \{m_1, \dots, m_{2n}\}$ denotes that there are $2n$ W^\pm lines and that there are m_i pairs of Higgs lines at each position in between the W^\pm lines. The m_i must add up to m .

At this point it is clear that the fields must come in pairs. If there is an odd number of Higgs interactions in between two W^\pm interactions, the Dirac trace in equation (4.5) vanishes because of the chiral projectors. Furthermore the isogeneration trace M vanishes if there is an odd number of W^\pm lines, and also if the W^+ fields do not alternate with the W^- fields.

Similar as equation (4.5) for the left-hand diagram of (4.4), one obtains for the the right-hand diagram

$$- \int \frac{d^4 p}{(2\pi)^4} \text{Tr} \left(\dots \tilde{\tau}^- \gamma^{\mu_2} P_L \frac{(\not{p} - \not{k}_1 - \not{q}_1 - \not{q}_2)}{(p - k_1 - q_1 - q_2)^2} D \frac{(\not{p} - \not{k}_1 - \not{q}_1)}{(p - k_1 - q_1)^2} D \times \right. \\ \left. \frac{(\not{p} - \not{k}_1)}{(p - k_1)^2} \tilde{\tau}^+ \gamma^{\mu_1} P_L \right), \quad (4.9)$$

(where we have taken $p \rightarrow -p$ with respect to (4.5)). By taking the transpose of the matrix inside the trace, using some of the relations for γ -matrices in Appendix A and the relation $\tilde{\tau}^{+T} = \tilde{\tau}^{-*}$, this can be rewritten to

$$-3 \int \frac{d^4 p}{(2\pi)^4} \Delta_{n, \{m_1, \dots, m_{2n}\}}^{\mu_1 \dots \mu_{2n}} (P_R) \bar{M}_{n, \{m_1, \dots, m_{2n}\}}^*, \quad (4.10)$$

where \bar{M} is obtained from M by interchanging $\tilde{\tau}^+ \leftrightarrow \tilde{\tau}^-$:

$$\bar{M}_{n, \{m_1, \dots, m_{2n}\}} = \text{Tr}_{\text{ig}} (\tilde{\tau}^- D^{m_1} \tilde{\tau}^+ \dots). \quad (4.11)$$

CP VIOLATING CONTRIBUTION

The interactions of the Standard Model are nearly invariant under CP transformation: the only change is that the CKM matrix V is complex conjugated (see section 2.3). For the diagrams (4.4) this implies that under CP transformation only the isogeneration traces M and \bar{M} in equations (4.6) and (4.10) are complex conjugated. The CP violating contribution is therefore the difference between the results (4.6) plus (4.10) and these same results with complex conjugated M and \bar{M} :

$$-3 \int \frac{d^4 p}{(2\pi)^4} \left\{ \Delta(P_L) (M - M^*) + \Delta(P_R) (\bar{M}^* - \bar{M}) \right\} = \\ -6i \int \frac{d^4 p}{(2\pi)^4} \left\{ \Delta\left(\frac{1}{2}\right) (\text{Im}M - \text{Im}\bar{M}) - \Delta\left(\frac{\gamma_5}{2}\right) (\text{Im}M + \text{Im}\bar{M}) \right\}, \quad (4.12)$$

where we have suppressed the indices of Δ and M .

This is the CP violating contribution of the effective vertices Γ . For the full effective action (4.2) one expects that CP violating terms contain an epsilon tensor $\epsilon^{\mu_1 \mu_2 \mu_3 \mu_4}$, which can only come from the trace $\Delta(\gamma_5/2)$. Therefore we consider in the following only this term.

4.2.2 CP VIOLATION

As expected, the CP violating contribution (4.12) is only nonzero if the imaginary part of V is nonzero. However for simple diagrams, the traces M and \bar{M} turn out to be real even if V is complex. In this section we derive the lowest order diagrams for which the CP violating contribution does not vanish, by starting with diagrams without W^\pm lines, and subsequently adding W^\pm lines.

Less than four W^\pm lines. If there are no W^\pm lines, the isogeneration space matrix contains only powers of \mathcal{D} and therefore M is real.

For two external W^\pm lines the $\tilde{\tau}^+$ and $\tilde{\tau}^-$ matrices bring in complex numbers. However the trace M is always real, as we show here. The most general M with two external W^\pm lines is

$$M_{1,\{m_1,m_2\}} = \text{Tr}(\tilde{\tau}^+ \mathcal{D}^{m_1} \tilde{\tau}^- \mathcal{D}^{m_2}). \quad (4.13)$$

The complex conjugate can be obtained by taking the hermitian conjugate of the matrix inside the trace

$$M_{1,\{m_1,m_2\}}^* = \text{Tr}(\mathcal{D}^{m_2} \tilde{\tau}^+ \mathcal{D}^{m_1} \tilde{\tau}^-), \quad (4.14)$$

where the relation $\tilde{\tau}^{+\dagger} = \tilde{\tau}^-$ is used. Using the cyclic property of traces, one sees that $M_{1,\{m_1,m_2\}}^* = M_{1,\{m_1,m_2\}}$.

Four W^\pm lines. For four W^\pm lines the most general M is

$$M_{2,\{m_1,m_2,m_3,m_4\}} = \text{Tr}(\tilde{\tau}^+ \mathcal{D}^{m_1} \tilde{\tau}^- \mathcal{D}^{m_2} \tilde{\tau}^+ \mathcal{D}^{m_3} \tilde{\tau}^- \mathcal{D}^{m_4}). \quad (4.15)$$

If three of the four m_i are equal to 1, this M is real which can be seen in a similar way as above. If two consecutive m_i are equal to 2, and the other two m_i are equal to 1, M is complex. However in this case the corresponding \bar{M} is equal to M^* , and therefore $\text{Im}\bar{M} = -\text{Im}M$ and the sum $(\text{Im}M + \text{Im}\bar{M})$ in the term with $\Delta(\gamma_5/2)$ in (4.12) vanishes.

One finds the first CP violating contribution to the effective action for $m_1 = 3, m_2 = 2, m_3 = m_4 = 1$. It can be checked (for example by using Mathematica) that for this case

$$\text{Im}M_{2,\{3,2,1,1\}} = -\frac{e^4}{4 \sin^4 \theta_W} J(\lambda_b^2 + \lambda_s^2 + \lambda_d^2) \delta\lambda^{12}, \quad (4.16)$$

$$\text{Im}\bar{M}_{2,\{3,2,1,1\}} = \frac{e^4}{4 \sin^4 \theta_W} J(\lambda_t^2 + \lambda_c^2 + \lambda_u^2) \delta\lambda^{12}, \quad (4.17)$$

where J is the Jarlskog invariant (1.21), and we have used the notations

$$\mathcal{D} = \text{diag}(\lambda_u^2, \lambda_c^2, \lambda_t^2, \lambda_d^2, \lambda_s^2, \lambda_b^2), \quad (4.18)$$

$$\delta\lambda^{12} = (\lambda_t^2 - \lambda_c^2)(\lambda_t^2 - \lambda_u^2)(\lambda_c^2 - \lambda_u^2)(\lambda_b^2 - \lambda_s^2)(\lambda_b^2 - \lambda_d^2)(\lambda_s^2 - \lambda_d^2), \quad (4.19)$$

where diag denotes a diagonal matrix in isogeneration space. The CP violating contribution (the term with $\Delta(\gamma_5/2)$ from equation (4.12)) from this diagram is then

$$\frac{3ie^4}{2\sin^4\theta_W} J\delta\lambda^{12}(\lambda_t^2 + \lambda_c^2 + \lambda_u^2 - \lambda_b^2 - \lambda_s^2 - \lambda_d^2) \int \frac{d^4p}{(2\pi)^4} \Delta_{2,\{3,2,1,1\}}\left(\frac{\gamma_5}{2}\right), \quad (4.20)$$

where the result of the integral is a function of the external momenta k_i and q_j . Note the resemblance with the standard estimate (1.20).

There are also CP violating contributions from diagrams with permutations of the m_i , e.g. $m_1 = 2, m_2 = 3, m_3 = m_4 = 1$. The contribution from this permutation is

$$-\frac{3ie^4}{2\sin^4\theta_W} J\delta\lambda^{12}(\lambda_t^2 + \lambda_c^2 + \lambda_u^2 - \lambda_b^2 - \lambda_s^2 - \lambda_d^2) \int \frac{d^4p}{(2\pi)^4} \Delta_{2,(2,3,1,1)}\left(\frac{\gamma_5}{2}\right). \quad (4.21)$$

This term is not expected to cancel (4.20), because the Δ 's are different functions of the external momenta.

Comments. These diagrams with four W^\pm lines and fourteen Higgs lines are the lowest order CP violating diagrams. Diagrams with more W^\pm lines need also more Higgs lines. E.g. diagrams with six W^\pm lines must have at least nine pairs of Higgs lines (so eighteen Higgs lines). These diagrams are therefore of higher order in both the W^\pm fields and in the Higgs field.

Interactions with other gauge bosons (Z , A and G^k) lead to insertions in the isogeneration trace M of matrices that are diagonal in $SU(2)$ space and proportional to the identity matrix in generation space. Clearly these interactions are not interesting from the point of view of CP violation.

4.2.3 VALIDITY OF EXPANSION IN FIELDS

Next we examine when the expansion in fields (4.2) can be expected to be valid.

An extra W^\pm line introduces an extra factor

$$\frac{e}{\sqrt{2}\sin\theta_W} \frac{W^\pm \not{p}}{p^2}, \quad (4.22)$$

as follows from the interaction term (2.36). Here p is the loop momentum, which is the sum of the original loop momentum and the external momentum k_i through the extra W^\pm line. Because $(e/\sqrt{2}\sin\theta_W) \approx 0.45$, this factor is typically smaller than one for momenta $k_i \gtrsim W^\pm$, and one expects that for such momenta, higher order terms become smaller and the expansion is valid.

Similarly an extra Higgs line introduces an extra factor

$$D \frac{\varphi_d \not{p}}{p^2}, \quad (4.23)$$

as follows from the interaction (2.33). Here D is the diagonal matrix (2.33) containing Yukawa couplings λ_i that vary in size from 10^{-5} up to 1. In general one expects that they will occur in products that are smaller than one. For example we have seen above that the CP violating terms are proportional to

$$(\lambda_t^2 \lambda_b^2 \lambda_c \lambda_s)^2 \ll 1. \quad (4.24)$$

So also in this case one expects that the expansion is valid for momenta larger than the fields $q_j \gtrsim \varphi_d$, where q_j is the external momentum through the extra Higgs line.

In the previous section we have seen that the lowest order CP violating terms are of rather high order in the fields. This means that, if the expansion is valid, the CP violating contributions are automatically very small.

4.3 CP VIOLATION IN CEB

In this section we estimate the size of CP violation from the CKM matrix in CEB. We argue by estimating the typical sizes of the external momenta and the fields that the expansion is expected to be valid in CEB. As a consequence CP violation from the CKM matrix in CEB is expected to be small.

Consider first the momenta. From the equation of motion (3.33) one sees that they are set by the scale μ_{eff} , even if the field Φ is small. In the instantaneous quench that is used in chapter 3, $\mu_{\text{eff}} = \pm\sqrt{\lambda}v$ (equation (3.34)), where the sign is positive before the quench and negative after the quench (we used $\lambda = 1/9$ for the case $m_H/m_W = \sqrt{2}$ and $\lambda = 2/9$ for the case $m_H/m_W = 2$). In slower quenches (see [63]), the change of μ_{eff} is gradual but eventually it will reach the same value.

We can also check from the simulations that the momenta are at scale v . For example in figure 3.23, the largest length scale is of the order of 20 lattice units, which corresponds with a smallest momentum of around $0.4v$.

Next consider the fields. The Higgs and gauge fields start close to zero at the onset of the transition, but grow quickly towards the new vacuum value $v/\sqrt{2}$ (from the simulations we know that the gauge fields grow soon after the Higgs field becomes large). In some regions the Higgs field remains small or becomes small again later, for example in the half-knot configurations that we studied in chapter 3. These configurations are important for the baryon number violation.

From these estimates we expect that in CEB the ‘expansion parameters’ (4.22) and (4.23) are smaller than one and that the expansion is valid. This is especially so in the half-knot configurations where φ_d is even smaller. Therefore we expect that CP violation from CKM matrix in CEB is small.

4.4 COMPARISON WITH DERIVATIVE INTERACTION

It is interesting to compare with the derivative expansion of the effective action. This expansion can be obtained by expanding S_{eff} in derivatives of fields ($D_\mu\varphi_d$ and $F_{\mu\nu}$, around $D_\mu\varphi_d = F_{\mu\nu} = 0$). This expansion is quite different from the expansion in fields of above, because the latter is not valid for vanishing momentum (so for $D_\mu\varphi_d = F_{\mu\nu} = 0$).

In [80] the derivative expansion of S_{eff} is studied by making use of the general formalism for derivative expansions for chiral gauge theories derived in [94, 95]. The expansion of [80] is actually an expansion in the number of indices μ . No CP violation is found up to fourth order, but it is anticipated to come in at sixth order. The structure of the coefficients at fourth order suggests that the CP violating term at sixth order will not be suppressed by the factor $\delta\lambda^{12}$, and is therefore potentially important.

To determine when this expansion is valid one can again check when terms of higher order become smaller. $D_\mu\varphi_d$ and $F_{\mu\nu}$ have dimensions of momentum squared. Therefore higher order terms need to have higher powers of a dimensionful quantity in the denominator. The only dimensionful quantity that is available is $D\varphi_d$, where D is the matrix of Yukawa couplings. Therefore the expansion parameter is roughly $p/D\varphi_d$, the inverse of equation (4.23) of the expansion in fields. As a consequence we expect that the derivative expansion will not be valid for CEB.

4.5 DISCUSSION

In this chapter we have studied CP violation from the CKM matrix and applied the results to estimate the CP violating effect in CEB. In an expansion in fields of the bosonic effective action of the Standard Model, CP violating contributions start at fourth order in the gauge fields and fourteenth order in the Higgs fields. We expect that in CEB this expansion is valid, and that therefore the CP violating effect is small (of the order of the standard estimate (1.20)).

We have used equilibrium quantum field theory in this chapter, even though CEB is clearly not in equilibrium and a correct description requires non-equilibrium quantum field the-

ory (see also part II). However we do not expect that the CP violating effect in non-equilibrium field theory will be much larger.

Intuitively one can explain the smallness of the CP violation for large momenta as follows. The CP violation depends on mass differences of quarks. When the dynamics is at momentum scales that are much larger than the mass differences, these differences become relatively small, and so does the CP violation. In case that the momenta are of the order of the mass differences (or smaller), the CP violating effect can be much larger. For example this occurs in $K\bar{K}$ and $B\bar{B}$ oscillations where CP violation is observably large. This is also in agreement with the expected coefficients of the first CP violating terms (of sixth order) in the derivative expansion, which are probably not suppressed by $\delta\lambda^{12}$.

The problem with constructing a model of electroweak baryogenesis with CP violation from the CKM matrix seems to be that these models typically have two mismatching scales: the baryon violation occurs at electroweak scales, and the CP violation is only substantial at lower energy scales. To construct a working model one can try to resolve this mismatch (see however [96] for an attempt along another way). An example is presented in [97, 98, 99], where it is suggested that quarks with small momenta (at the low end of a thermal distribution) can generate a large CP violating effect. However this model turns out to be not viable [77, 100, 78].

CHAPTER 5

CONCLUSIONS

In this part we studied Cold Electroweak Baryogenesis, which is a model that combines low scale inflation and electroweak baryogenesis. This model of electroweak baryogenesis is quite different from electroweak baryogenesis models studied before, because it takes place during a tachyonic transition at zero temperature instead of during the electroweak phase transition at finite temperature. In previous work [58, 61] it has been confirmed, using numerical simulations in the $SU(2)$ Higgs model, that this model can work: there is indeed baryon production, and if there is CP violation an asymmetry can be produced. Here this work is extended in two directions: the mechanism of baryon production in CEB is studied in detail, and the amount of CP violation from the CKM matrix is estimated.

In chapter 3 we studied the mechanism of baryon production in detail. The baryon number is related to the Chern-Simons number N_{CS} via the anomaly equation (2.70) of the gauge fields, which is in turn closely related to the Higgs winding number N_w . To obtain more insight in the evolution of these numbers, we studied their densities n_{CS} and n_w .

It has been suggested [56] that the Chern-Simons number is changed by decaying Higgs winding configurations, that are created by the Kibble mechanism. We find a slightly different picture: there are no clear-cut Higgs winding configurations, because there is no mechanism that can concentrate an integer winding number in a limited region in space (as there is energy minimization for stable winding configurations like monopoles). But there are regions where the Higgs length is small. These ‘half-knots’ have a large winding number density n_w and a total winding number of approximately $1/2$. The winding number in the total volume is still integer; the other half is spread out over this volume. When the Higgs length in the center of a half-knot vanishes, the sign of its winding number can change. The total winding number N_w then changes by an integer. When the system re-

laxes to its vacuum, the Chern-Simons number N_{CS} adjusts to the Higgs winding number N_{w} and a baryon has been produced.

These half-knots can occur in the initial conditions by statistical fluctuations, in which case we call them ‘early half-knots’. We found that they can also be formed later on. These ‘late half-knots’ seem to occur in regions where the Higgs length oscillates about its new vacuum quite strongly, often not in phase with the overall oscillation of the Higgs length, and with very little damping. These regions are reminiscent of oscillons. Because interactions are necessary for creating a CP asymmetry, we expect that only the late half-knots are important for baryogenesis.

In chapter 4 we estimated the size of CP violating effect from the CKM matrix in CEB. We did this by analyzing the effective action that is obtained by integrating out the fermions of the Standard Model. In the expansion in fields of this effective action, the first CP violating term comes in at fourth order in the gauge fields W^\pm and at fourteenth order in the Higgs field φ_d , in a way that is similar to the estimate (1.20). The expansion is valid for large momenta compared to the fermion ‘masses’ $\lambda_i\varphi_d$. When the expansion is valid, the CP violating term is automatically very small because it is proportional to high powers of the expansion parameters.

An alternative expansion is the derivative expansion, that is valid for small momenta compared to the fermion masses. As explained in [80], it is likely that the coefficients of the CP violating terms are not suppressed by the factor (1.20) as is the case in the expansion in fields.

For the case of CEB we argue that the momenta are larger than the fermion masses, and consequently that the expansion in fields is expected to be valid and the CP violating effect to be small. In models of baryogenesis that use the electroweak anomaly for baryon number violation, the energy scale of baryon violation is the electroweak scale, while the CP violation from the CKM matrix is typically only significant at lower energy scales.

We conclude that CEB is an interesting alternative to more conventional baryogenesis models. The mechanism of baryon production is quite different and may involve oscillons. However we expect that CEB shares the problem of too little CP violation from the CKM matrix with conventional electroweak baryogenesis models. To resolve this the model has to be adjusted, for example by somehow matching the energy scales of baryon violation and CP violation, or by adding an extra source of CP violation.

Part II

Quantum cosmological correlations

CHAPTER 6

INTRODUCTION

Looking up at the sky at night, one sees that the matter in the universe is not at all homogeneously distributed: inside the stars the matter density is huge, but outside the stars there is hardly any matter at all. Yet there is evidence that in the early universe the matter distribution was quite homogeneous. For example the temperature that is observed in the Cosmic Microwave Background (CMB) radiation is the same in all directions, up to small inhomogeneities of the order of 10^{-5} . These small inhomogeneities are the seeds of the large inhomogeneities that we observe nowadays. They grow under the influence of gravity.

One of the attractive features of inflation is that it provides an explanation for the origin of these small fluctuations: quantum fluctuations during inflation are amplified and can become observable. Different inflation models lead to different statistical properties of the fluctuations, which are characterized by correlation functions. For the simplest inflation models the spectrum is close to Gaussian (there is only a nontrivial two point function), but in more complicated models there can also be non-Gaussian features. Hence observations of correlation functions of the temperature fluctuations in the CMB can teach us lessons about inflation.

These observations have become much more precise in the past fifteen years. The first detection of the temperature fluctuations has been done with the COBE satellite in 1992. Since then there have been many more experiments, among which the WMAP satellite, that observed the temperature fluctuations with increasing precision. In the future the precision will become even better with the Planck satellite [101].

Theoretical calculations of the quantum fluctuations are often done using free field theory, which gives a good approximation because the interactions during inflation are typically small (in agreement with the absence of observations of non-Gaussian features). But

	$a(t)$	$H(t)$
cosmological constant ($w = -1$)	e^{Ht}	t^0
radiation ($w = 1/3$)	$t^{1/2}$	t^{-1}
matter ($w = 0$)	$t^{2/3}$	t^{-1}

Table 6.1: Time dependence of the scale factor a and the Hubble rate H for some important stages in the evolution of the universe.

because of the improving precision of the observations, also theoretical calculations are currently being done at higher orders [102, 103, 104, 105, 106, 107, 108]. One can distinguish two effects from interacting fluctuations: backreaction on the classical background, which affects the Hubble rate H and the slow-roll parameters, and interactions between the fluctuations themselves. In calculations of the latter effect, one often uses classical physics to calculate the evolution of the fluctuations. In the next chapter, which has been published as [109], we check how good this approximation is.

This chapter is meant as introduction to and motivation for the next chapter. We shortly review some aspects of cosmological perturbation theory, and of existing calculations of inflationary fluctuations.

6.1 COSMOLOGICAL PERTURBATION THEORY

From the fact that the CMB is nearly homogeneous we know that it is sensible to approximate the (early) universe as a homogeneous universe. In chapter 1 we gave the evolution equations (1.4)-(1.6) for a homogeneous universe during inflation. Here we are interested in perturbations about the homogeneous solution, hence in cosmological perturbation theory (see [110] for a review).

6.1.1 SCALES

First we compare the evolution of the wavelengths of the perturbations with the evolution of the horizon length H^{-1} .

The wavelengths of the perturbations are stretched with the expansion of the universe and therefore grow with the scale factor a . The evolution of a depends on the (homogeneous) energy ρ and pressure P of the universe via the equation of state, which is assumed to be given by the ratio $w = P/\rho$. For some important cases the time dependence of a and H is given in table 6.1.

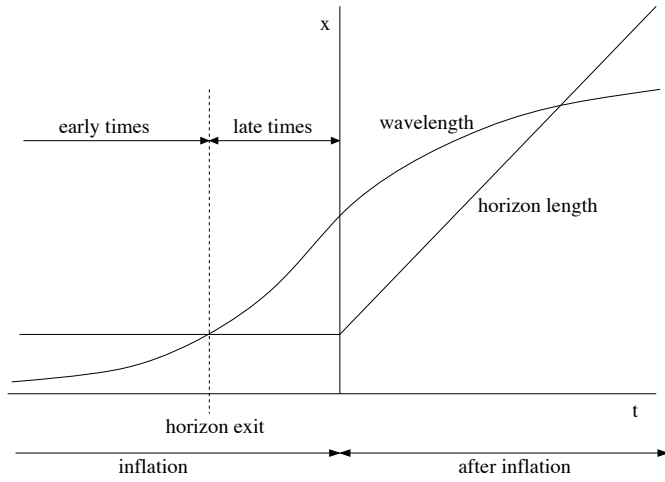


Figure 6.1: Sketch of the evolution of a wavelength of a perturbation, and of the horizon length H^{-1} .

During inflation the equation of state is close to $w = -1$. Therefore a grows (nearly) exponentially, and the horizon length H^{-1} is (nearly) constant. Hence the wavelengths grow faster than the horizon length; the modes are said to ‘leave the horizon’. The moment when the wavelength is equal to the horizon length is called the moment of horizon exit. For a mode with comoving momentum k this occurs when $k/aH = 1$. Modes with $k \ll aH$ are outside the horizon.

The fluctuations at the end of inflation are referred to as the primordial fluctuations. After inflation and reheating the universe is first radiation dominated and then matter dominated. In these periods the scale factor grows as $t^{1/2}$ and $t^{2/3}$ respectively, while the horizon length grows linearly in time. Hence the growth of the wavelengths is slower than that of the horizon length and the modes enter the horizon again. The large scale fluctuations that we observe now (e.g. in the CMB), are currently inside the horizon but have been outside the horizon before. The situation is sketched in figure 6.1.

6.1.2 DEGREES OF FREEDOM

Next we study which degrees of freedom can fluctuate and define the curvature perturbation which is the quantity in terms of which the primordial fluctuations are usually expressed.

First there are the matter fields. For cosmology one is interested in their influence on spacetime and therefore in their energy-momentum tensor $T_{\mu\nu}$. Its scalar perturbations

are

$$\delta\rho = -\delta T_0^0, \quad \delta P = \frac{1}{3}\delta T_i^i, \quad \partial_i\delta q = \delta T_i^0, \quad (6.1)$$

where we have neglected anisotropic stress.

Second there is the metric tensor $g_{\mu\nu}$ which has ten degrees of freedom: two tensor, four vector and four scalar degrees of freedom. Fluctuations in the tensor and scalar degrees of freedom are ‘amplified’ during inflation and are therefore interesting (see next section). The tensor fluctuations correspond to gravitational waves and can also have an imprint in the CMB. Their observation would be an important source of information. However they have not been observed yet and we will not consider them here. Vector fluctuations are not amplified and will also not be considered here. With only scalar perturbations, the metric can be written as

$$ds^2 = -(1 + 2A)dt^2 + 2a\partial_i B dx^i dt + a^2 [(1 - 2\psi)\delta_{ij} + 2\partial_{ij}E] dx^i dx^j. \quad (6.2)$$

This set of scalar energy-momentum perturbations (6.1) and metric perturbations (6.2) is not gauge invariant and also contains redundant degrees of freedom (gauge modes and modes that can be eliminated by constraint equations). Often one uses combinations of these perturbations that have certain advantages in certain gauge fixings.

The primordial fluctuations are usually expressed in a combination that corresponds to the curvature perturbation. Its definition depends on the coordinate system. Two common definitions are

$$-\zeta = \psi + \frac{H}{\dot{\rho}}\delta\rho, \quad \mathcal{R} = \psi - \frac{H}{\rho + P}\delta q, \quad (6.3)$$

which are respectively the curvature perturbation on uniform-density hypersurfaces and the comoving curvature perturbation. It can be shown that they differ by terms that are proportional to $k^2/(aH)^2$, which are small outside the horizon.

The curvature perturbation is often referred to as the adiabatic perturbation. There can also be isocurvature (or entropy) perturbations. The total entropy perturbation is (see e.g. [111])

$$S = H \left(\frac{\delta P}{\dot{P}} - \frac{\delta\rho}{\dot{\rho}} \right). \quad (6.4)$$

In linear approximation in the fields, the change in the curvature perturbation on scales outside the horizon (neglecting spatial derivatives) can be expressed as [111]

$$\dot{\mathcal{R}} \approx -3H \frac{\dot{P}}{\dot{\rho}} S. \quad (6.5)$$

Therefore the curvature perturbation remains constant outside the horizon if there are no isocurvature perturbations. This is for example the case if there is only one fluctuating degree of freedom (as in single field inflation, see below).

6.1.3 OBSERVATIONS

In the end we observe temperature fluctuations in the CMB. Hence to compare the calculated primordial fluctuations with observations, the evolution of the primordial fluctuations has to be calculated up to the time of photon decoupling and then they have to be transformed to temperature fluctuations. By following this procedure one has found that the primordial power spectrum of the curvature perturbation and its spectral index are given by equation (1.13). Hence the fluctuations are small and their spectrum is nearly flat.

Moreover we know (see e.g. [112, 113]) that the observations are consistent with primordial fluctuations that are purely adiabatic. A mix between adiabatic and entropy perturbations is also allowed, but pure entropy perturbations are ruled out.

As mentioned above, no signs of tensor modes have been found yet. Also no non-Gaussian corrections have been found yet. The constraints on these effects will be improved significantly in the future with the Planck satellite.

6.2 INFLATIONARY FLUCTUATIONS

The primordial fluctuations are the fluctuations at the end of inflation. As mentioned above, one usually considers only the fluctuations in the curvature perturbation. This section contains a short review of the theoretical calculation of the correlation functions of the curvature perturbation at the end of inflation.

6.2.1 QUANTUM FLUCTUATIONS IN DE SITTER SPACE

A de Sitter universe is a universe with a positive cosmological constant. An inflating universe is quasi de Sitter: the potential energy acts as a cosmological constant, but is not completely constant. In the limit that the slow-roll parameters vanish, it becomes exactly a de Sitter universe. We first consider quantum fluctuations in an exact de Sitter universe.

A de Sitter universe is a curved spacetime, and quantum fields on such spacetimes have peculiar properties [114]. The most famous example is a black hole. Hawking showed [115] that if one puts a quantum field in the background spacetime of a black hole, the black hole emits thermal radiation in this field: the Hawking radiation. In a de Sitter universe there is a similar effect.

For our purposes we are interested in correlation functions of a quantum field in de Sitter space as a function of time. Because the background is time dependent, the system is

not in equilibrium and one has to use non-equilibrium field theory. This is based on the Closed Time Path formalism, as described in section 7.2.1.

During inflation interactions are typically small and the correlation functions can be well approximated by free field theory. Of course the only nontrivial correlation function in this case is the two point function, from which one derives the power spectrum. Consider a free, massless and minimally coupled scalar field ϕ with action

$$S = -\frac{1}{2} \int d^4x \sqrt{-g} \partial_\mu \phi \partial^\mu \phi \quad (6.6)$$

on a de Sitter background. In terms of conformal time $\tau = -\int_t^\infty dt'/a(t')$ the metric is

$$ds^2 = a(\tau)^2 (-d\tau^2 + d\mathbf{x}^2), \quad (6.7)$$

with scale factor $a(\tau) = -1/H\tau$. The two point function of ϕ at equal times τ is called $F(k, \tau, \tau)$ (see equation (7.17)):

$$F(k, \tau, \tau) = \int d^3x e^{-i\mathbf{k}\cdot\mathbf{x}} \langle \phi(\tau, \mathbf{x}) \phi(\tau, 0) \rangle. \quad (6.8)$$

The total power of the field fluctuations is

$$\int \frac{d^3k}{(2\pi)^3} F(k, \tau, \tau) = \int \frac{dk}{k} \mathcal{P}(k, \tau), \quad \mathcal{P}(k, \tau) = \frac{k^3}{2\pi^2} F(k, \tau, \tau), \quad (6.9)$$

where $\mathcal{P}(k, \tau)$ is the power spectrum. Using the result (7.24) for $F(k, \tau, \tau)$ one finds for scales well outside the horizon ($|k\tau| \ll 1$) that the power spectrum is

$$\mathcal{P} = \frac{H^2}{4\pi^2}. \quad (6.10)$$

This power spectrum is independent of k and is therefore called a flat spectrum.

6.2.2 SINGLE FIELD INFLATION

In single field inflation the accelerated expansion is caused by the potential energy of one scalar field. This field is supposed to have a spatially homogeneous expectation value, which slowly rolls down from the potential. The scalar perturbation about the homogeneous background is quantized, and has fluctuations with a power spectrum as described above. In the context of inflation one often chooses a gauge (coordinate system) in which this scalar degree of freedom is the curvature perturbation. In this section we closely follow [116] to derive the action for the curvature perturbation at second order, and use equation (6.10) to obtain its power spectrum. We also repeat the argument in [116] for conservation of the curvature perturbation to all orders.

ACTION OF THE CURVATURE PERTURBATION

For the current purpose it is convenient to work in the ADM formalism [117], in which the metric is parameterized as

$$ds^2 = -N^2 dt^2 + h_{ij}(dx^i + N^i dt)(dx^j + N^j dt), \quad (6.11)$$

where N is the lapse function and N^i the shift function. Note that in this section we use coordinate time t instead of conformal time τ . The action (1.3) for single field inflation becomes

$$S = \frac{1}{2} \int \sqrt{h} \left[NR^{(3)} - 2NV + N^{-1}(E_{ij}E^{ij} - E^2) + N^{-1}(\dot{\sigma} - N^j \partial_j \sigma)^2 - Nh^{ij} \partial_i \sigma \partial_j \sigma \right], \quad (6.12)$$

where

$$E_{ij} = \frac{1}{2} (\dot{h}_{ij} - \nabla_i N_j - \nabla_j N_i), \quad E = E^i_i, \quad (6.13)$$

and where ∇_i is the covariant derivative calculated with the metric h_{ij} . The gauge in which the remaining scalar degree of freedom is the curvature perturbation, is

$$\delta\sigma = 0, \quad h_{ij} = a^2 e^{2\zeta} [\exp(\gamma)]_{ij}, \quad \partial_i \gamma_{ij} = 0, \quad \gamma_{ii} = 0, \quad (6.14)$$

where γ_{ij} is the tensor perturbation which we neglect in the remaining. Note that ζ is dimensionless. We follow here the notation of [116], but the ζ of equation (6.14) actually corresponds to the \mathcal{R} of equation (6.3).

N and N^i can be seen as Lagrange multipliers, i.e. their equations of motion

$$\nabla_i [N^{-1}(E^i_j - \delta^i_j E)] = 0, \quad (6.15)$$

$$R^{(3)} - 2V - N^{-2}(E_{ij}E^{ij} - E^2 + \dot{\sigma}^2) = 0, \quad (6.16)$$

are constraint equations. They can be solved perturbatively in terms of ζ and their solutions can be put back into the action, to obtain the action for ζ . It turns out [116] that it is sufficient to solve equations (6.15) and (6.16) to first order, in order to obtain the action to second order. The resulting action is

$$S = \frac{1}{2} \int d^4x \frac{\dot{\sigma}^2}{H^2} [a^3 \zeta'^2 - a(\partial\zeta)^2]. \quad (6.17)$$

For constant $\dot{\sigma}$ this is just the action (6.6) of a scalar field with a normalization factor $|\dot{\sigma}/H| = \sqrt{2\epsilon} M_{\text{pl}}$, where ϵ is the slow-roll parameter (1.7). In the limit $\epsilon \rightarrow 0$, the action of ζ vanishes and ζ is not well defined.

In general however $\dot{\sigma}$ and ϵ will not remain constant. At this point the advantage of using the curvature perturbation ζ comes in: because ζ is conserved outside the horizon (see below) it is sufficient to calculate ζ just after horizon exit, even if the background changes. The power spectrum of ζ can then easily be obtained by dividing equation (6.10) by $2\epsilon M_{\text{pl}}^2$ evaluated at the time just after horizon exit, and is:

$$\mathcal{P}_\zeta = \frac{1}{8\pi^2 M_{\text{pl}}^2} \frac{H^2}{\epsilon}. \quad (6.18)$$

Using the equation of motion (1.4) and the slow-roll approximation, this can be rewritten to equation (1.11).

To be able to calculate higher point correlation functions and loop corrections, one needs to solve the action of ζ to higher orders. In [116] the action is calculated up to third order, and the tree-level three point correlation function is obtained. It is found that this non-Gaussianity is too small to be observable.

ζ CONSERVATION

In single field inflation there are no isocurvature perturbations. Therefore the curvature perturbation is conserved outside the horizon in linear approximation, as was mentioned above. In fact it is shown in [116] and [118] that this conservation holds to all orders under the assumption that fluctuations with wavelengths of the horizon length or smaller can be neglected (the procedure of leaving out the short wavelength is called smoothing). Here we repeat the argument that is presented in [116].

Instead of solving the constraint equations (6.15) and (6.16) perturbatively in ζ as we did above, we solve them here perturbatively in derivatives. We write $N = 1 + \delta N + \dots$ where δN is of first order in derivatives but to all orders in fields, which is consistent with the structure of the constraint equations. N^i is of zeroth order in derivatives. To first order in derivatives we have

$$E_{ij}E^{ij} - E^2 = -6H^2 - 12H\dot{\zeta} + 4H\nabla_i N^i + \dots \quad (6.19)$$

Using this and the background equation of motion (1.4), the Hamiltonian constraint (6.16) becomes

$$-2V\delta N + 6H\dot{\zeta} - 2H\nabla_i N^i = 0, \quad (6.20)$$

where $R^{(3)}$ drops out because it is of second order in derivatives. Then the action up to first order in derivatives can be rewritten as

$$S = - \int d^4x a^3 e^{3\zeta} (1 + \delta N) 2V = - \int d^4x a^3 e^{3\zeta} (6H^2 - \dot{\sigma}^2 + 6H\dot{\zeta} - 2H\nabla_i N^i) = \int d^4x [2\partial_t (a^3 e^{3\zeta} H) + 2H\partial_i (a^3 e^{3\zeta} N^i)], \quad (6.21)$$

where we have used (6.16) and (6.20) and left out $R^{(3)}$. Both terms of (6.21) do not contribute to the classical equation of motion. All the remaining terms in the action have at least two derivatives.

The argument for ζ conservation is that if one neglects the spatial derivatives (smoothing), the classical equation of motion that is derived from this action always has a constant solution. This remains true even if the background parameters like H and ϵ are not constant. This is clearly a valid argument for contributions from tree level diagrams, but not necessarily for contributions from loop diagrams, since then internal lines can have large momenta.

6.2.3 MULTIFIELD INFLATION

There are many inflation models that involve more than one field. Examples are multifield models like assisted inflation [119] and N-flation [120], in which there are several fields that contribute to the accelerating expansion. Another possibility is that there is only one field that causes the accelerating expansion, but that there are other fields that cause the density fluctuations, as in the curvaton mechanism [121, 122, 123]. A motivation to study these inflation models is that often models of physics beyond the Standard Model involve many fields. Models with several fields can have advantages over single field inflation. For example they may need less fine-tuning, or they may not need the inflaton field displacement to be larger than M_{pl} as is often the case in single field inflation models.

In inflation models with more than one field the curvature perturbation is not conserved outside the horizon, because there are isocurvature perturbations. As a consequence the primordial fluctuations are much harder to calculate. The correlation functions cannot be calculated just after horizon exit, but their evolution up to the end of inflation has to be taken into account.

The existing methods to calculate the evolution of the correlation functions after horizon exit use classical physics. This is expected to give a good approximation, because the occupation numbers of the field modes after horizon exit grow quickly, which is usually an indication for classical behaviour (see also Appendix B). In the next chapter we will investigate this classical approximation for a toy model. Here we briefly review two classical methods to calculate the evolution of correlation functions: the stochastic approach and the δN formalism.

STOCHASTIC APPROACH

In the stochastic approach [124, 125] a field operator ϕ is split up in a ‘coarse grained’ part $\bar{\phi}$ that is considered to be classical, and a remaining part:

$$\phi(t, \mathbf{x}) = \bar{\phi}(t, \mathbf{x}) + \int \frac{d^3k}{(2\pi)^3} \theta(k - \beta a(t)H) \left[a_{\mathbf{k}} \phi_{\mathbf{k}}(t) e^{i\mathbf{k}\cdot\mathbf{x}} + a_{\mathbf{k}}^\dagger \phi_{\mathbf{k}}^*(t) e^{-i\mathbf{k}\cdot\mathbf{x}} \right], \quad (6.22)$$

where $\bar{\phi}$ is multiplied by the unity operator, and where $\beta \ll 1$ is a constant. The equation of motion for the coarse grained part $\bar{\phi}$ is, neglecting the terms with two derivatives,

$$\dot{\bar{\phi}}(t, \mathbf{x}) = -\frac{1}{3H} V'(\bar{\phi}) + f(t, \mathbf{x}), \quad (6.23)$$

with

$$f(t, \mathbf{x}) = \beta a(t)H^2 \int \frac{d^3k}{(2\pi)^3} \delta(k - \beta a(t)H) \left[a_{\mathbf{k}} \phi_{\mathbf{k}}(t) e^{i\mathbf{k}\cdot\mathbf{x}} + a_{\mathbf{k}}^\dagger \phi_{\mathbf{k}}^*(t) e^{-i\mathbf{k}\cdot\mathbf{x}} \right]. \quad (6.24)$$

At this point, equation (6.23) is reinterpreted [125] as a classical Langevin equation for the stochastic quantity $\bar{\phi}$, with a stochastic noise term $f(t, \mathbf{x})$ that has statistical properties characterized by expectation values of the quantum operator $f(t, \mathbf{x})$.

In [126, 127, 128, 129] this method has been applied to calculate non-Gaussianities in multifield inflation. Another use of the stochastic approach is in nonperturbative applications. As is well known (see also next chapter) corrections in de Sitter can grow after horizon exit and eventually become nonperturbatively large. The stochastic approach has been used to investigate this regime in [125, 130, 131, 132].

δN FORMALISM

The number of e-folds of inflation N from an initial time until the end of inflation can be obtained by integrating over the trajectories of the inflaton fields. For example the integral over the trajectory of the inflaton field in single field inflation is given by equations (1.9) and (1.10). Hence N depends on the initial values of the inflaton fields, and small perturbations $\delta\sigma^A$ in the initial conditions give small perturbations δN in the number of e-folds. The curvature perturbation ζ can be shown¹ to be equal to the perturbation δN , and can therefore be expanded as:

$$\zeta = \delta N = N_A \delta\sigma^A + \frac{1}{2} N_{AB} \delta\sigma^A \delta\sigma^B + \dots, \quad (6.25)$$

¹Here N is calculated as the number of e-folds between a flat hypersurface at initial time and a uniform-density hypersurface at final time.

where this ζ is again the ζ of equation (6.3), and where $N_A = \partial N / \partial \sigma^A$. In the δN formalism, correlation functions of ζ are expressed, via equation (6.25), in terms of correlation functions of the field perturbations $\delta\sigma^A$ at the initial time. Usually one takes this initial time to be the time of horizon exit of the modes one is interested in, and one assumes that the $\delta\sigma^A$ are Gaussian at this time.

Originally [133] the δN formalism was used to calculate the two point function of ζ in order to determine the power spectrum in multifield inflation models. Later the formalism was extended [134] to calculations of non-Gaussianities. N is calculated using classical physics, and as a consequence the δN formalism is classical.

Note that the perturbations $\delta\sigma^A$ are not homogeneous in space, but that N and its derivatives are always calculated using homogeneous fields. This is justified by the separate universe assumption: regions that are separated by at least a horizon distance H^{-1} cannot influence each other and evolve as separate universes. In practice this assumption acts as smoothing, because perturbations with wavelengths shorter than the horizon are neglected so that the fields can be considered to be homogeneous in each ‘separate universe’. This smoothing assumption is often left implicit, but it is not always valid. For example in [135], where non-Gaussianity from preheating is investigated, it is found that it is necessary to also consider the modes inside the horizon to obtain reliable results.

CHAPTER 7

CLASSICAL APPROXIMATION TO QUANTUM COSMOLOGICAL CORRELATIONS

7.1 INTRODUCTION

The precision of measurements of temperature fluctuations in the Cosmic Microwave Background radiation has increased enormously in the recent past and is expected to increase even more in the near future. From these measurements, statistical properties of the primordial cosmological perturbations can be deduced. They are found to have a nearly flat power spectrum, and to be close to Gaussian. Non-Gaussian effects (see [136] for a review) may be detected in the future and can provide a powerful tool to discriminate between different inflation models.

There is therefore a large interest in calculating the statistical properties of the primordial cosmological perturbations for different inflation models. In these calculations the cosmological perturbations are often parameterized by the curvature perturbation ζ , which is the perturbation in scalar curvature on time slices of uniform density. This parameterization is convenient because of the property that, under certain conditions, perturbations in ζ remain constant after their wavelengths have grown larger than the horizon length, i.e. after horizon exit. This has been shown for linear perturbation theory in [137], to all orders in ζ for single field inflation in [116], and nonperturbatively for adiabatic perturbations in [118]. The latter two references use a derivative expansion and therefore assume that effects from wavelengths of the order of the horizon and shorter are negligible.

In more complicated models for inflation, e.g. those involving multiple fields, the curvature perturbation ζ is not constant after horizon exit. Therefore evolution after horizon exit might lead to non-Gaussian effects, which has been investigated in [138, 139, 140, 126, 127, 128, 129, 141, 134, 108, 142, 143, 144, 145, 146, 147, 148, 149, 150, 151, 152, 153, 107]. These investigations have been done by solving classical equations of motion, which is assumed to be a good approximation to the quantum theory, because quantum effects are presumably negligible for wavelengths much longer than the horizon length (see [154] for a recent argument).

The goal of this chapter is to investigate up to which order corrections to cosmological correlation functions that are generated after horizon exit can be calculated reliably using classical physics. For this we study ϕ^3 theory on an exact de Sitter background for a massless minimally coupled scalar field ϕ , as toy model for the curvature perturbation ζ on an inflationary background. We consider correlation functions with (external) momenta much smaller than the Hubble scale H in the quantum theory, using the Closed Time Path (CTP) formalism (also known as in-in formalism, see e.g. [155, 156]), as is also done by Weinberg in [102, 103]. Furthermore we formulate a classical theory with statistical fluctuations, in such a way that correlation functions in this theory can easily be compared with those in the quantum theory.

In short our results for the ϕ^3 toy model are that the tree level contributions in the quantum theory can be approximated quite well by classical physics (which sounds trivial, but we argue that this is not completely so). As was argued in [102, 103] there can be loop corrections that grow after horizon exit. We find that a classical approximation is expected to be able to reproduce a certain class of these corrections, but not all of them. The reason is that loop integrals get growing contributions not only from loop momenta with magnitude of the order of the external momenta (which are smaller than H), but also from loop momenta of the order of H . This is supported by an explicit calculation of the one loop correction to the two point function, where we use a small mass as infrared regulator. We argue that a classical approximation is not expected to be good at scales around H , and that in general it cannot reproduce contributions from these loop momenta. An exception is the one loop correction, for which we find that the classical approximation can be saved by choosing a suitable ultraviolet cutoff.

We generalize the arguments for the toy model to derivative interactions, and apply them to the curvature perturbation ζ . This leads to the conclusion that corrections to correlation functions generated after horizon exit in multifield inflation models can, up to one loop level, be approximated by classical physics. We also compare with a theorem derived by Weinberg [102]. We find that it is not excluded that there are corrections to correlation functions of ζ that grow after horizon exit, even in single field inflation.

We remark that the problem we are addressing is related to, but different from the problem of the quantum-to-classical transition [157, 158, 159, 160, 161, 162], that deals with

the way quantum fluctuations acquire classical properties by decoherence, and with the production of entropy. In this chapter we are not investigating how a quantum system evolves to a classical system; we are considering a quantum system and a classical system separately from each other and investigate how well the classical system can reproduce correlation functions of the quantum system.

In the next section we recall the CTP formalism, using a variation of the Keldysh-basis, and apply it to ϕ^3 theory on a de Sitter background (for other applications of the CTP formalism to interacting fields in cosmology see [163, 164, 165, 166, 167, 168, 169, 170, 171, 172, 173, 174, 175, 176, 177, 104, 105, 106]). Subsequently we analyze contributions to correlation functions with small external momenta, that are generated after horizon exit (but still during inflation). In section 7.3 we show how correlation functions in classical ϕ^3 theory on a de Sitter background can be calculated perturbatively, starting from given initial conditions. The perturbative contributions are graphically represented in a way that is similar to Feynman diagrams in the quantum theory. Next in section 7.4 we argue that the classical theory can approximate the contributions from small internal momenta in the quantum theory quite well, but that this is in general not the case for large internal momenta. The one loop correction is an exception: we show that by choosing a suitable ultraviolet cutoff, the classical approximation can be good. We generalize our arguments and conclude in section 7.5.

In Appendix B details of the quantization are given and a comparison is made with finite temperature field theory. Appendix C contains an argument on closed retarded loops. In Appendix D diagrams in the classical and quantum theory are compared. To illustrate the arguments in this chapter, we give in Appendix E the detailed calculations of the one loop correction to the two point function in the ϕ^3 toy model, that is generated after horizon exit.

7.2 QUANTUM THEORY

In this section we set up the quantum theory using the CTP formalism, and analyze the contributions to correlation functions that are generated after horizon exit.

The Lagrangian density of ϕ^3 theory is

$$\mathcal{L}[\phi] = \sqrt{-g} \left(-\frac{1}{2} \partial_\mu \phi \partial^\mu \phi - \frac{1}{2} m^2 \phi^2 - \frac{1}{2} \xi R \phi^2 - \frac{\lambda}{3!} \phi^3 \right) + \delta \mathcal{L} \quad (7.1)$$

where we are using a metric $g_{\mu\nu}$ with signature $-+++$. Except when we need the mass m as infrared regulator, we take $m = 0$ and $\xi = 0$ to obtain a massless minimally coupled scalar field. The term $\delta \mathcal{L}$ contains the counterterms:

$$\delta \mathcal{L} = \sqrt{-g} \left(-\delta_1 \phi - \frac{1}{2} \delta_Z \partial_\mu \phi \partial^\mu \phi - \frac{1}{2} \delta_m \phi^2 - \frac{\delta_\lambda}{3!} \phi^3 \right). \quad (7.2)$$

We added a linear counterterm δ_1 to keep $\langle\phi\rangle = 0$ for all times, at one loop level¹, hence up to $\mathcal{O}(\lambda^3)$. The potential can be stabilized by adding a ϕ^4 term if desired. We use a spatial momentum cutoff Λ as ultraviolet regulator. Then

$$\delta_m = \frac{\lambda^2}{4(2\pi)^2} \ln \frac{\Lambda}{\mu} + \mathcal{O}(\lambda^4), \quad (7.3)$$

where μ is a renormalization scale.

7.2.1 CLOSED TIME PATH FORMALISM ON A DE SITTER BACKGROUND

CTP FORMALISM

In a system with time-dependent Hamiltonian $H(t)$, that starts in a state $|\text{in}\rangle$ at initial time t_i , the expectation value of an operator Q at time $t > t_i$ is given by

$$\langle Q(t) \rangle = \left\langle \text{in} \left| \left[\bar{\text{T}} \exp \left(i \int_{t_{\text{in}}}^t dt' H(t') \right) \right] Q \left[\text{T} \exp \left(-i \int_{t_{\text{in}}}^t dt' H(t') \right) \right] \right| \text{in} \right\rangle, \quad (7.4)$$

where T means a time-ordered product and $\bar{\text{T}}$ an anti-time-ordered product. In the Closed Time Path (CTP) formalism (or in-in formalism) [156] this expectation value can also be calculated using path integrals, from the generating functional

$$Z[J_+, J_-, \rho(t_{\text{in}})] = \int \mathcal{D}\phi_{\text{in}}^+ \mathcal{D}\phi_{\text{in}}^- \langle \phi_{\text{in}}^+ | \rho(t_{\text{in}}) | \phi_{\text{in}}^- \rangle \times \int_{\phi_{\text{in}}^+}^{\phi_{\text{in}}^-} \mathcal{D}\phi^+ \mathcal{D}\phi^- \exp \left[i \int_{t_{\text{in}}}^t dt' \int d^3x (\mathcal{L}[\phi^+] - \mathcal{L}[\phi^-] + J_+ \phi^+ + J_- \phi^-) \right]. \quad (7.5)$$

The path integral on the second line can be written in short-hand notation as

$$\int \mathcal{D}\phi \exp \left[i \int_{\mathcal{C}} dt' \int d^3x (\mathcal{L}[\phi] + J\phi) \right], \quad (7.6)$$

where \mathcal{C} is the so-called Schwinger-Keldysh contour which runs from t_{in} to t and back. The field ϕ and source J are split up in ϕ^+ , J_+ on the first part of this contour, and ϕ^- , J_- on the second part, with the condition $\phi^+(t) = \phi^-(t)$. The integration along the contour \mathcal{C} explains the name Closed Time Path formalism. The path integral on the first line of equation (7.5) imposes that at the initial time t_{in} the state of the system is given by the

¹It can be checked that this is possible by calculating the tadpole diagram, using the F two point function of equation (7.24) and the infrared and ultraviolet regulators as discussed later in this chapter.

density matrix $\rho(t_{\text{in}})$. Expectation values are obtained by variation of the sources J_+ and J_- :

$$\langle \bar{\text{T}}(\phi(x_1) \dots \phi(x_n)) \text{T}(\phi(x_{n+1}) \dots \phi(x_{n+m})) \rangle = \left. \frac{\delta^{n+m} Z[J_+, J_-, \rho(t_{\text{in}})]}{\delta J_-(x_1) \dots \delta J_-(x_n) \delta J_+(x_{n+1}) \dots \delta J_+(x_{n+m})} \right|_{J_+, J_- = 0}, \quad (7.7)$$

where the times x_j^0 are smaller than or equal to the time t used in definition (7.5).

When calculating these correlation functions perturbatively, we need to know the free two point functions with all four possible time orderings:

$$G^{-+}(x, y) = i \langle \phi(x) \phi(y) \rangle^{(0)}, \quad (7.8)$$

$$G^{+-}(x, y) = i \langle \phi(y) \phi(x) \rangle^{(0)}, \quad (7.9)$$

$$G^{++}(x, y) = i \langle \text{T} \phi(x) \phi(y) \rangle^{(0)} = \theta(x_0 - y_0) G^{-+}(x, y) + \theta(y_0 - x_0) G^{+-}(x, y), \quad (7.10)$$

$$G^{--}(x, y) = i \langle \bar{\text{T}} \phi(x) \phi(y) \rangle^{(0)} = \theta(x_0 - y_0) G^{+-}(x, y) + \theta(y_0 - x_0) G^{-+}(x, y), \quad (7.11)$$

where the superscript (0) denotes the free field correlation functions. They obey the identity

$$G^{++}(x, y) + G^{--}(x, y) = G^{-+}(x, y) + G^{+-}(x, y), \quad (7.12)$$

and they can be put together in a matrix:

$$\mathbf{G}(x, y) = \begin{pmatrix} G^{++}(x, y) & G^{+-}(x, y) \\ G^{-+}(x, y) & G^{--}(x, y) \end{pmatrix}. \quad (7.13)$$

Note that the two point functions depend on the initial conditions via the dependence on $\rho(t_i)$ of the generating functional (7.5).

In the context of the classical approximation it is useful to transform the ϕ^+ and ϕ^- fields to a different basis, which is a variation of the Keldysh basis (see also [178]):

$$\begin{pmatrix} \phi^{(1)} \\ \phi^{(2)} \end{pmatrix} = \begin{pmatrix} (\phi^+ + \phi^-)/2 \\ \phi^+ - \phi^- \end{pmatrix} = \mathbf{R} \begin{pmatrix} \phi^+ \\ \phi^- \end{pmatrix}, \quad \text{with} \quad \mathbf{R} = \begin{pmatrix} 1/2 & 1/2 \\ 1 & -1 \end{pmatrix}. \quad (7.14)$$

The Lagrangian density $\mathcal{L}[\phi^+] - \mathcal{L}[\phi^-]$ transforms to

$$\mathcal{L}[\phi^{(1)}, \phi^{(2)}] = \sqrt{-g} \left(-\partial_\mu \phi^{(1)} \partial^\mu \phi^{(2)} - (m^2 + \xi R) \phi^{(1)} \phi^{(2)} + \right. \\ \left. - \frac{\lambda}{3!} \left(3(\phi^{(1)})^2 \phi^{(2)} + \frac{1}{4} (\phi^{(2)})^3 \right) \right). \quad (7.15)$$

The free two point functions in this basis can easily be obtained by the transformation

$$\mathbf{G}_K(x, y) = \mathbf{R}\mathbf{G}(x, y)\mathbf{R}^T = \begin{pmatrix} iF(x, y) & G^R(x, y) \\ G^A(x, y) & 0 \end{pmatrix}, \quad (7.16)$$

with

$$F(x, y) = -\frac{i}{2} (G^{-+}(x, y) + G^{+-}(x, y)), \quad (7.17)$$

$$G^R(x, y) = G^{++}(x, y) - G^{+-}(x, y) = \theta(x_0 - y_0) (G^{-+}(x, y) - G^{+-}(x, y)), \quad (7.18)$$

$$G^A(x, y) = G^{++}(x, y) - G^{-+}(x, y) = \theta(y_0 - x_0) (G^{+-}(x, y) - G^{-+}(x, y)), \quad (7.19)$$

where we have used identity (7.12). They obey the equations

$$(\square_x + m^2 + \xi R(x)) F(x, y) = 0, \quad (7.20)$$

$$(\square_x + m^2 + \xi R(x)) G^{R,A}(x, y) = \frac{\delta^4(x - y)}{\sqrt{-g(x)}}, \quad (7.21)$$

with

$$\square_x = \frac{1}{\sqrt{-g(x)}} \partial_\mu \left(\sqrt{-g(x)} g^{\mu\nu}(x) \partial_\nu \right). \quad (7.22)$$

The G^R and G^A two point functions are often called the retarded and advanced propagators. Note that $G^A(x, y) = G^R(y, x)$.

FEYNMAN RULES ON A DE SITTER BACKGROUND

The metric of the de Sitter background is

$$ds^2 = -dt^2 + a^2(t) d\mathbf{x}^2, \quad (7.23)$$

where $a(t)$ is the FRW scale factor. The Hubble rate is $H = \dot{a}/a$. In de Sitter space the scale factor is $a(t) = a_0 \exp(Ht)$. We will use conformal time $\tau = -\int_t^\infty dt'/a(t')$, which runs from $-\infty$ to 0. The scale factor in conformal time is $a(\tau) = -1/H\tau$.

As initial state $\rho(\tau_{\text{in}})$ we take the adiabatic or Bunch-Davies vacuum for $\tau_{\text{in}} \rightarrow -\infty$. One expects that other choices will give the same results because this state is an attractor state [179, 180]. The free field operator with this initial state is given in equation (B.5) in

Appendix B and it can be used to derive the free two point functions (7.17)-(7.19):

$$F(k, \tau_1, \tau_2) = \frac{H^2}{2k^3} \left[(1 + k^2 \tau_1 \tau_2) \cos k(\tau_1 - \tau_2) + k(\tau_1 - \tau_2) \sin k(\tau_1 - \tau_2) \right], \quad (7.24)$$

$$G^R(k, \tau_1, \tau_2) = \theta(\tau_1 - \tau_2) \frac{H^2}{k^3} \left[(1 + k^2 \tau_1 \tau_2) \sin k(\tau_1 - \tau_2) + k(\tau_1 - \tau_2) \cos k(\tau_1 - \tau_2) \right], \quad (7.25)$$

and $G^A(k, \tau_1, \tau_2) = G^R(k, \tau_2, \tau_1)$. Here the two point functions depend only on the length of the spatial momentum $k = |\mathbf{k}|$. Representing the $\phi^{(1)}$ field with a full line and the $\phi^{(2)}$ field with a dashed line, the Feynman rules for the two point functions, the vertices and the counterterm are²

$$\frac{\tau_1 \text{---} \tau_2}{\text{---}} = F(k, \tau_1, \tau_2), \quad (7.26)$$

$$\frac{\tau_1 \text{---} \tau_2}{\text{---}} = -iG^R(k, \tau_1, \tau_2) = -iG^A(k, \tau_2, \tau_1), \quad (7.27)$$

$$\begin{array}{c} \tau_2 \\ \diagup \\ \tau_1 \text{---} \\ \diagdown \\ \tau_3 \end{array} = -i\lambda a^4(\tau_1) \delta(\tau_1 - \tau_2) \delta(\tau_1 - \tau_3), \quad (7.28)$$

$$\begin{array}{c} \tau_2 \\ \diagup \\ \tau_1 \text{---} \\ \diagdown \\ \tau_3 \end{array} = -\frac{i\lambda}{4} a^4(\tau_1) \delta(\tau_1 - \tau_2) \delta(\tau_1 - \tau_3), \quad (7.29)$$

$$\tau_1 \text{---} \otimes \tau_2 = -ia^4(\tau_1) \delta(\tau_1 - \tau_2) \delta_m. \quad (7.30)$$

When a two point function is attached to a vertex, the corresponding time has to be integrated over. A closed loop corresponds with an integral over spatial momentum $\int d^3p/(2\pi)^3$.

EXAMPLE: EQUAL TIME TWO POINT FUNCTION

As an example to which we will return repeatedly, we consider the equal time two point function up to one loop level:

$$\int d^3x e^{-i\mathbf{k}\cdot\mathbf{x}} \langle \phi(\tau, \mathbf{x}) \phi(\tau, \mathbf{0}) \rangle. \quad (7.31)$$

The tree level contribution is given by

$$\frac{\tau \text{---} \tau}{\text{---}} = F(k, \tau, \tau). \quad (7.32)$$

²These Feynman rules should not be confused with the graphical representation developed in [181].

7.2.2 LATE TIMES

COSMOLOGICAL CORRELATION FUNCTIONS

In this chapter we consider cosmological correlation functions, by which we mean equal time correlation functions

$$\int d^3x_1 \dots d^3x_r e^{-i\mathbf{k}_1 \cdot \mathbf{x}_1 - \dots - i\mathbf{k}_r \cdot \mathbf{x}_r} \langle \phi(\tau, \mathbf{x}_1) \dots \phi(\tau, \mathbf{x}_r) \phi(\tau, \mathbf{0}) \rangle, \quad (7.36)$$

where the time τ is late, i.e. is well after horizon exit with respect to the spatial momenta k_i , which can be expressed as $|k_i\tau| \ll 1$. Similarly, early times are times for which $|k_i\tau| \gg 1$.

We constrain the analysis further by only considering contributions to these cosmological correlation functions that are generated after horizon exit. For this we introduce a split in time at τ_H , a few (N_H) e-folds after horizon exit, such that $|k\tau_H| = \exp(-N_H) \ll 1$. Correlation functions at τ_H have accumulated contributions from earlier times, of which we only keep the free field contributions. Then we use these correlation functions as initial conditions for the evolution after τ_H . In practice this means that we use the Feynman rules as described in the previous subsection, with the only difference that we take τ_H as initial time. This procedure is not completely correct because the neglected contributions generated before τ_H are of the same order in the coupling constant as the contributions generated after τ_H . But it does not change the qualitative behaviour of the contributions generated after τ_H , and neglecting the contributions from before τ_H simplifies the calculations significantly. We comment further on this point in section 7.5.1.

Different contributions to cosmological correlation functions (7.36) depend in different ways on the time τ . Those that are proportional to positive powers of τ are dominated by their values at the initial time τ_H . These contributions are negligible if τ_H is taken sufficiently long after horizon exit. Contributions that are proportional to a non-positive power of τ can grow after horizon exit and will therefore dominate. In [102, 103] it is shown that these contributions do not grow faster than powers of $\ln(-H\tau)$, so negative powers of τ do not occur. In this chapter we call contributions that are proportional to τ^0 (including powers of $\ln(-H\tau)$) late time contributions. In this subsection we analyze the dependence on τ of the different contributions by counting powers of τ .

Contributions can contain integrals over spatial internal (loop) momenta p , which can be arbitrarily large. We have found that the power counting goes quite differently for small internal momenta (smaller than the Hubble scale H , i.e. $|p\tau| \ll 1$) than for large internal momenta (of the order of the Hubble scale and larger, i.e. $|p\tau| \gtrsim 1$). Therefore we analyze first the case that all internal momenta are small, and consider then arbitrary (amputated) IPI diagrams for which all the internal momenta are large and the external

momenta are small. These 1PI diagrams can be treated as effective (non-local) couplings in the analysis for small internal momenta, and in this way our analysis covers the whole range of internal momenta. After this general analysis, we compare our results with the specific case of the one loop correction to the two point function.

SMALL INTERNAL MOMENTA

When the internal momenta are small, the expressions for the free two point functions F (7.24) and G^R (7.25) can be expanded in $k\tau_i$:

$$F(k, \tau_1, \tau_2) = \frac{H^2}{2k^3} [1 + \mathcal{O}(k^2\tau_i^2)], \quad (7.37)$$

$$G^R(k, \tau_1, \tau_2) = \theta(\tau_1 - \tau_2) \frac{H^2}{3k^3} [k^3(\tau_1^3 - \tau_2^3) + \mathcal{O}(k^5\tau_i^5)], \quad (7.38)$$

where $k^2\tau_i^2$ indicate all possible combinations $k^2\tau_1^2$, $k^2\tau_1\tau_2$ and $k^2\tau_2^2$, and similarly for $k^5\tau_i^5$. Using the lowest order of these expansions, it is easy to count the powers of τ_i of the contribution of an arbitrary Feynman diagram. The F two point function does not contribute any factor of τ_i , and the G^R two point function gives a factor of τ_i^3 . Furthermore, a vertex contributes a factor $a^4(\tau_i) \propto \tau_i^{-4}$, and an integral $\int d\tau_i \propto \tau_i$, so effectively it contributes a factor τ_i^{-3} .

We can divide the Feynman diagrams into two classes: diagrams that contain only vertices with one dashed line (diagrams A, B and D in the example of the two point function (7.33)), and diagrams that contain one or more vertices with three dashed lines (diagram C in (7.33)). Because each dashed line is attached to a G^R two point function, diagrams of the first class have an equal number of vertices as G^R two point functions. Each vertex contributes a factor τ_i^{-3} and each G^R two point function a factor of τ_i^3 and therefore diagrams from the first class are proportional to τ_i^0 . Because these diagrams can contain integrals like $\int d\tau_i/\tau_i$, they can be proportional to powers of $\ln(-\tau_i)$, which are largest for the upper limit of the time integrals, i.e. τ .

Diagrams from the second class have more G^R two point functions than vertices, and are therefore proportional to positive powers of τ_i . For example a diagram with one vertex with three dashed lines has two more G^R two point functions than if this vertex would have had one dashed line, and is therefore suppressed by a factor of $|k\tau_i|^6$. The contributions from diagrams of the second class are largest for the lower limit of the time integrals, i.e. for τ_H . Therefore the contributions of diagrams from this class are suppressed with respect to contributions of the first class by a factor of $|k\tau_H|^6 = \exp(-6N_H)$, and they do not have the growing factors of $\ln(\tau/\tau_H)$.

The power counting of τ_i that is done here is similar to the power counting of the scale factor a in the derivation of the theorem in [102]. The expansion of the two point functions

(7.37) and (7.38) can be compared with the asymptotic expansions of the wavefunctions for late times in [102]. The difference is that here we use power counting to differentiate between growing and vanishing contributions to correlation functions for a specific (ϕ^3) interaction, whereas in [102] it was used to differentiate between interactions leading to different late time behaviour. We return to this in section 7.5.2.

LARGE INTERNAL MOMENTA

We consider an arbitrary amputated 1PI diagram, which has small external momenta, and we integrate the internal momenta starting at a scale M somewhat smaller than H . We use a cutoff Λ as ultraviolet regulator. Because both M and Λ are physical scales and not comoving scales, the limits of the momentum integrals are time dependent: $Ma(\tau_i)$ and $\Lambda a(\tau_i)$, where τ_i corresponds to the time of one of the vertices. We take for this time the earliest time that occurs in the loop, because that corresponds with the smallest cutoff.³ In this way the momentum integrals do also contribute time dependencies, which we also have to take into account.

Suppose that our arbitrary amputated 1PI diagram has E external lines and N vertices, each with V legs. Then there are P internal lines and L loops with

$$P = \frac{1}{2} (NV - E), \quad (7.39)$$

$$L = \frac{1}{2} (NV - E) - N + 1. \quad (7.40)$$

Furthermore from equations (7.24) and (7.25) we see that each internal two point function contributes factors proportional to

$$\frac{(p_i \tau_{j_1})^{n_\beta}}{p_i^3} e^{\pm i p_i \tau_{j_2}}, \quad (7.41)$$

where $n_\beta = 0, 1, 2$. Each vertex gives $\int d\tau_j / \tau_j^4$, and each loop gives an integral $\int d^3 p_i$. We ignore powers of the external momenta because the internal momenta are much larger, $p \gg k$. Then we can count the powers of p and τ of the diagram:

$$p_i^{(-3+n)P+3L-l} \tau_j^{-3N+nP-l} \left| \begin{array}{l} \Lambda a(\tau_j) \\ Ma(\tau_j) \end{array} \right. \rightarrow \left(\frac{\Lambda}{H} \right)^{\frac{n}{2}(NV-E)-3N-l+3} \tau_j^{-3}, \quad (7.42)$$

where n is the sum of the n_β , and where l is a non-negative integer that represents the fact that p integrals can also lead to factors of $1/\tau$ instead of an extra factor p (see e.g. the integrals (E.22)-(E.30) in the example calculation of Appendix E). We ignore the contribution from the lower limit $Ma(\tau_j)$, because the full result cannot depend on the split in the integrals.⁴

³If an ultraviolet divergence is local, it occurs only if the times of the vertices in the loop are equal (i.e. they are proportional to $\delta(\tau_{j_1} - \tau_{j_2})$ for all times τ_{j_i}); then it does not matter which time one chooses.

⁴This is confirmed for the specific case considered in Appendix E.

Apparently the power of τ_j is independent of the details of the calculation: contributions from large internal momenta to 1PI diagrams are always proportional to τ_j^{-3} .

We can now compare the 1PI diagram, seen as an effective coupling, with a tree level coupling. They are both proportional to τ_j^{-3} , but they differ in the possible numbers of (external) dashed lines. The 1PI diagrams can have any number of dashed lines, instead of one or three dashed lines for the tree level coupling. However, as shown in Appendix C, it turns out that 1PI diagrams with no external dashed lines vanish. Hence the non-vanishing 1PI diagrams can have one or more external dashed lines.

The 1PI diagrams, being effective couplings for small momenta, can be put into the analysis for small internal momenta of section 7.2.2. The power counting argument of that section shows that only those effective couplings with one external dashed line can lead to contributions proportional to τ^0 . Effective couplings with more external dashed lines lead to contributions that are suppressed by (at least) a factor $|k\tau_H|^3$.

The power of Λ/H in equation (7.42) does depend on the details of the calculation. When it is non-negative, it can cause an ultraviolet divergence. Some divergent terms are proportional to $\delta(\tau_{j_1} - \tau_{j_2})$ for all the times τ_{j_i} that occur in the loop. These divergences are the usual local divergences and are canceled by counterterms. Non-local divergent terms can also occur (an example of this is given below), as a consequence of the way in which the total correction is split up in contributions from individual diagrams. They must cancel between different contributions in order to make the total result finite.

It is interesting to consider the errors that occur when the ultraviolet regulator Λ is not taken to infinity but kept finite. From equation (7.42) it is clear that, after the counterterms have been taken into account, the errors will be proportional to positive powers of H/Λ . Hence if Λ is taken to be smaller than H , large errors occur, but if Λ is taken to be larger than H the errors are suppressed. Clearly, internal momenta of the order magnitude of the Hubble scale H still contribute to the correlation functions, even though H is much larger than the external momenta $k/a(\tau)$. This is a feature of quantum field theory in de Sitter space that is different from what one would expect from field theory in flat space. In the latter case, from the point of view of effective field theories, one expects only contributions from internal momenta of the order of magnitude of the external momenta. Contributions from higher scales are said to decouple. In de Sitter space, scales decouple only when they are larger than the Hubble scale H .

EXAMPLE: LATE TIME CONTRIBUTIONS TO EQUAL TIME TWO POINT FUNCTION AT ONE LOOP

The general analysis of this subsection can be checked in the example of the late time contributions to the one loop correction to the two point function (7.33), as calculated in

Appendix E. In this calculation the momenta are split up between small and large at a comoving scale M_{cm} , which obeys $|M_{\text{cm}}\tau| \ll 1$ and $M_{\text{cm}} > k$.

Small internal momenta. The results for small internal momenta of diagrams A and B are given in equations (E.11) and (E.58), respectively. Diagram C does not give any late time contribution. After attaching the external lines, the dominant terms can be found in equations (E.49) and (E.71) and are proportional to

$$\frac{\lambda^2}{\delta} \ln^2 \frac{\tau}{\tau_H} \quad \text{with} \quad \delta = \frac{m^2}{3H^2}, \quad \text{or} \quad \lambda^2 \ln^3 \frac{\tau}{\tau_H}, \quad (7.43)$$

depending on the values of δ and $\ln(\tau/\tau_H)$, where δ is the infrared regulator. In this calculation we have used an expansion that is valid for $|\delta \ln(-k\tau)| < 1$, and therefore this calculation is only valid for a limited amount of time. When $|\delta \ln(-k\tau)|$ approaches 1, the term on the right in (7.43) becomes of comparable magnitude to the term on the left.

Two powers of the logarithm $\ln(\tau/\tau_H)$ come from the two time integrals corresponding with the two vertices. The extra factor of $\ln(\tau/\tau_H)$ in the term on the right in (7.43), is the consequence of the momentum integration, and was observed earlier in a similar calculation in [175], where also a small mass was used as infrared regulator.

Large internal momenta. For large momenta the result for the amputated diagrams are given in (E.42) for diagrams A and D, (E.61) and (E.62) for diagram B and (E.65) for diagram C. Diagram A has a local ultraviolet divergence that is canceled by the counterterm, diagram D. Diagrams B and C have divergent terms that are non-local and that cancel each other. The finite remainder is suppressed for late times. The contribution (E.62) from diagram B only removes the dependence on the scale M_{cl} . Therefore only diagram A leads to late time contributions, in agreement with the result above that late time contributions can only come from 1PI diagrams with one external dashed line.

The term from diagram A that grows quickest for large internal momenta, after attaching the external lines, can be found in equation (E.49) and is proportional to

$$\lambda^2 \ln^3 \frac{\tau}{\tau_H}, \quad (7.44)$$

which is comparable to the term on the right in (7.43) for the small internal momenta.

Complete result for the one loop correction. The complete result of the late time contributions to the one loop correction is two times equation (E.49) added to equation

(E.71), which gives

$$\begin{aligned} & \frac{\lambda^2}{36(2\pi)^2 k^3} \left\{ \frac{7}{9\delta} + \frac{392}{27} - \frac{7}{3}\gamma - \frac{17}{18}\pi^2 - \frac{4}{3}\ln 2 - 4\zeta(3) - \ln \frac{2\mu}{H} + \frac{4}{9}\ln(-k\tau_H) + \right. \\ & \left. \left(\frac{2}{\delta} + 15 - \frac{17}{3}\gamma - \frac{2}{3}\pi^2 - \frac{8}{3}\ln 2 - 3\ln \frac{2\mu}{H} + \frac{8}{3}\ln(-k\tau_H) \right) \ln \frac{\tau}{\tau_H} + \right. \\ & \left. \left(\frac{2}{\delta} + \frac{22}{3} - 2\gamma - 2\ln 2 + 4\ln(-k\tau_H) \right) \ln^2 \frac{\tau}{\tau_H} + \frac{8}{3}\ln^3 \frac{\tau}{\tau_H} + \mathcal{O}\left(\frac{\tau}{\tau_H}\right) + \mathcal{O}(\delta) \right\}. \end{aligned} \quad (7.45)$$

Note that a consequence of the growing behaviour of loop corrections is that the theory becomes nonperturbative if one waits long enough.

7.3 CLASSICAL THEORY

In this section we consider classical ϕ^3 theory for a massless minimally coupled field ϕ . The evolution of classical fields on a de Sitter background is governed by the equation of motion (which can be derived from the Lagrangian density (7.1))

$$\partial_\tau^2 \phi(x) + 2Ha(\tau)\partial_\tau \phi(x) - \nabla^2 \phi(x) + a^2(\tau)\frac{\lambda}{2!}\phi^2(x) = 0, \quad (7.46)$$

where we use $x = (\tau, \mathbf{x})$ with τ conformal time. Initial conditions have to be imposed at an initial time τ_{in} . We focus on the calculation of equal time correlation functions

$$\langle \phi(\tau, \mathbf{x}_1) \dots \phi(\tau, \mathbf{x}_n) \rangle_{\text{cl}}, \quad (7.47)$$

where the subscript ‘‘cl’’ denotes a correlation function in the classical theory. In this section we show how to calculate these correlation functions in a way that is similar to the interaction picture in quantum field theory: first we calculate the free field correlation functions starting from the initial conditions and using the free equations of motion, and then we calculate perturbative corrections, expressed in terms of these free field correlation functions. In [182, 178] this method was used in the context of thermal field theory. Furthermore we show that the contributions to the correlation functions can be represented graphically in a way that is similar to Feynman diagrams.

7.3.1 PERTURBATIVE CALCULATION OF CORRELATION FUNCTIONS

We assume that at the initial time τ_{in} initial conditions are given for the correlation functions

$$\langle \phi(\tau_{\text{in}}, \mathbf{x}_1) \dots \phi(\tau_{\text{in}}, \mathbf{x}_n) \rangle_{\text{cl}}, \quad (7.48)$$

and first order time derivatives of these correlation functions. In the free field case ($\lambda = 0$), the initial conditions can be evolved in time using the free field equations of motion. Then one obtains the free field correlation functions

$$\langle \phi_0(\tau_1, \mathbf{x}_1) \dots \phi_0(\tau_n, \mathbf{x}_n) \rangle_{\text{cl}}, \quad (7.49)$$

where the subscript “0” denotes the free field solutions, and where the times τ_1, \dots, τ_n do not have to be equal.

To calculate perturbative corrections to the correlation functions, we first solve the classical equation of motion for $\phi(x)$ perturbatively. The first order correction is

$$\phi_1(x) = -\frac{\lambda}{2!} \int d^4y a^4(y_0) G^R(x, y) \phi_0^2(y), \quad (7.50)$$

where y_0 denotes conformal time, and where the retarded propagator $G^R(x, y)$ is the solution of

$$\frac{1}{a^2(x_0)} (\partial_{x_0}^2 + 2Ha(x_0)\partial_{x_0} - \nabla^2) G^R(x, y) = \frac{\delta^4(x - y)}{a^4(x_0)}, \quad (7.51)$$

where we used the de Sitter metric (7.23). This equation is the same as (7.21), so that the retarded propagator in the classical theory is equal to the one in quantum theory, given in equation (7.25) after a spatial Fourier transform. Higher order perturbative corrections to the solution of the equation of motion are obtained by

$$\phi_i(x) = -\frac{\lambda}{2!} \int d^4y a^4(y_0) G^R(x, y) \sum_{j=0}^{i-1} \phi_j(y) \phi_{i-j-1}(y). \quad (7.52)$$

By iteration the i -th order solution can be expressed in terms of the zeroth order solution $\phi_0(x)$. The full perturbative solution of the equation of motion (7.46) is the sum

$$\phi(x) = \sum_i \phi_i(x). \quad (7.53)$$

Perturbative corrections to the correlation function (7.47) are obtained by replacing the $\phi(x_i)$'s in (7.47) by the perturbative solution (7.53), and ordering the terms according to the total powers of λ :

$$\langle \phi(\tau, \mathbf{x}_1) \dots \phi(\tau, \mathbf{x}_n) \rangle_{\text{cl}} = \sum_r \langle \phi(\tau, \mathbf{x}_1) \dots \phi(\tau, \mathbf{x}_n) \rangle_{\text{cl}}^r, \quad (7.54)$$

with

$$\langle \phi(\tau, \mathbf{x}_1) \dots \phi(\tau, \mathbf{x}_n) \rangle_{\text{cl}}^r = \sum_{i_1 + \dots + i_n = r} \langle \phi_{i_1}(\tau, \mathbf{x}_1) \dots \phi_{i_n}(\tau, \mathbf{x}_n) \rangle_{\text{cl}}. \quad (7.55)$$

When the ϕ_{i_j} 's are completely expressed in terms of free field solutions $\phi_0(x)$, the corrections to the correlation function (7.55) are expressed in terms of free field correlation functions, which we have obtained from the free equations of motion and the initial conditions in (7.49).

7.3.2 GRAPHICAL REPRESENTATION

When we choose the initial conditions to be Gaussian, it is possible to represent the contributions on the right hand side of equation (7.55) graphically in a way that is similar to the Feynman diagrams of the quantum theory. In the free field case, Gaussian initial conditions evolve to Gaussian free field correlation functions. Therefore the free field correlation functions are completely determined by the two point function, which we call suggestively F_{cl} :

$$F_{\text{cl}}(x_1, x_2) = \langle \phi_0(x_1)\phi_0(x_2) \rangle_{\text{cl}}. \quad (7.56)$$

We assign graphical rules analogously to the quantum case:

$$\frac{x \quad y}{\text{---}} = -iG^R(x, y), \quad (7.57)$$

$$\frac{x \quad y}{\text{—}} = F_{\text{cl}}(x, y), \quad (7.58)$$

$$\text{---} \begin{array}{l} \diagup \\ \diagdown \end{array} = \frac{-i\lambda}{2} \int d^4y a^4(y_0), \quad (7.59)$$

and furthermore

$$\frac{x}{\text{---}\times} = \phi_0(x). \quad (7.60)$$

The r -th order corrections on the right-hand side of equation (7.55) can be constructed graphically in two steps. First the ϕ_i 's of equation (7.52) are represented by tree graphs where the endpoint x and the i vertices are connected to each other by G^R propagators. The remaining free legs of the vertices are occupied by the ϕ_0 's of (7.60). For example the second order solution $\phi_2(x)$ can be represented by

$$\begin{array}{c} x \\ \text{---} \diagdown \\ \diagup \times \\ \diagdown \times \end{array} \quad \phi_2(x) = 2 \int d^4y a^4(y_0) (-i)G^R(x, y) \frac{-i\lambda}{2!} \phi_0(y) \times \int d^4z a^4(z_0) (-i)G^R(y, z) \frac{-i\lambda}{2!} \phi_0^2(z), \quad (7.61)$$

where the factor 2 comes from two equal contributions.

In the second step the tree graphs representing the ϕ_{i_j} in (7.55) are glued together at the crosses in all possible ways. When two crosses are glued together, a full line is created representing the free two point function (7.58). Consider for example the contribution $\langle \phi_2(x_1)\phi_0(x_2) \rangle_{\text{cl}}$ to the second order two point function $\langle \phi(x_1)\phi(x_2) \rangle_{\text{cl}}^{(2)}$. The tree

graphs representing $\phi_2(x_1)$ and $\phi_0(x_2)$ can be glued together in two ways:

$$\begin{aligned}
 \text{---}x_1 \text{---} \bigcirc \text{---}x_2 & \quad (-i)^2(-i\lambda)^2 \int d^4y a^4(y_0) G^R(x_1, y) \times \\
 & \quad \int d^4z a^4(z_0) G^R(y, z) F_{\text{cl}}(y, z) F_{\text{cl}}(z, x_2), \quad (7.62)
 \end{aligned}$$

(where an extra factor 2 comes from two ways of contracting the ϕ_0 's), and

$$\begin{aligned}
 \text{---}x_1 \text{---} \bigcirc \text{---}x_2 & \quad \frac{(-i)^2(-i\lambda)^2}{2} \int d^4y a^4(y_0) G^R(x_1, y) F_{\text{cl}}(y, x_2) \times \\
 & \quad \int d^4z a^4(z_0) G^R(y, z) F_{\text{cl}}(z, z). \quad (7.63)
 \end{aligned}$$

The former diagram is equal to diagram A in the quantum theory (equation (7.33), after a spatial Fourier transform) if $F_{\text{cl}}(x_1, x_2)$ equals the F two point function in equation (7.24).

Both diagrams (7.62) and (7.63) can be divergent, depending on F_{cl} . If the divergences are local they can be canceled by adding counterterms. In fact diagram (7.63) contains a tadpole diagram, which is automatically local and can be canceled completely by a linear counterterm.

Similarly one can construct the contribution $\langle \phi_0(x_1)\phi_2(x_2) \rangle_{\text{cl}}$, which is equal to the mirror version of diagram A in (7.33). Finally there is $\langle \phi_1(x_1)\phi_1(x_2) \rangle_{\text{cl}}$, which is equal to diagram B in the quantum theory. It is not possible to obtain diagram C in the classical theory.

Note that the resulting classical diagrams can have loops. This illustrates that loop corrections occur not only in the quantum theory, but also in the classical theory. These diagrams do not vanish, because there are statistical fluctuations.

7.4 CLASSICAL APPROXIMATION

In section 7.2 we have investigated the late time behaviour of the quantum theory, and in section 7.3 we have set up the classical theory. The graphical representation of the classical perturbative corrections as described in section 7.3.2 suggests that the classical theory reproduces exactly the diagrams of the quantum theory with only vertices with one dashed line. In Appendix D a precise argument is given that shows that this is indeed the case. Hence if we choose the initial conditions of the classical approximation such

that the classical free field two point function F_{cl} is equal to the quantum F two point function (7.24), the classical approximation reproduces the contributions of the quantum theory coming from these diagrams.

In the one loop correction to the two point function (7.33), this means that the classical approximation is given by diagrams A, B and D (counterterms are still necessary in the classical approximation).

In this section we investigate how good the classical theory is as a classical approximation to the quantum theory for late times.

7.4.1 SMALL INTERNAL MOMENTA

As argued in section 7.2.2 for small internal momenta, the diagrams with only vertices with one dashed line give exactly the contributions in the quantum theory that are proportional to τ^0 . The other diagrams, that have vertices with three dashed lines and are not in the classical approximation, give contributions that are suppressed by $|k\tau_H|^6 = \exp(-6N_H)$, because each vertex with three dashed lines leads to two more retarded propagators compared to a vertex with one dashed line. These contributions do not grow after horizon exit. Therefore, for small internal momenta the classical approximation is good up to errors that are suppressed by a factor of $\exp(-6N_H)$ with respect to the late time contributions.

This is confirmed in the example of the one loop correction to the two point function. Here the late time contributions from small internal momenta are completely coming from diagrams A and B and these diagrams do indeed occur in the classical approximation.

The internal momenta in tree diagrams are always small. Therefore the tree level contributions in the quantum theory can well be approximated by a classical approximation, if τ_H is chosen sufficiently long after horizon exit. Note that this is not trivial: the quantum theory contains tree diagrams with vertices with three dashed lines that do not occur in the classical approximation.

7.4.2 LARGE INTERNAL MOMENTA

In section 7.2.2 we have seen that in the quantum theory loop corrections get late time contributions from internal momenta up to the Hubble scale H , from 1PI diagrams with one external dashed line. This set of diagrams is not the same as the diagrams of the classical approximation. Namely the 1PI diagrams with one external dashed line can contain vertices with three dashed lines, but these diagrams do not occur in the classical approximation. Therefore, the classical approximation misses late time contributions from large

internal momenta. This could have been expected: the classical approximation is not supposed to be good for physics at scales around H .

For one loop corrections the classical approximation can be saved: it turns out that the classical approximation does not miss any late time contributions, because at one loop level there are no 1PI diagrams having both one external dashed line and a vertex with three dashed lines. However, another problem arises: because the classical approximation has fewer diagrams than the quantum theory, not all ultraviolet divergences are canceled. In the next subsection, we treat these new ultraviolet divergences by introducing a cutoff.

In the two point function this becomes apparent by the fact that the classical approximation does not contain diagram C. As a consequence, the ultraviolet divergence of diagram B is not canceled. As mentioned above, this ultraviolet divergence is not local, and can therefore not be canceled by a counterterm.

7.4.3 CLASSICAL APPROXIMATION AT ONE LOOP

In order to deal with the ultraviolet divergences in the classical approximation at one loop, we introduce a cutoff at a physical scale Λ (we use a physical scale and not a comoving scale, such that we can use the arguments of section 7.2.2). In the following we estimate the magnitude of the error that is induced by this cutoff in one loop diagrams.

First of all there are the ultraviolet divergences that made the cutoff necessary. From equation (7.42) we see that they are proportional to $(\Lambda/H)^{n_1}$ with $n_1 \geq 0$ (the case $n_1 = 0$ can give a factor $\ln(\Lambda/H)$). As argued above, these divergences occur (at least at one loop level) only in 1PI diagrams with two or more external dashed lines, and are therefore, according to the argument in section 7.2.2, suppressed by a factor $\exp(-3N_H)$ or a positive power of this factor. Thus errors coming from the divergent terms have an extra factor of $\exp(-3N_H)(\Lambda/H)^{n_1}$ with respect to late time contributions from large internal momenta.

This can be checked for the example in Appendix E: the term of the amputated version of diagram B that causes a linear divergence in the classical approximation is given in (E.61). Together with the external G^R two point functions, the divergent term has an extra factor $|k\tau_H|^3(\Lambda/H)$ with respect to non-vanishing late time contributions, e.g. equation (E.62).

Secondly there are the errors from terms that are proportional to inverse powers of Λ and that would vanish if the cutoff would be sent to infinity. For 1PI diagrams with one external dashed line, these errors can be proportional to τ^0 and give late time contributions. These errors therefore have only an extra factor of $(H/\Lambda)^{n_2}$ with $n_2 > 0$, with respect to other late time contributions from large internal momenta.

The total error thus scales like

$$c_1 e^{-3N_H} \left(\frac{\Lambda}{H}\right)^{n_1} + c_2 \left(\frac{H}{\Lambda}\right)^{n_2}, \quad (7.64)$$

with respect to other late time contributions, where c_i are constants of $\mathcal{O}(1)$. To make this factor considerably smaller than one, τ_H should be chosen long enough after horizon exit and the cutoff Λ should be chosen considerably larger than the Hubble scale H ; e.g. if $n_1 = n_2 = 1$ and $c_1 = c_2$, Λ should be chosen of the order of $\exp(3N_H/2)H$.

Instead of introducing the cutoff by hand in the momentum integrals, one can also remove the ultraviolet divergences by changing the ultraviolet behaviour of the initial conditions. For example one can put a cutoff in the initial conditions:

$$\int d^3x e^{-i\mathbf{k}\cdot\mathbf{x}} \langle \phi(\tau_H, \mathbf{x}) \phi(\tau_H, \mathbf{0}) \rangle_{\text{cl}} = \frac{H^2}{2k^3} (1 + k^2 \tau_H^2) \theta(\Lambda_{\text{cm}} - k), \quad (7.65)$$

where Λ_{cm} is now a cutoff in comoving momentum. The physical scale Λ that corresponds with Λ_{cm} is $|\Lambda_{\text{cm}}/a(\tau)|$, thus the error estimate (7.64) becomes now

$$c_1 e^{-3N_H} |\Lambda_{\text{cm}} \tau|^{n_1} + c_2 \left| \frac{1}{\Lambda_{\text{cm}} \tau} \right|^{n_2}. \quad (7.66)$$

Another possibility is to choose initial conditions as

$$\int d^3x e^{-i\mathbf{k}\cdot\mathbf{x}} \langle \phi(\tau_H, \mathbf{x}) \phi(\tau_H, \mathbf{0}) \rangle_{\text{cl}} = \frac{H^2}{2k^3} \frac{1 + k^2 \tau_H^2}{1 + k^2 \tau_c^2}, \quad (7.67)$$

where there is not a hard cutoff, but the loop diagrams are made finite (except for the tadpole diagram, which does not cause problems because it can be canceled by a local counterterm). The time τ_c acts like an inverse (soft) cutoff in comoving momenta, so that it should be taken small enough to make $\tau/\tau_c \gg 1$ and large enough to keep $|k\tau_H|^3 (\tau/\tau_c)^n$ small.

7.4.4 EXAMPLE

In Appendix E we have calculated the one loop correction to the two point function in the quantum theory. As an example, we have computed numerically the error that comes from using a finite cutoff for a specific set of parameters, as a function of the cutoff. This is done for diagram A by taking the upper limit in equation (E.31), adding the counterterm (diagram D), and subtracting the term that remains finite in the limit $\Lambda \rightarrow \infty$ (i.e. the second line of (E.42)). Then the external lines are attached and the times τ_1 and τ_2 are integrated numerically. For diagram B the upper limit in equation (E.60) is used, and there are no counterterms. The results are divided by the full correction (7.45), and are

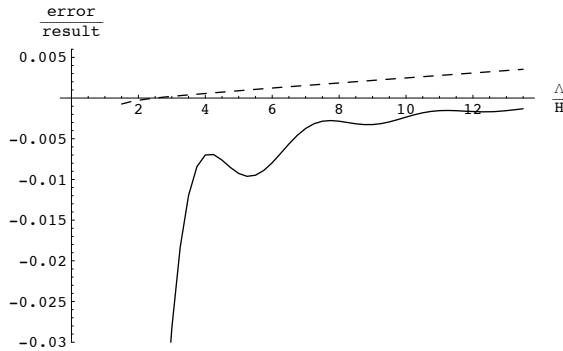


Figure 7.1: Plot of the numerically calculated error with respect to the complete result (7.45), for diagrams A and D (full line) and diagram B (dashed line), versus the cutoff Λ/H . We have used $k\tau_H = -0.4$, $k\tau = -0.03$, $\delta = 0.1$, and $2\mu = H$.

plotted, separately for diagrams A and D, and for diagram B, in figure 7.1. Both errors are much smaller than the full correction (7.45). The error from diagrams A and D is clearly decreasing for increasing cutoff. The error from diagram B is suppressed, but increasing linearly with the cutoff. These results agree with the arguments given in this section.

7.5 DISCUSSION AND CONCLUSIONS

7.5.1 EARLY TIME CONTRIBUTIONS

Both in the quantum theory and in the classical theory we have neglected early time contributions, i.e. contributions from times before τ_H . In both cases they can be included by imposing initial conditions at τ_H , which can be obtained by calculating equal time correlation functions at τ_H in the quantum theory with initial time $\tau_{\text{in}} \rightarrow -\infty$.

In the quantum theory the initial conditions can be represented by non-local n -point vertex functions that act only at the initial time τ_H , as explained for example in [156]. These vertex functions can have any number of dashed and full lines. They can give by themselves constant late time contributions, and can also occur in diagrams that give growing late time contributions. These extra ingredients make the arguments and calculations more complicated, but do not change them qualitatively. For example the calculation of the one loop correction to the two point function in Appendix E will have extra contributions from early times, of order λ^2 but without growing factors $\ln(\tau/\tau_H)$.

In the classical theory a similar thing can be done. A practical problem is that not all the vertex functions can be represented in the classical theory, because they can have

any number of dashed lines, while in the classical theory only vertices with one dashed line can be represented. Instead the initial conditions at τ_H can be imposed by adjusting the free field correlation functions. They are then in general non-Gaussian and cannot be represented only by the free field two point function (7.56). As a consequence, the calculations become more complicated, but not qualitatively different, as is the case in the quantum theory.

7.5.2 GENERALIZATION TO DERIVATIVE INTERACTIONS

Throughout this chapter we have used ϕ^3 theory as a toy model. For other interactions the analysis of this chapter can be adjusted, which is straightforward for ϕ^n interactions, but less so for derivative interactions, which are of particular interest for cosmology.

Let us first consider contributions from small internal momenta. A spatial derivative leads to an inverse power of the scale factor, or equivalently to a factor of τ . As can be seen from the power counting argument in section 7.2.2, this extra factor of τ suppresses late time contributions and prevents that any factors of $\ln(\tau/\tau_H)$ occur.

For a temporal derivative the situation is more complicated. If a time derivative $\partial_{t_1} = -H\tau_1\partial_{\tau_1}$ acts on an F two point function, which can be expanded as (7.37), the constant term vanishes, so the result is proportional to τ_i^2 and as a consequence, late time contributions are suppressed. But if a time derivative acts on a G^R two point function, which can be expanded as (7.38), the result is still proportional to τ_i^3 , and there is no suppression of late time contributions yet. Only when there is also a time derivative acting on the other time argument ∂_{t_2} , the result becomes proportional to τ_i^5 and late time contributions are suppressed.

Hence when an interaction has one time derivative, e.g. $\dot{\phi}\phi^2$, there are still late time contributions: if at all vertices (with one dashed line) the time derivatives act at the dashed line, no extra factors of τ_i appear and late time contributions are not suppressed. But when an interaction has two time derivatives, e.g. $\dot{\phi}^2\phi$, there is no way to avoid suppression of the late time contributions: in a diagram with N vertices (all of this type and with one dashed line), there are N G^R two point functions and $2N$ time derivatives, so that there must be at least one G^R two point function with time derivatives on both sides, or an F two point function with a time derivative.

For large internal momenta, we can reconsider the power counting argument in section 7.2.2. A derivative (spatial or temporal) leads in (7.42) to either an additional factor $p\tau$, or to no additional factors. Hence derivatives only change the value of the integer l , and do not change the arguments of section 7.2.2. Apparently late time contributions from large internal momenta are not necessarily suppressed by derivative interactions.

In [102] these matters are treated in a slightly different way. There the time integrals are

performed first, and after that the momentum integrals, which is a different order than employed in this chapter. For fixed external and internal momenta, a theorem is derived that shows that if the interactions obey certain conditions, the time integrals converge for $\tau \rightarrow 0$. For the wavefunctions an asymptotic expansion is used, which is valid for late times (or equivalently small momenta).

Because in this theorem $\tau \rightarrow 0$ is taken, relative to which all fixed momenta are small, and because of the use of the asymptotic expansion, this theorem can be compared with our findings above for small internal momenta. They are indeed in agreement with the conditions of the theorem.

7.5.3 COMPARISON TO STOCHASTIC APPROACH

It is interesting to compare the classical theory as described in section 7.3, to the stochastic approach [124, 125]. In this approach the field ϕ is also considered to be a classical field with statistical fluctuations after horizon exit. The difference with the classical theory of section 7.3 is that the fluctuations are not imposed as initial conditions at a fixed initial time, but are put into the system stochastically at wavenumber H at all times.

The stochastic approach has in the recent literature been used for different purposes, e.g. for calculating non-Gaussianities perturbatively in multifield inflation [126, 127, 128, 129], and for investigating nonperturbative behaviour in de Sitter space that occurs at very late times [125, 130, 131, 132] when the factors $\ln(-\tau)$ have grown so large that they overcome the suppression by small coupling constants. In the latter case it has been argued [130, 131, 132] that the stochastic approach can reproduce the terms with the largest power of $\ln(-\tau)$ at each order in the coupling constant (leading log approximation).

Below we first discuss the case of only a massless minimally coupled scalar field with nonderivative interactions, as in section 7.3. Then we make some remarks on theories with derivative interactions and with other fields than massless minimally coupled scalars.

MASSLESS MINIMALLY COUPLED SCALAR WITH NONDERIVATIVE INTERACTIONS

The stochastic approach mostly does not use a mass as infrared regulator, but a finite lower limit for the momentum integrals: the classical field ϕ is defined to contain only modes with comoving wavenumber $k > H$. Physically this corresponds to considering only a finite patch of de Sitter space, the size of which increases exponentially by the expansion. So to compare with the classical theory of section 7.3, we need to reformulate the latter using this infrared regulator.

Apart from the different infrared regulator, the stochastic approach makes two additional approximations with respect to the classical theory of section 7.3. First the classical field

is assumed not to contain modes with wavenumber $k > Ha$; hence the momentum integrals have an upper limit Ha . Second, the wavefunction of the free scalar field (B.4), that is used to characterize the stochastic fluctuations, is approximated by its leading term for late times: $\phi_{k,1}(\tau) \rightarrow i \frac{H}{\sqrt{2k^3}}$. In the classical theory of section 7.3 this is equivalent to taking only the leading term of the expansion of the F two point function, as is done in equation (7.37). Also the retarded propagator G^R is approximated by its leading term, as in equation (7.38).

We now compare the stochastic approach with the classical theory of section 7.3 for the one loop correction of the two point function in ϕ^3 theory, in particular the term with the largest power of $\ln(-\tau)$. For the classical theory we can use the calculation in Appendix E; we only adjust the infrared regulator. This means that in the calculations for small internal momenta we put $\delta \rightarrow 0$, and use a lower limit H for the momentum integrals. For diagram A this changes equation (E.11) to

$$\frac{i\lambda^2\theta(\tau_1 - \tau_2)}{6(2\pi)^2 H^4 (\tau_1 \tau_2)^4} \left(2(\tau_1^3 - \tau_2^3) \ln \frac{M_{\text{cm}}}{H} \right). \quad (7.68)$$

The calculation for large internal momenta is unchanged and gives a finite contribution after adding the counterterm of diagram D. Attaching the external lines and performing the time integrals gives for the term with the largest power of $\ln(-\tau)$

$$\frac{\lambda^2}{36(2\pi)^2 k^3} \left\{ -\frac{1}{3} \ln^3 \frac{\tau}{\tau_H} \right\}. \quad (7.69)$$

For the small internal momenta of diagram B we use the integral

$$\int_H^{M_{\text{cm}}} \frac{dp}{p^2} \int_{|p-k|}^{p+k} \frac{dp'}{p'^2} = \frac{1}{k^2} \left(\ln \frac{k^2}{H^2} + \ln \frac{M_{\text{cm}} - k}{M_{\text{cm}} + k} + \frac{2k}{M_{\text{cm}}} - 2 \right), \quad (7.70)$$

so that the analog of (E.58) becomes

$$\frac{-\lambda^2}{4(2\pi)^2 k^3 H^4 (\tau_1 \tau_2)^4} \left(\ln \frac{k^2}{H^2} + \ln \frac{M_{\text{cm}} - k}{M_{\text{cm}} + k} + \frac{2k}{M_{\text{cm}}} - 2 \right). \quad (7.71)$$

Again the integral for the large internal momenta remains unchanged (we use a cutoff as described in section 7.4.3), and attaching the external lines and performing the time integrals gives a leading logarithmic term of $\ln^2(\tau/\tau_H)$. Apparently there is no contribution to the $\ln^3(\tau/\tau_H)$ term from diagram B when we use this infrared regularization.

We can calculate the same quantity in the stochastic approach by using stochastic sources. However we will not do this, but instead repeat the calculation of above, using the additional assumptions of the stochastic approach (i.e. taking the leading order approximations for the propagators (7.37), (7.38), and the upper limit $k < Ha$ in the momentum integral). We expect that this does not make a difference for the result of the largest

power of $\ln(-\tau)$ and therefore we interpret the result of this calculation as the result of the stochastic approach.

With the approximations of the stochastic approach, the calculation of diagram A reduces to the calculation for small internal momenta done above, with only the upper limit changed from M_{cm} to $Ha(\tau_2)$. For the amputated version of diagram A the result is then

$$\frac{i\lambda^2\theta(\tau_1 - \tau_2)}{6(2\pi)^2 H^4(\tau_1\tau_2)^4} \left(2(\tau_1^3 - \tau_2^3) \ln \frac{-1}{H\tau_2} \right), \quad (7.72)$$

and after attaching the external lines and performing the time integrals, the result for the largest power of $\ln(-\tau)$ is the same as in our formulation of the classical theory, (7.69). For the amputated version of diagram B the result is

$$\frac{-\lambda^2}{4(2\pi)^2 k^3 H^4(\tau_1\tau_2)^4} \left(\ln \frac{k^2}{H^2} + \ln \frac{Ha(\tau_2) - k}{Ha(\tau_2) + k} + \frac{2k}{Ha(\tau_2)} - 2 \right), \quad (7.73)$$

which, similarly to the contribution (7.71) for our formulation of the classical theory, does not lead to $\ln^3(\tau/\tau_H)$ terms.

In this calculation the stochastic approach reproduces the same leading logarithmic term (but not the same subleading logarithmic terms) as the classical theory in our formulation, using a lower momentum limit as infrared regulator. We remark that if we would have split the momentum integrals at a physical scale $M_{\text{cm}}a$ instead of the comoving scale M_{cm} in the calculation of the classical theory, *all* the contributions to the leading logarithmic term would have come from small internal momenta. It is reasonable to expect that this remains true for higher orders. Moreover the approximations for the propagators in the stochastic approach are then also the same as we made in the calculation for the small internal momenta. Therefore we expect that the stochastic approach will give the largest logarithmic term at each order in the coupling, consistent with the arguments in [130, 131, 132].

Because of the used approximations, the stochastic approach has fewer problems with the ultraviolet than our formulation of the classical theory (see sections 7.4.2 and 7.4.3). The drawback of using these approximations is that even at one loop order, only the leading logarithmic term can be obtained, whereas in our formulation of the classical theory, also the subleading logarithmic terms can be obtained at one loop order, as explained in section 7.4.3.

DERIVATIVE INTERACTIONS AND OTHER FIELDS

As argued in section 7.5.2, derivative interactions typically lead to positive powers of τ and therefore to suppression of late time contributions from small internal momenta. There can also be interactions with fields that are not massless minimally coupled scalar

fields. The wavefunctions of these fields are proportional to a positive power of τ for late times, instead of to τ^0 , as is the case for massless minimally coupled scalar fields. Therefore the leading terms of the expansions of the F two point functions of these fields are also proportional to a positive power of τ . If a diagram contains such an F two point function, this diagram cannot lead to late time contributions from small internal momenta.

However, even if there are no late time contributions from small internal momenta, it is still possible that there are late time contributions from large internal momenta. The stochastic approach makes approximations that are not valid for large internal momenta. Therefore one expects the stochastic approach to have problems with reproducing the late time contributions for this case. These problems can be circumvented for corrections that come from a massless fermion [183] or from a photon [132], by integrating out the fermion or photon and considering the resulting effective theory of the scalar field.

7.5.4 APPLICATION TO THE CURVATURE PERTURBATION

The motivation for this work comes from cosmological perturbations generated during a period of inflation. As mentioned in the introduction, a suitable parameterization for these cosmological perturbations is the curvature perturbation ζ , which typically has interactions involving derivatives. It is of interest to know late time contributions of correlation functions of ζ , and whether these can be approximated by a classical approximation.

For small internal momenta, one can derive the interaction terms for the various degrees of freedom in a specific model of inflation, and then use the conditions of the theorem of [102] to decide whether these interactions can lead to late time contributions. For single field inflation (possibly together with \mathcal{N} free massless scalar fields) it is shown in [102] that the interactions do obey the conditions, and therefore do not give late time contributions to all orders. This can be compared with [118], where it is argued, using classical physics, that ζ is conserved after horizon exit. This argument is only valid for adiabatic perturbations which applies to single field inflation and for small internal momenta because the large internal momenta are removed by a smoothing procedure. Indeed we found in section 7.4.1 that for small internal momenta the quantum theory can be approximated quite well by classical physics.

For inflation models involving more fields, there are typically interactions that do not obey the conditions of the theorem in [102], and therefore can lead to late time contributions. Correspondingly, the perturbations are not adiabatic in these models, hence the argument of [118] does not apply and it is no surprise that ζ is not conserved after horizon exit.

For large internal momenta the situation is different. Since derivatives do not necessarily suppress late time contributions, it is possible that loop corrections lead to late time contributions, even for single field inflation. Moreover, a classical approximation would

only be able to approximate these contributions up to one loop. An explicit calculation should decide on whether these contributions occur or not. The sample calculation in [102] seems to indicate that there are no late time contributions, even for large internal momenta, but we are concerned about the fact that in this calculation $\tau \rightarrow 0$ is taken before the momentum integrals are performed. The terms that are discarded in this way might lead to late time contributions.

Note that the background spacetime in inflation is not exactly de Sitter, but typically has a slowly decreasing Hubble constant H . This time dependence should be taken into account when deriving the wavefunctions for the fluctuating fields, and when doing the time integrals. Moreover, the fluctuations can react back on this background and in this way change the time dependence of H . This backreaction can be calculated by considering one point functions of the fluctuating fields, as is done for example in [184, 104, 105].

7.5.5 CONCLUSIONS

We have investigated up to which order corrections to cosmological correlation functions, generated after horizon exit, can be calculated reliably using classical physics. We have done this by making a detailed study of ϕ^3 theory on a de Sitter background, for a massless minimally coupled scalar field ϕ as a toy model.

In the quantum theory we studied late time contributions (generated after horizon exit) to equal time correlation functions with external momenta much smaller than the Hubble scale. We found that in loop corrections the loop integrals get contributions from internal momenta up to the Hubble scale H . This is different from the intuition from effective field theories in flat space that loop integrals are dominated by internal momenta of the same order of magnitude as the external momenta. Our calculation of the one loop correction to the two point function supports the argument that the contributions from large internal momenta (around scale H) are not negligible: they are proportional to $\lambda^2 \ln^3(\tau/\tau_H)$, whereas the contributions from the small internal momenta are also proportional to $\lambda^2 \ln^3(\tau/\tau_H)$, or to $\lambda^2 \ln^2(\tau/\tau_H)/\delta$, with $\delta = m^2/3H^2$.

Furthermore we found that a classical approximation can approximate contributions from small internal momenta quite well, but that this does not hold for contributions from large internal momenta. This is not surprising, because the classical approximation is only supposed to work for physics at momentum scales much below the Hubble scale H . As a consequence, the classical approximation is good at tree level, but in general not for loop corrections. An exception is the one loop correction, for which the classical approximation can be good if an ultraviolet cutoff $\Lambda > H$ is introduced.

We argued that the results presented for the ϕ^3 toy model can be extended to derivative interactions, and be applied to the curvature perturbation ζ . For non-Gaussian effects in

multifield inflation models this means that at leading order, which is tree level, can be approximated quite well using classical physics. Also the one loop corrections can be approximated if a suitable cutoff is chosen. But for higher order corrections, the classical approximation is not expected to reproduce all late time contributions.

For small internal momenta, we found that derivatives tend to suppress late time corrections, in a way that agrees with the theorem derived by Weinberg [102]. However, for large internal momenta late time contributions need not be suppressed. Consequently, it is possible that the curvature perturbation ζ is not conserved to all orders after horizon exit, even for single field inflation. There might be contributions to correlation functions of ζ that grow after horizon exit, coming from loop corrections. These contributions would be suppressed by powers of the coupling constant H/M_{pl} and possibly also by slow-roll parameters, but they would be amplified by powers of the number of e-folds $\ln a$.

CHAPTER 8

CONCLUSIONS

Currently the evolution of cosmological correlations after horizon exit is calculated using classical physics, which is expected to be a good approximation. Yet there are reasons to study quantum corrections to cosmological correlations. First it is important to estimate the size of the quantum corrections, and to check if the approximation is indeed good. Second there is a more fundamental reason: we should check if we understand quantum field theory well enough to be able to do these calculations and if it behaves as we expect it to behave, or quoting [102], we “ought to know what our theories entail”.

In this context we studied in chapter 7 a toy model of ϕ^3 theory on an exact de Sitter background. We formulated the CTP formalism of quantum field theory in a suitable way, and derived the corresponding diagrammatic expansion. Next we derived which terms contain contributions that grow after horizon exit (late time contributions).

In our classical theory with statistical fluctuations, all the late time contributions of the quantum theory at tree level can be reproduced exactly. Those at one loop level can be reproduced approximately, by using suitable initial conditions and a carefully chosen ultraviolet cutoff. The classical methods discussed in section 6.2.3 can have errors at this order: the stochastic approach usually has an ultraviolet cutoff that is smaller than the Hubble scale H , and the δN formalism uses smoothing which also leads to errors.

From two loop level on, there can be late time contributions in the quantum theory from large internal momenta that cannot be reproduced by a classical theory.

It would be interesting to extend this work by applying this method to the curvature perturbation ζ , which has (much) more complicated interactions than the toy model. The arguments [116, 118] that show that ζ is conserved to all orders outside the horizon use a smoothing assumption. It is possible that without this assumption, ζ is not conserved

anymore to all orders.

APPENDIX A

CONVENTIONS

We use a metric $g_{\mu\nu}$ with signature $-+++$.

For the γ matrices we use the representation

$$\gamma^0 = -i \begin{pmatrix} 0 & 1 \\ 1 & 0 \end{pmatrix}, \quad \gamma^i = -i \begin{pmatrix} 0 & \tau^i \\ -\tau^i & 0 \end{pmatrix}, \quad (\text{A.1})$$

where the τ^i are the Pauli matrices, and which satisfies $\{\gamma^\mu, \gamma^\nu\} = 2g^{\mu\nu}$. Furthermore we have

$$\bar{\psi} = \psi^\dagger \beta, \quad (\text{A.2})$$

with

$$\beta = i\gamma_0, \quad \beta^2 = 1, \quad \beta\gamma^\mu\beta = -\gamma^{\mu\dagger}, \quad (\text{A.3})$$

and

$$\mathcal{C} = \gamma_2\beta, \quad \mathcal{C}^\dagger = \mathcal{C}^{-1} = \mathcal{C}^T = -\mathcal{C} \quad \mathcal{C}\gamma^\mu\mathcal{C}^{-1} = -\gamma^{\mu T}. \quad (\text{A.4})$$

We define

$$\gamma_5 = i\gamma^0\gamma^1\gamma^2\gamma^3, \quad \gamma_5^\dagger = \gamma_5, \quad \gamma_5^2 = 1, \quad \{\gamma^\mu, \gamma_5\} = 0. \quad (\text{A.5})$$

The γ_5 matrices are used in the projectors $P_{L,R}$:

$$P_L = \frac{1}{2}(1 - \gamma_5), \quad P_R = \frac{1}{2}(1 + \gamma_5), \quad (\text{A.6})$$

and obey

$$P_{L,R}\gamma^\mu = \gamma^\mu P_{R,L}, \quad \beta P_{L,R}\beta = P_{R,L}, \quad \mathcal{C}P_{L,R}\mathcal{C}^{-1} = P_{L,R}^T. \quad (\text{A.7})$$

APPENDIX B

FREE SCALAR FIELD ON A DE SITTER BACKGROUND

B.1 SCALAR WAVEFUNCTION

The free field equation of motion for a scalar field on a de Sitter background is

$$\partial_\tau^2 \phi(x) + 2Ha(\tau)\partial_\tau \phi(x) - \nabla^2 \phi(x) + a^2(\tau)(m^2 + \xi R)\phi(x) = 0, \quad (\text{B.1})$$

where we use $x = (\tau, \mathbf{x})$ with τ conformal time. After a spatial Fourier transformation the solutions for the mode functions are (see e.g. [114])

$$\phi_{k,\alpha}(\tau) = -\frac{\sqrt{-\pi\tau}}{2a(\tau)} H_\nu^{(\alpha)}(-k\tau), \quad (\text{B.2})$$

where $H_\nu^{(\alpha)}(-k\tau)$ are the Hankel functions for $\alpha = 1, 2$, and where ν is determined by

$$\nu^2 = \frac{9}{4} - \frac{m^2}{H^2} - 12\xi. \quad (\text{B.3})$$

For massless minimally coupled fields, $m = 0$, $\xi = 0$ and thus $\nu = 3/2$ (we choose ν to be positive). Then the modefunctions reduce to

$$\phi_{k,1}(\tau) = i \frac{H}{\sqrt{2k^3}} (1 + ik\tau) e^{-ik\tau} \quad (\text{B.4})$$

and $\phi_{k,2}(\tau) = \phi_{k,1}^*(\tau)$. For $k\tau \rightarrow -\infty$ the $\phi_{k,1}(\tau)$ mode function is proportional to $e^{-ik\tau}/a(\tau)$ and is called the positive frequency solution¹. Using these mode functions,

¹Often the Hankel functions are used with a negative argument: $H_\nu^{(\alpha)}(k\tau)$. Then the $\phi_{k,2}(\tau)$ mode function is the positive frequency solution.

the scalar field operator can be decomposed as

$$\phi(\tau, \mathbf{x}) = \int \frac{d^3k}{(2\pi)^3} \left(e^{i\mathbf{k}\cdot\mathbf{x}} \alpha_{\mathbf{k}} \phi_{k,1}(\tau) + e^{-i\mathbf{k}\cdot\mathbf{x}} \alpha_{\mathbf{k}}^\dagger \phi_{k,1}^*(\tau) \right), \quad (\text{B.5})$$

where the annihilation operators $\alpha_{\mathbf{k}}$ and creation operators $\alpha_{\mathbf{k}}^\dagger$ satisfy the commutation relations

$$[\alpha_{\mathbf{k}}, \alpha_{\mathbf{k}'}^\dagger] = (2\pi)^3 \delta^3(\mathbf{k} - \mathbf{k}'), \quad [\alpha_{\mathbf{k}}, \alpha_{\mathbf{k}'}] = 0. \quad (\text{B.6})$$

The normalizations are chosen such that

$$[\phi(\tau, \mathbf{x}), \pi(\tau, \mathbf{x}')] = i\delta^3(\mathbf{x} - \mathbf{x}'), \quad (\text{B.7})$$

where $\pi(\tau, \mathbf{x}) = a^2(\tau)\partial_\tau\phi(\tau, \mathbf{x})$ is the conjugate momentum, and that $a(\tau)\phi(\tau, \mathbf{x})$ is a conventionally normalized free field for $k\tau \rightarrow -\infty$. The state $|0\rangle$ defined by

$$\alpha_{\mathbf{k}}|0\rangle = 0 \quad (\text{B.8})$$

corresponds therefore with the free vacuum state in Minkowski spacetime for $k\tau \rightarrow -\infty$. This state is called adiabatic or Bunch-Davies vacuum and is the state with respect to which we calculate correlation functions in this paper.

B.2 PARTICLE CREATION

Despite the confusing nature of the concept of particle number in curved spacetime (see e.g. [114]), we give here a definition of the particle number in the frame of a comoving observer in de Sitter spacetime. This definition of particle number then allows us to make a comparison with the classical approximation in thermal field theory in the next section.

Using comoving time, the free Lagrangian is the spatial integral over the Lagrangian density (7.1) with $\lambda = 0$

$$L[\varphi_{\mathbf{k}}, \partial_\tau\varphi_{\mathbf{k}}] = \int \frac{d^3k}{(2\pi)^3} \left(\frac{1}{2}a^2|\partial_\tau\varphi_{\mathbf{k}}|^2 - \frac{1}{2}a^2k^2|\varphi_{\mathbf{k}}|^2 - \frac{1}{2}(m^2 + \xi R)a^4|\varphi_{\mathbf{k}}|^2 \right), \quad (\text{B.9})$$

where we have taken

$$\phi(\tau, \mathbf{x}) = \int \frac{d^3k}{(2\pi)^3} \varphi_{\mathbf{k}} e^{i\mathbf{k}\cdot\mathbf{x}}, \quad (\text{B.10})$$

where the $\varphi_{\mathbf{k}}$ are time dependent operators. In this form the Lagrangian describes a system of uncoupled harmonic oscillators with frequencies $\omega_k = \sqrt{k^2 + a^2(m^2 + \xi R)}$. The conjugate momentum is defined as $\pi_{\mathbf{k}} = \delta L/\delta(\partial_\tau\varphi_{\mathbf{k}}) = a^2\partial_\tau\varphi_{\mathbf{k}}$, and using this the Hamiltonian becomes

$$H[\varphi_{\mathbf{k}}, \pi_{\mathbf{k}}] = \int \frac{d^3k}{(2\pi)^3} \left(\frac{1}{2} \frac{|\pi_{\mathbf{k}}|^2}{a^2} + \frac{1}{2} a^2 k^2 |\varphi_{\mathbf{k}}|^2 + \frac{1}{2} (m^2 + \xi R) a^4 |\varphi_{\mathbf{k}}|^2 \right). \quad (\text{B.11})$$

By analogy to the harmonic oscillator, we define *time dependent* annihilation and creation operators $\bar{\alpha}_{\mathbf{k}}$ and $\bar{\alpha}_{\mathbf{k}}^\dagger$ by

$$a\varphi_{\mathbf{k}} = \frac{1}{\sqrt{2\omega_k}} \left(\bar{\alpha}_{\mathbf{k}} e^{-ik\tau} + \bar{\alpha}_{-\mathbf{k}}^\dagger e^{ik\tau} \right), \quad \frac{\pi_{\mathbf{k}}}{a} = \frac{1}{i} \sqrt{\frac{\omega_k}{2}} \left(\bar{\alpha}_{\mathbf{k}} e^{-ik\tau} - \bar{\alpha}_{-\mathbf{k}}^\dagger e^{ik\tau} \right). \quad (\text{B.12})$$

They obey the commutation relation

$$[\bar{\alpha}_{\mathbf{k}}, \bar{\alpha}_{\mathbf{k}'}^\dagger] = (2\pi)^3 \delta^3(\mathbf{k} - \mathbf{k}'). \quad (\text{B.13})$$

The Hamiltonian (B.11) expressed in terms of these operators has the familiar form

$$H = \int \frac{d^3k}{(2\pi)^3} \left(\bar{\alpha}_{\mathbf{k}}^\dagger \bar{\alpha}_{\mathbf{k}} + \frac{1}{2} [\bar{\alpha}_{\mathbf{k}}, \bar{\alpha}_{\mathbf{k}}^\dagger] \right) \omega_k. \quad (\text{B.14})$$

If we take $m = 0$ and $\xi = 0$ we can use the modefunction $\phi_{k,1}(\tau)$ of equation (B.4) to express the operators $\bar{\alpha}_{\mathbf{k}}, \bar{\alpha}_{\mathbf{k}}^\dagger$ in terms of the operators $\alpha_{\mathbf{k}}, \alpha_{\mathbf{k}}^\dagger$ in the mode decomposition (B.5):

$$\bar{\alpha}_{\mathbf{k}} = \frac{-i}{2k\tau} (1 + 2ik\tau) \alpha_{\mathbf{k}} + i \frac{e^{2ik\tau}}{2k\tau} \alpha_{-\mathbf{k}}^\dagger, \quad (\text{B.15})$$

$$\bar{\alpha}_{-\mathbf{k}}^\dagger = \frac{-ie^{-2ik\tau}}{2k\tau} \alpha_{\mathbf{k}} + \frac{i}{2k\tau} (1 - 2ik\tau) \alpha_{-\mathbf{k}}^\dagger. \quad (\text{B.16})$$

For $k\tau \rightarrow -\infty$ the $\bar{\alpha}_{\mathbf{k}}$ operator becomes equal to $\alpha_{\mathbf{k}}$. We can define n_k and \tilde{n}_k by

$$\langle 0 | \bar{\alpha}_{\mathbf{k}}^\dagger \bar{\alpha}_{\mathbf{k}'} | 0 \rangle = n_k (2\pi)^3 \delta^3(\mathbf{k} - \mathbf{k}'), \quad n_k = \frac{1}{4k^2\tau^2} \quad (\text{B.17})$$

$$\langle 0 | \bar{\alpha}_{\mathbf{k}} \bar{\alpha}_{-\mathbf{k}'} | 0 \rangle = e^{2ik\tau} (\tilde{n}_k + \frac{i}{2k\tau}) (2\pi)^3 \delta^3(\mathbf{k} - \mathbf{k}'), \quad \tilde{n}_k = \frac{1}{4k^2\tau^2} \quad (\text{B.18})$$

where one can interpret n_k as the particle number and \tilde{n}_k as a kind of off-diagonal particle number, with respect to the vacuum at $k\tau \rightarrow -\infty$. Clearly these quantities are proportional to a^2 .

B.3 COMPARISON WITH THERMAL FIELD THEORY

It is interesting to compare with thermal field theory on a Minkowski background (see [182, 178]). The F two point function in a thermal system with temperature T in Minkowski spacetime is given by

$$F(k, t_1, t_2) = \frac{1}{k} \left(n_{\text{th}}(k) + \frac{1}{2} \right) \cos k(t_1 - t_2) \quad n_{\text{th}}(k) = \frac{1}{e^{k/T} - 1}, \quad (\text{B.19})$$

where $n_{\text{th}}(k)$ is the particle number. For small momenta with respect to the temperature $k \ll T$, $n_{\text{th}} \simeq T/k$, which becomes large and classical behaviour emerges. Moreover the G^R two point function does not have this amplification factor; it is given by

$$G^R(k, t_1, t_2) = \frac{\theta(t_1 - t_2)}{k} \sin k(t_1 - t_2). \quad (\text{B.20})$$

Therefore a diagram containing a vertex with more than one dashed line is suppressed with respect to the same diagram with a vertex with one dashed line.

To compare this with the de Sitter case, it is natural to consider $a\phi_k(\tau)$. Then we have

$$a(\tau_1)a(\tau_2)F(k, \tau_1, \tau_2) = \frac{1}{k} \left[\left(\frac{1}{2k^2\tau_1\tau_2} + \frac{1}{2} \right) \cos k(\tau_1 - \tau_2) + \frac{\tau_1 - \tau_2}{2k\tau_1\tau_2} \sin k(\tau_1 - \tau_2) \right]. \quad (\text{B.21})$$

We see that for equal times $\tau_1 = \tau_2 = \tau$ this quantity grows as

$$\frac{1}{2k^2\tau^2} + \frac{1}{2} \propto n + \tilde{n} + \frac{1}{2}. \quad (\text{B.22})$$

The quantity $a(\tau_1)a(\tau_2)G^R(k, \tau_1, \tau_2)$ does not have this amplification factor for late times, as can be seen from expansion for small $k\tau$. Therefore a diagram containing a vertex with more than one dashed line is suppressed with respect to the same diagram with a vertex with one dashed line, as in thermal field theory.

Both in the de Sitter case as in thermal field theory, the arguments given above explain why the classical approximation is good for small physical internal momenta, i.e. $k/a \ll H$ ($|k\tau| \ll 1$) or $k \ll T$. But, as we argue in this paper for the de Sitter case, for large internal momenta ($\approx H$ or $\approx T$) problems arise for the classical approximation (compare with Hard Thermal Loops [185] in thermal field theory).

APPENDIX C

AMPUTATED DIAGRAMS WITH NO EXTERNAL DASHED LINES

The contribution of an amputated diagram with no external dashed lines, as for example occurs in diagram (7.34), vanishes. The reason is that in such a diagram there is always a closed loop of G^R two point functions. This can be seen by picking an arbitrary vertex, and from there following one of the dashed lines along a G^R two point function to another vertex. From this new vertex one can repeat this to go to the next vertex. Because there are no external dashed lines, this can be repeated indefinitely while staying inside the diagram. Since there is only a finite number of vertices in the diagram, one eventually ends up at a vertex for the second time. Therefore there must be a closed loop of G^R two point functions in a diagram with no external dashed lines.

Because of the θ -functions of the G^R two point functions, the times of the vertices of a closed loop of G^R two point functions have to be ordered. But in a closed loop there is always at least one G^R two point function for which the θ -function vanishes, and therefore the complete diagram vanishes. Even if all the internal times of the loop are equal, the diagram vanishes because the G^R two point function vanishes if the time arguments are equal.

APPENDIX D

CORRESPONDENCE BETWEEN DIAGRAMS IN QUANTUM AND CLASSICAL THEORY

In this Appendix we show that, if one chooses initial conditions such that

$$F_{\text{cl}}(\mathbf{k}, \tau_1, \tau_2) = F(\mathbf{k}, \tau_1, \tau_2), \quad (\text{D.1})$$

the classical approximation reproduces the diagrams of the quantum theory with only vertices with one dashed line.

Discarding the vertex with three dashed lines in the quantum theory corresponds to discarding the term with $(\phi^{(2)})^3$ in equation (7.15). An arbitrary equal time correlation function, calculated up to order n in the coupling λ , can then be written as

$$\langle \phi(\tau, \mathbf{x}_1) \dots \phi(\tau, \mathbf{x}_r) \rangle = \langle \phi^{(1)}(\tau, \mathbf{x}_1) \dots \phi^{(1)}(\tau, \mathbf{x}_r) \frac{1}{n!} (\bar{S}_{\text{int}})^n \rangle^{(0)}, \quad (\text{D.2})$$

where the superscript (0) denotes the free correlation function, and where the modified interaction part of the action is given by

$$\bar{S}_{\text{int}} = - \int_{-\infty}^{\tau} d\tau a^4(\tau) \int d^3x \frac{\lambda}{2!} (\phi^{(1)})^2 \phi^{(2)}. \quad (\text{D.3})$$

On the right hand side of equation (D.2) the fields $\phi^{(1)}$ and $\phi^{(2)}$ have to be contracted in all possible ways: every $\phi^{(2)}$ is contracted with a $\phi^{(1)}$ to a retarded propagator G^R , and the remaining $\phi^{(1)}$'s are contracted with each other to F two point functions. Suppose

that we do have contracted the $\phi^{(2)}$'s, but not yet the remaining $\phi^{(1)}$'s. The correlation function can then be drawn as a number of disconnected diagrams, in which the vertices are connected by G^R two point functions and which have loose ends representing $\phi^{(1)}$'s that are yet to be connected. In total there are n vertices. Each disconnected diagram can be a tree diagram or a loop diagram. A loop diagram with only G^R two point functions vanishes, as explained in Appendix C. Hence if one of the disconnected diagrams contains a loop, the complete contraction does not contribute to the correlation function, and for all non-vanishing contractions the disconnected diagrams are tree diagrams. These tree diagrams are the same tree diagrams in the classical theory that represent the perturbative solutions ϕ_i in the classical theory (7.52), where all the $\phi^{(1)}$'s in the quantum theory correspond with free field solutions ϕ_0 in the classical theory. The symmetry factors are also equal because they arise in the same way (the factor $1/n!$ is canceled by a factor $n!$ from the n equivalent vertices). The remaining contractions of the $\phi^{(1)}$'s in the quantum theory are equal to the contractions of the ϕ_0 's in the classical theory, because of equation (D.1).

Therefore the classical theory with the same couplings as the quantum theory, and using initial conditions such that (D.1) holds, gives all the diagrams using only the vertex with one dashed line in the quantum theory, up to vanishing diagrams. Hence this classical theory reproduces the late time contributions for small internal momenta.

APPENDIX E

ONE LOOP CORRECTION TO TWO POINT FUNCTION

In this appendix we calculate the one loop correction to the two point function as given in equation (7.33). We first consider the diagrams with one external dashed line (diagrams A and D), and then the ones with two external dashed lines (diagrams B and C). The complete result is given in equation (7.45).

E.1 DIAGRAMS A AND D

We start with the diagrams with one external G^R two point function. First we calculate the amputated diagrams, and then attach the external lines. The amputated diagrams are:

$$\begin{array}{cc}
 \begin{array}{c} \text{A} \\ \text{---} \tau_2 \\ \text{---} \tau_1 \end{array} & \begin{array}{c} \text{D} \\ \text{---} \tau_2 \\ \text{---} \tau_1 \end{array} .
 \end{array} \quad (E.1)$$

The amputated version of diagram A is given by

$$\begin{aligned}
 A_{\text{amp}}(k, \tau_1, \tau_2) &= \frac{-i(-i\lambda)^2}{H^8 \tau_1^4 \tau_2^4} \int \frac{d^3 p d^3 p'}{(2\pi)^3} \delta^3(\mathbf{k} - \mathbf{p} - \mathbf{p}') G^R(p', \tau_1, \tau_2) F(p, \tau_1, \tau_2) = \\
 &= \frac{i\lambda^2}{(2\pi)^2 k H^8 \tau_1^4 \tau_2^4} \int_0^\infty dp p \int_{|p-k|}^{p+k} dp' p' G^R(p', \tau_1, \tau_2) F(p, \tau_1, \tau_2), \quad (E.2)
 \end{aligned}$$

where we have used the identity

$$\int d^3p d^3p' \delta^3(\mathbf{k} + \mathbf{p} + \mathbf{p}') f(k, p, p') = \frac{2\pi}{k} \int_0^\infty dp p \int_{|p-k|}^{p+k} dp' p' f(k, p, p'). \quad (\text{E.3})$$

We will evaluate this integral below. For diagram D we see from equations (7.30) and (7.3) that it is equal to

$$D_{\text{amp}}(k, \tau_1, \tau_2) = -i a^4(\tau_1) \delta_m \delta(\tau_1 - \tau_2) = \frac{-i\lambda^2}{4(2\pi)^2 H^4 \tau_1^4} \ln\left(\frac{\Lambda}{\mu}\right) \delta(\tau_1 - \tau_2), \quad (\text{E.4})$$

where Λ is the ultraviolet momentum cutoff and μ is a renormalization scale. The counterterm δ_Z is finite and leads to terms proportional to positive powers of τ , and is therefore left out.

We calculate the integral (E.2) by splitting the p integral in a small momentum part $\int_0^{M_{\text{cm}}} dp$ and a large momentum part $\int_{M_{\text{cm}}}^{\Lambda a(\tau_2)} dp$, with $|M_{\text{cm}}\tau_i| \ll 1$ and $M_{\text{cm}} > k$.¹

E.1.1 AMPUTATED DIAGRAM FOR SMALL INTERNAL MOMENTA

The integral in equation (E.2) is infrared divergent for $p \rightarrow 0$. We regulate this divergence by giving the field a small mass $m \ll H$, such that $\nu = 3/2 - \delta$ with $\delta = m^2/3H^2$. The F and G^R two point functions are then, using equations (7.17), (7.18) and (B.5),

$$F(k, \tau_1, \tau_2) = \frac{\pi\sqrt{\tau_1\tau_2}}{4a(\tau_1)a(\tau_2)} \text{Re}\left(H_\nu^{(1)}(-k\tau_1)H_\nu^{(1)*}(-k\tau_2)\right), \quad (\text{E.5})$$

$$G^R(k, \tau_1, \tau_2) = -\frac{\pi\sqrt{\tau_1\tau_2}}{2a(\tau_1)a(\tau_2)} \theta(\tau_1 - \tau_2) \text{Im}\left(H_\nu^{(1)}(-k\tau_1)H_\nu^{(1)*}(-k\tau_2)\right). \quad (\text{E.6})$$

Using (see [186])

$$H_\nu^{(1)}(-k\tau) = J_\nu(-k\tau) + i\left(\frac{\cos\nu\pi}{\sin\nu\pi} J_\nu(-k\tau) - \frac{1}{\sin\nu\pi} J_{-\nu}(-k\tau)\right), \quad (\text{E.7})$$

$$J_\nu(-k\tau) = \frac{1}{\Gamma(\nu+1)} \left(-\frac{1}{2}k\tau\right)^\nu \left(1 + \mathcal{O}(k^2\tau^2)\right), \quad (\text{E.8})$$

and the identity $\Gamma(\nu)\Gamma(1-\nu) = \pi/\sin\nu\pi$, we obtain

$$F(k, \tau_1, \tau_2) = \frac{H^2}{2k^3} (k^2\tau_1\tau_2)^\delta, \quad (\text{E.9})$$

$$G^R(k, \tau_1, \tau_2) = \theta(\tau_1 - \tau_2) \frac{H^2}{3} \left(\tau_1^3 \left(\frac{\tau_2}{\tau_1}\right)^\delta - \left(\frac{\tau_1}{\tau_2}\right)^\delta \tau_2^3\right). \quad (\text{E.10})$$

¹In [175] a similar split of integrals is used to calculate a similar integral. Note however that the integral there differs from the integral here, because the self-energy kernel of [175] is not the same as the amputated diagram A.

The integral is

$$\begin{aligned}
 & \frac{i\lambda^2}{(2\pi)^2 k H^8 \tau_1^4 \tau_2^4} \frac{H^4 \theta(\tau_1 - \tau_2) (\tau_1^3 |\tau_2|^{2\delta} - |\tau_1|^{2\delta} \tau_2^3)}{6} \int_0^{M_{\text{cm}}} dp \frac{p^{2\delta}}{p^2} \int_{|p-k|}^{p+k} dp' p' = \\
 & \frac{i\lambda^2 \theta(\tau_1 - \tau_2) (\tau_1^3 |\tau_2|^{2\delta} - |\tau_1|^{2\delta} \tau_2^3)}{6(2\pi)^2 H^4 (\tau_1 \tau_2)^4} \frac{M_{\text{cm}}^{2\delta}}{\delta} = \\
 & \frac{i\lambda^2 \theta(\tau_1 - \tau_2)}{6(2\pi)^2 H^4 (\tau_1 \tau_2)^4} \left(\frac{\tau_1^3 - \tau_2^3}{\delta} + 2\tau_1^3 \ln |M_{\text{cm}} \tau_2| - 2\tau_2^3 \ln |M_{\text{cm}} \tau_1| + \mathcal{O}(\delta) \right). \tag{E.11}
 \end{aligned}$$

E.1.2 AMPUTATED DIAGRAMS FOR LARGE INTERNAL MOMENTA

For large momenta we approximate the field to be massless and we use the two point functions of equations (7.24) and (7.25), which we write as

$$F(k, \tau_1, \tau_2) = \frac{H^2}{2} \sum_{i=1}^3 F_i(k, \tau_1, \tau_2), \tag{E.12}$$

$$F_1(k, \tau_1, \tau_2) = \frac{1}{k^3} \cos k \Delta\tau,$$

$$F_2(k, \tau_1, \tau_2) = \frac{1}{k^2} \Delta\tau \sin k \Delta\tau,$$

$$F_3(k, \tau_1, \tau_2) = \frac{1}{k} \tau_1 \tau_2 \cos k \Delta\tau,$$

with $\Delta\tau = \tau_1 - \tau_2$, and similarly

$$G^R(k, \tau_1, \tau_2) = \theta(\tau_1 - \tau_2) H^2 \sum_{i=1}^3 G_i^R(k, \tau_1, \tau_2), \tag{E.13}$$

$$G_1^R(k, \tau_1, \tau_2) = \frac{1}{k^3} \sin k \Delta\tau,$$

$$G_2^R(k, \tau_1, \tau_2) = \frac{-1}{k^2} \Delta\tau \cos k \Delta\tau,$$

$$G_3^R(k, \tau_1, \tau_2) = \frac{1}{k} \tau_1 \tau_2 \sin k \Delta\tau.$$

In the following calculations we use the definitions

$$\text{Si}(x) = \int_0^x dx' \frac{\sin x'}{x'}, \quad \text{Ci}(x) = - \int_x^\infty dx' \frac{\cos x'}{x'}, \tag{E.14}$$

which behave for small respectively large arguments as

$$\text{Si}(x) = x + \mathcal{O}(x^3), \quad \text{Ci}(x) = \frac{\pi}{2} - \frac{\cos x}{x} - \frac{\sin x}{x^2} + \mathcal{O}(x^{-3}), \tag{E.15}$$

$$\text{Ci}(x) = \gamma + \ln x - \frac{x^2}{4} + \mathcal{O}(x^4), \quad \text{Ci}(x) = \frac{\sin x}{x} - \frac{\cos x}{x^2} + \mathcal{O}(x^{-2}), \tag{E.16}$$

and the identities

$$\int_{p-k}^{p+k} dp' \frac{\sin p' \Delta\tau}{p'^2} = -\frac{\sin(p+k)\Delta\tau}{p+k} + \frac{\sin(p-k)\Delta\tau}{p-k} + \Delta\tau \left(\text{Ci}((p+k)\Delta\tau) - \text{Ci}((p-k)\Delta\tau) \right), \quad (\text{E.17})$$

$$\int_{p-k}^{p+k} dp' \frac{\cos p' \Delta\tau}{p'^2} = -\frac{\cos(p+k)\Delta\tau}{p+k} + \frac{\cos(p-k)\Delta\tau}{p-k} + \Delta\tau \left(\text{Si}((p+k)\Delta\tau) - \text{Si}((p-k)\Delta\tau) \right), \quad (\text{E.18})$$

$$\int_{p-k}^{p+k} dp' \sin p' \Delta\tau = \frac{-1}{\Delta\tau} (\cos(p+k)\Delta\tau - \cos(p-k)\Delta\tau) = \frac{2}{\Delta\tau} \sin k \Delta\tau \sin p \Delta\tau, \quad (\text{E.19})$$

$$\int_{p-k}^{p+k} dp' \cos p' \Delta\tau = \frac{1}{\Delta\tau} (\sin(p+k)\Delta\tau - \sin(p-k)\Delta\tau) = \frac{2}{\Delta\tau} \sin k \Delta\tau \cos p \Delta\tau. \quad (\text{E.20})$$

Next we calculate the contributions

$$\int_{M_{\text{cm}}}^{\Lambda a(\tau_2)} dp p F_i(p, \tau_1, \tau_2) \int_{p-k}^{p+k} dp' p' G_j^R(p', \tau_1, \tau_2), \quad (\text{E.21})$$

for i and j from 1 to 3:

#1: $F_1(p, \tau_1, \tau_2) G_1^R(p', \tau_1, \tau_2)$

$$\begin{aligned} & \int_{M_{\text{cm}}}^{\Lambda a(\tau_2)} dp \frac{\cos p \Delta\tau}{p^2} \int_{p-k}^{p+k} dp' \frac{\sin p' \Delta\tau}{p'^2} = \\ & \left[-\frac{\cos p \Delta\tau}{p} \left(-\frac{\sin(p+k)\Delta\tau}{p+k} + \frac{\sin(p-k)\Delta\tau}{p-k} + \Delta\tau \left(\text{Ci}((p+k)\Delta\tau) - \text{Ci}((p-k)\Delta\tau) \right) \right) \right]_{M_{\text{cm}}}^{\Lambda a(\tau_2)} + \\ & \int_{M_{\text{cm}}}^{\Lambda a(\tau_2)} dp \left\{ -\Delta\tau \frac{\sin p \Delta\tau}{p} \left(-\frac{\sin(p+k)\Delta\tau}{p+k} + \frac{\sin(p-k)\Delta\tau}{p-k} + \Delta\tau \left(\text{Ci}((p+k)\Delta\tau) - \text{Ci}((p-k)\Delta\tau) \right) \right) + \right. \\ & \left. \frac{\cos p \Delta\tau}{p} \left(\frac{\sin(p+k)\Delta\tau}{(p+k)^2} - \frac{\sin(p-k)\Delta\tau}{(p-k)^2} \right) \right\}, \quad (\text{E.22}) \end{aligned}$$

#2: $F_1(p, \tau_1, \tau_2)G_2^R(p', \tau_1, \tau_2)$

$$\begin{aligned}
 & - \Delta\tau \int_{M_{\text{cm}}}^{\Lambda a(\tau_2)} dp \frac{\cos p\Delta\tau}{p^2} \int_{p-k}^{p+k} dp' \frac{\cos p'\Delta\tau}{p'} = \\
 & \Delta\tau \left[\frac{\cos p\Delta\tau}{p} \left(\text{Ci}((p+k)\Delta\tau) - \text{Ci}((p-k)\Delta\tau) \right) \right]_{M_{\text{cm}}}^{\Lambda a(\tau_2)} + \\
 & \Delta\tau \int_{M_{\text{cm}}}^{\Lambda a(\tau_2)} dp \left\{ \Delta\tau \frac{\sin p\Delta\tau}{p} \left(\text{Ci}((p+k)\Delta\tau) - \text{Ci}((p-k)\Delta\tau) \right) + \right. \\
 & \quad \left. - \frac{\cos p\Delta\tau}{p} \left(\frac{\cos(p+k)\Delta\tau}{p+k} - \frac{\cos(p-k)\Delta\tau}{p-k} \right) \right\}, \quad (\text{E.23})
 \end{aligned}$$

#3: $F_1(p, \tau_1, \tau_2)G_3^R(p', \tau_1, \tau_2)$

$$\begin{aligned}
 & \tau_1\tau_2 \int_{M_{\text{cm}}}^{\Lambda a(\tau_2)} dp \frac{\cos p\Delta\tau}{p^2} \int_{p-k}^{p+k} dp' \sin p'\Delta\tau = \\
 & \frac{\tau_1\tau_2 \sin k\Delta\tau}{\Delta\tau} \int_{M_{\text{cm}}}^{\Lambda a(\tau_2)} dp \frac{\sin 2p\Delta\tau}{p^2} = \\
 & \frac{\tau_1\tau_2 \sin k\Delta\tau}{\Delta\tau} \left[-\frac{\sin 2p\Delta\tau}{p} + 2\Delta\tau \text{Ci}(2p\Delta\tau) \right]_{M_{\text{cm}}}^{\Lambda a(\tau_2)}, \quad (\text{E.24})
 \end{aligned}$$

#4: $F_2(p, \tau_1, \tau_2)G_1^R(p', \tau_1, \tau_2)$

$$\begin{aligned}
 & \Delta\tau \int_{M_{\text{cm}}}^{\Lambda a(\tau_2)} dp \frac{\sin p\Delta\tau}{p} \int_{p-k}^{p+k} dp' \frac{\sin p'\Delta\tau}{p'^2} = \\
 & \int_{M_{\text{cm}}}^{\Lambda a(\tau_2)} dp \Delta\tau \frac{\sin p\Delta\tau}{p} \left(-\frac{\sin(p+k)\Delta\tau}{p+k} + \frac{\sin(p-k)\Delta\tau}{p-k} + \right. \\
 & \quad \left. \Delta\tau \left(\text{Ci}((p+k)\Delta\tau) - \text{Ci}((p-k)\Delta\tau) \right) \right), \quad (\text{E.25})
 \end{aligned}$$

#5: $F_2(p, \tau_1, \tau_2)G_2^R(p', \tau_1, \tau_2)$

$$\begin{aligned}
 & - \Delta\tau^2 \int_{M_{\text{cm}}}^{\Lambda a(\tau_2)} dp \frac{\sin p\Delta\tau}{p} \int_{p-k}^{p+k} dp' \frac{\cos p'\Delta\tau}{p'} = \\
 & - \Delta\tau^2 \int_{M_{\text{cm}}}^{\Lambda a(\tau_2)} dp \frac{\sin p\Delta\tau}{p} \left(\text{Ci}((p+k)\Delta\tau) - \text{Ci}((p-k)\Delta\tau) \right), \quad (\text{E.26})
 \end{aligned}$$

#6: $F_2(p, \tau_1, \tau_2)G_3^R(p', \tau_1, \tau_2)$

$$\begin{aligned} \Delta\tau \tau_1 \tau_2 \int_{M_{\text{cm}}}^{\Lambda\alpha(\tau_2)} dp \frac{\sin p\Delta\tau}{p} \int_{p-k}^{p+k} dp' \sin p'\Delta\tau = \\ \tau_1 \tau_2 \sin k\Delta\tau \int_{M_{\text{cm}}}^{\Lambda\alpha(\tau_2)} dp \frac{1 - \cos 2p\Delta\tau}{p} = \\ \tau_1 \tau_2 \sin k\Delta\tau \left[\ln p - \text{Ci}(2p\Delta\tau) \right]_{M_{\text{cm}}}^{\Lambda\alpha(\tau_2)}, \end{aligned} \quad (\text{E.27})$$

#7: $F_3(p, \tau_1, \tau_2)G_1^R(p', \tau_1, \tau_2)$

$$\begin{aligned} \tau_1 \tau_2 \int_{M_{\text{cm}}}^{\Lambda\alpha(\tau_2)} dp \cos p\Delta\tau \int_{p-k}^{p+k} dp' \frac{\sin p'\Delta\tau}{p'^2} = \\ \tau_1 \tau_2 \int_{M_{\text{cm}}}^{\Lambda\alpha(\tau_2)} dp \cos p\Delta\tau \left(-\frac{\sin(p+k)\Delta\tau}{p+k} + \frac{\sin(p-k)\Delta\tau}{p-k} + \right. \\ \left. \Delta\tau \left(\text{Ci}((p+k)\Delta\tau) - \text{Ci}((p-k)\Delta\tau) \right) \right) = \\ -\frac{\tau_1 \tau_2}{2} \left[\sin k\Delta\tau \left(\ln(p^2 - k^2) - \text{Ci}(2(p+k)\Delta\tau) - \text{Ci}(2(p-k)\Delta\tau) \right) + \right. \\ \left. \cos k\Delta\tau \left(\text{Si}(2(p+k)\Delta\tau) - \text{Si}(2(p-k)\Delta\tau) \right) \right]_{M_{\text{cm}}}^{\Lambda\alpha(\tau_2)} + \\ \tau_1 \tau_2 \Delta\tau \int_{M_{\text{cm}}}^{\Lambda\alpha(\tau_2)} dp \cos p\Delta\tau \left(\text{Ci}((p+k)\Delta\tau) - \text{Ci}((p-k)\Delta\tau) \right), \end{aligned} \quad (\text{E.28})$$

#8: $F_3(p, \tau_1, \tau_2)G_2^R(p', \tau_1, \tau_2)$

$$\begin{aligned} -\tau_1 \tau_2 \Delta\tau \int_{M_{\text{cm}}}^{\Lambda\alpha(\tau_2)} dp \cos p\Delta\tau \int_{p-k}^{p+k} dp' \frac{\cos p'\Delta\tau}{p'} = \\ -\tau_1 \tau_2 \Delta\tau \int_{M_{\text{cm}}}^{\Lambda\alpha(\tau_2)} dp \cos p\Delta\tau \left(\text{Ci}((p+k)\Delta\tau) - \text{Ci}((p-k)\Delta\tau) \right), \end{aligned} \quad (\text{E.29})$$

#9: $F_3(p, \tau_1, \tau_2)G_3^R(p', \tau_1, \tau_2)$

$$\tau_1^2 \tau_2^2 \int_{M_{\text{cm}}}^{\Lambda\alpha(\tau_2)} dp \cos p\Delta\tau \int_{p-k}^{p+k} dp' \sin p'\Delta\tau = \frac{\tau_1^2 \tau_2^2}{\Delta\tau^2} \sin k\Delta\tau \left[\sin^2 p\Delta\tau \right]_{M_{\text{cm}}}^{\Lambda\alpha(\tau_2)}. \quad (\text{E.30})$$

Together this becomes

$$\begin{aligned}
 & \left[\frac{\cos p \Delta \tau}{p} \left(\frac{\sin(p+k)\Delta\tau}{p+k} - \frac{\sin(p-k)\Delta\tau}{p-k} \right) + \right. \\
 & \quad \frac{\tau_1 \tau_2 \sin k \Delta \tau}{2} \left(2 \text{Ci}(2p\Delta\tau) + \text{Ci}(2(p+k)\Delta\tau) + \text{Ci}(2(p-k)\Delta\tau) + \right. \\
 & \quad \ln \frac{p^2}{p^2 - k^2} - 2 \frac{\sin 2p\Delta\tau}{p\Delta\tau} \left. \right) - \frac{\tau_1 \tau_2}{2} \cos k \Delta \tau \left(\text{Si}(2(p+k)\Delta\tau) - \text{Si}(2(p-k)\Delta\tau) \right) + \\
 & \quad \left. \frac{\tau_1^2 \tau_2^2}{\Delta \tau^2} \sin k \Delta \tau \sin^2 p \Delta \tau \right]_{M_{\text{cm}}}^{\Lambda a(\tau_2)} + \\
 & \int_{M_{\text{cm}}}^{\Lambda a(\tau_2)} dp \frac{\cos p \Delta \tau}{p} \left\{ \frac{\sin(p+k)\Delta\tau}{(p+k)^2} - \frac{\sin(p-k)\Delta\tau}{(p-k)^2} + \right. \\
 & \quad \left. - \Delta \tau \left(\frac{\cos(p+k)\Delta\tau}{p+k} - \frac{\cos(p-k)\Delta\tau}{p-k} \right) \right\}. \quad (\text{E.31})
 \end{aligned}$$

For the upper limit the boundary term vanishes as $1/\Lambda^2$, except the last term which we will discuss below. The lower limit of the boundary term gives (where we use that $|M_{\text{cm}}\tau_i| \ll 1$)

$$\frac{2}{3} k \Delta \tau^3 - 2k\tau_1\tau_2 \Delta \tau \left(-2 + \gamma + \ln 2M_{\text{cm}}\Delta\tau \right) + \mathcal{O}(\tau_i^4). \quad (\text{E.32})$$

Using Mathematica, the integral in (E.31) becomes for $|M_{\text{cm}}\tau_i| \ll 1$

$$\frac{k\Delta\tau^3}{9} \left(8 - 6\gamma - 6 \ln 2M_{\text{cm}}\Delta\tau \right) + \mathcal{O}(\tau_i^4). \quad (\text{E.33})$$

Together equation (E.31) becomes

$$\begin{aligned}
 & \frac{2k}{3} (\tau_1^3 - \tau_2^3) \left(\frac{7}{3} - \gamma - \ln 2M_{\text{cm}}(\tau_1 - \tau_2) \right) - \frac{2}{3} k \tau_1 \tau_2 (\tau_1 - \tau_2) + \\
 & \quad \frac{\tau_1^2 \tau_2^2}{\Delta \tau^2} \sin k \Delta \tau \sin^2 \Lambda a(\tau_2) \Delta \tau + \mathcal{O}(\tau_i^4). \quad (\text{E.34})
 \end{aligned}$$

The term that contains the $\sin^2 \Lambda$ is logarithmically divergent for $\Lambda \rightarrow \infty$. This can be seen as follows. Consider the integral

$$\int_{-\infty}^{\infty} d\Delta\tau \theta(\Delta\tau) f(\Delta\tau) \frac{\sin^2 \Lambda a(\tau_2) \Delta \tau}{\Delta \tau} = \frac{1}{2} \int_0^{\infty} d\Delta\tau f(\Delta\tau) \frac{1 - \cos \left(\frac{-2\Lambda}{H} \frac{\Delta\tau}{\tau_1 - \Delta\tau} \right)}{\Delta \tau}, \quad (\text{E.35})$$

where $f(\Delta\tau)$ is a test function. The integral can be split into two integrals

$$\int_0^{\infty} = \lim_{\varepsilon \rightarrow 0} \int_{\varepsilon}^{\eta} + \int_{\eta}^{\infty}, \quad (\text{E.36})$$

where η is used as a regulator time, which we take to zero in the end, after taking the limit $\Lambda \rightarrow \infty$. In the first integral we can approximate

$$\frac{\Delta\tau}{\tau_1 - \Delta\tau} \approx \frac{\Delta\tau}{\tau_1}, \quad f(\Delta\tau) \approx f(0), \quad (\text{E.37})$$

so that it becomes

$$\begin{aligned} \lim_{\varepsilon \rightarrow 0} \int_{\varepsilon}^{\eta} d\Delta\tau f(0) \frac{1 - \cos\left(\frac{-2\Lambda}{H} \frac{\Delta\tau}{\tau_1}\right)}{\Delta\tau} = \\ \lim_{\varepsilon \rightarrow 0} f(0) \left(\ln \frac{\eta}{\varepsilon} - \text{Ci}\left(\frac{-2\Lambda\eta}{H\tau_1}\right) + \text{Ci}\left(\frac{-2\Lambda\varepsilon}{H\tau_1}\right) \right) = f(0) \left(\gamma + \ln \frac{-2\Lambda\eta}{H\tau_1} \right), \end{aligned} \quad (\text{E.38})$$

where we have taken $\text{Ci}(-2\Lambda\eta/H\tau_1) \rightarrow 0$, and $\text{Ci}(-2\Lambda\varepsilon/H\tau_1) \rightarrow \gamma + \ln(-2\Lambda\varepsilon/H\tau_1)$. The remaining integral is

$$\lim_{\Lambda \rightarrow \infty} \int_{\eta}^{\infty} d\Delta\tau f(\Delta\tau) \frac{1 - \cos\left(\frac{-2\Lambda}{H} \frac{\Delta\tau}{\tau_1 - \Delta\tau}\right)}{\Delta\tau} = \int_{\eta}^{\infty} d\Delta\tau \frac{f(\Delta\tau)}{\Delta\tau}, \quad (\text{E.39})$$

where the term with the cosine vanishes, provided that the test function $f(\Delta\tau)$ vanishes sufficiently fast as $\Delta\tau \rightarrow \infty$. Together we obtain for $\Lambda \rightarrow \infty$

$$\begin{aligned} \int_{-\infty}^{\infty} d\Delta\tau \theta(\Delta\tau) f(\Delta\tau) \frac{\sin^2 \Lambda a(\tau_2) \Delta\tau}{\Delta\tau} = \\ \int_{-\infty}^{\infty} d\Delta\tau f(\Delta\tau) \frac{1}{2} \left[\frac{\theta(-\eta + \Delta\tau)}{\Delta\tau} + \delta(\Delta\tau) \left(\gamma + \ln \frac{-2\Lambda\eta}{H\tau_1} \right) \right], \end{aligned} \quad (\text{E.40})$$

which is in the language of distributions

$$\theta(\Delta\tau) \frac{\sin^2 \Lambda a(\tau_2) \Delta\tau}{\Delta\tau} = \frac{1}{2} \left[\frac{\theta(-\eta + \Delta\tau)}{\Delta\tau} + \delta(\Delta\tau) \left(\gamma + \ln \frac{-2\Lambda\eta}{H\tau_1} \right) \right]. \quad (\text{E.41})$$

Using this result in equation (E.34), gathering the right prefactors and adding the contribution from the counterterm (E.4), we obtain for the large momentum contribution

$$\begin{aligned} \frac{i\lambda^2 \theta(\tau_1 - \tau_2)}{2(2\pi)^2 H^4 (\tau_1 \tau_2)^4} \left(\frac{2}{3} (\tau_1^3 - \tau_2^3) \left(\frac{7}{3} - \gamma - \ln 2M_{\text{cm}} \Delta\tau \right) - \frac{2}{3} \tau_1 \tau_2 (\tau_1 - \tau_2) + \right. \\ \left. \frac{(\tau_1 \tau_2)^2}{2} \left[\frac{\theta(-\eta + \Delta\tau)}{\Delta\tau} + \delta(\Delta\tau) \left(\gamma + \ln \frac{-2\mu\eta}{H\tau_1} \right) \right] \right). \end{aligned} \quad (\text{E.42})$$

E.1.3 ATTACHING THE EXTERNAL LINES

Adding the small and large momenta contributions, we obtain for the amputated diagrams A and D:

$$\begin{aligned}
 A_{\text{amp}}(k, \tau_1, \tau_2) + D_{\text{amp}}(k, \tau_1, \tau_2) &= \frac{i\lambda^2\theta(\tau_1 - \tau_2)}{6(2\pi)^2 H^4(\tau_1\tau_2)^4} \left((\tau_1^3 - \tau_2^3) \left(\frac{1}{\delta} + \frac{14}{3} - 2\gamma \right) + \right. \\
 &\quad \left. - 2\tau_1\tau_2(\tau_1 - \tau_2) + 2\tau_1^3 \ln \left| \frac{\tau_2}{2(\tau_1 - \tau_2)} \right| - 2\tau_2^3 \ln \left| \frac{\tau_1}{2(\tau_1 - \tau_2)} \right| + \right. \\
 &\quad \left. \frac{3}{2}(\tau_1\tau_2)^2 \left[\frac{\theta(-\eta + \tau_1 - \tau_2)}{\tau_1 - \tau_2} + \delta(\tau_1 - \tau_2) \left(\gamma + \ln \frac{-2\mu\eta}{H\tau_1} \right) \right] + \mathcal{O}(\tau_i^4) + \mathcal{O}(\delta) \right), \tag{E.43}
 \end{aligned}$$

where the dependence on M_{cm} has dropped out. The full correlation function is obtained by

$$-i \int_{\tau_H}^{\tau} d\tau_1 \int_{\tau_H}^{\tau} d\tau_2 G^R(k, \tau, \tau_1) F(k, \tau, \tau_2) \left(A_{\text{amp}}(k, \tau_1, \tau_2) + D_{\text{amp}}(k, \tau_1, \tau_2) \right). \tag{E.44}$$

Because the external momentum k is small, i.e. $|k\tau_i| \ll 1$, we can use the expanded versions of the two point functions (7.37), (7.38) (or the ones of (E.9), (E.10), but this gives only corrections of order $\mathcal{O}(\delta)$). Using the integrals

$$\int_{\tau_H}^{\tau} d\tau_1 \int_{\tau_H}^{\tau_1} d\tau_2 \frac{(\tau^3 - \tau_1^3)(\tau_1^3 - \tau_2^3)}{(\tau_1\tau_2)^4} = \frac{1}{3} \left(1 + 2 \ln \frac{\tau}{\tau_H} + \frac{3}{2} \ln^2 \frac{\tau}{\tau_H} \right) + \mathcal{O}\left(\frac{\tau}{\tau_H}\right), \tag{E.45}$$

$$\int_{\tau_H}^{\tau} d\tau_1 \int_{\tau_H}^{\tau_1} d\tau_2 \frac{(\tau^3 - \tau_1^3)(\tau_1 - \tau_2)}{(\tau_1\tau_2)^3} = -\frac{1}{12} \left(11 + 6 \ln \frac{\tau}{\tau_H} \right) + \mathcal{O}\left(\frac{\tau}{\tau_H}\right), \tag{E.46}$$

$$\begin{aligned}
 \int_{\tau_H}^{\tau} d\tau_1 \int_{\tau_H}^{\tau_1} d\tau_2 \frac{(\tau^3 - \tau_1^3)}{(\tau_1\tau_2)^4} \left(\tau_1^3 \ln \left| \frac{\tau_2}{2(\tau_1 - \tau_2)} \right| - \tau_2^3 \ln \left| \frac{\tau_1}{2(\tau_1 - \tau_2)} \right| \right) &= \\
 \frac{1}{18} \left(\frac{97}{6} - 18\zeta(3) - 2\pi^2 - 6 \ln 2 + (13 - 3\pi^2 - 12 \ln 2) \ln \frac{\tau}{\tau_H} + \right. \\
 \left. (3 - 9 \ln 2) \ln^2 \frac{\tau}{\tau_H} + 3 \ln^3 \frac{\tau}{\tau_H} \right) + \mathcal{O}\left(\frac{\tau}{\tau_H}\right), \tag{E.47}
 \end{aligned}$$

$$\begin{aligned}
 \int_{\tau_H}^{\tau} d\tau_1 \int_{\tau_H}^{\tau_1} d\tau_2 \frac{(\tau^3 - \tau_1^3)}{(\tau_1\tau_2)^2} \left[\frac{\theta(-\eta + \tau_1 - \tau_2)}{\tau_1 - \tau_2} + \delta(\tau_1 - \tau_2) \left(\gamma + \ln \frac{-2\mu\eta}{H\tau_1} \right) \right] &= \\
 \frac{1}{6} \left(8 - 2\gamma - \pi^2 - 2 \ln \frac{2\mu}{H} + 6 \left(1 - \gamma - \ln \frac{2\mu}{H} \right) \ln \frac{\tau}{\tau_H} \right) + \mathcal{O}\left(\frac{\tau}{\tau_H}\right), \tag{E.48}
 \end{aligned}$$

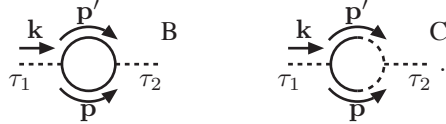
(recall that η is sent to zero), this becomes

$$\frac{\lambda^2}{36(2\pi)^2 k^3} \left\{ \frac{1}{3\delta} + \frac{194}{27} - \frac{7}{6}\gamma - \frac{17}{36}\pi^2 - \frac{2}{3}\ln 2 - 2\zeta(3) - \frac{1}{2}\ln \frac{2\mu}{H} + \right. \\ \left. \left(\frac{2}{3\delta} + \frac{127}{18} - \frac{17}{6}\gamma - \frac{1}{3}\pi^2 - \frac{4}{3}\ln 2 - \frac{3}{2}\ln \frac{2\mu}{H} \right) \ln \frac{\tau}{\tau_H} + \right. \\ \left. \left(\frac{1}{2\delta} + \frac{8}{3} - \gamma - \ln 2 \right) \ln^2 \frac{\tau}{\tau_H} + \frac{1}{3}\ln^3 \frac{\tau}{\tau_H} + \mathcal{O}\left(\frac{\tau}{\tau_H}\right) + \mathcal{O}(\delta) \right\}. \quad (\text{E.49})$$

There is an equal contribution from the diagram with τ_1 and τ_2 interchanged. Note that there is no dependence on $\ln k/\mu$ for $|k\tau| \ll 1$.

E.2 DIAGRAMS B AND C

The amputated versions of the diagrams with two external G^R propagators are



$$\begin{array}{ccc} \begin{array}{c} \text{B} \\ \text{---} \tau_1 \quad \text{---} \tau_2 \end{array} & \begin{array}{c} \text{C} \\ \text{---} \tau_1 \quad \text{---} \tau_2 \end{array} & \end{array} \quad (\text{E.50})$$

They translate to

$$\begin{aligned} B_{\text{amp}}(k, \tau_1, \tau_2) &= \frac{(-i\lambda)^2}{2H^8(\tau_1\tau_2)^4} \int \frac{d^3p d^3p'}{(2\pi)^3} \delta^3(\mathbf{k} - \mathbf{p} - \mathbf{p}') F(p', \tau_1, \tau_2) F(p, \tau_1, \tau_2) \\ &= \frac{-\lambda^2}{2(2\pi)^2 k H^8 (\tau_1 \tau_2)^4} \int_0^\infty dpp \int_{|p-k|}^{p+k} dp' p' F(p', \tau_1, \tau_2) F(p, \tau_1, \tau_2), \end{aligned} \quad (\text{E.51})$$

$$\begin{aligned} C_{\text{amp}}(k, \tau_1, \tau_2) &= \frac{(-i)^2 (-i\lambda)^2}{8H^8 (\tau_1 \tau_2)^4} \int \frac{d^3p d^3p'}{(2\pi)^3} \delta^3(\mathbf{k} - \mathbf{p} - \mathbf{p}') G^R(p', \tau_1, \tau_2) G^R(p, \tau_1, \tau_2) \\ &= \frac{\lambda^2}{8(2\pi)^2 k H^8 (\tau_1 \tau_2)^4} \int_0^\infty dpp \int_{|p-k|}^{p+k} dp' p' G^R(p', \tau_1, \tau_2) G^R(p, \tau_1, \tau_2), \end{aligned} \quad (\text{E.52})$$

where both diagrams have a factor $1/2$ for symmetry. Diagram C has an additional factor $1/4$ from the vertex with three dashed lines (7.29). We split the p integral again into a small momentum part and a large momentum part.

E.2.1 AMPUTATED DIAGRAMS FOR SMALL INTERNAL MOMENTA

For small internal momenta we use the expanded propagators (E.9) and (E.10).

Diagram B. The integral is

$$\begin{aligned} & \frac{-\lambda^2}{2(2\pi)^2 k H^8 (\tau_1 \tau_2)^4} \frac{H^4 (\tau_1 \tau_2)^{2\delta}}{4} \int_0^{M_{\text{cm}}} dp \int_{|p-k|}^{p+k} dp' \frac{(pp')^{2\delta}}{(pp')^2} = \\ & \frac{-\lambda^2 (\tau_1 \tau_2)^{2\delta}}{8(2\pi)^2 k H^4 (\tau_1 \tau_2)^4 (2\delta - 1)} \left(\int_0^k dp p^{-2+2\delta} ((p+k)^{-1+2\delta} - (k-p)^{-1+2\delta}) + \right. \\ & \left. \int_k^{M_{\text{cm}}} dp p^{-2+2\delta} ((p+k)^{-1+2\delta} - (p-k)^{-1+2\delta}) \right). \quad (\text{E.53}) \end{aligned}$$

The integral on the middle line of (E.53) is finite, but the individual parts are infrared divergent. Therefore we calculate the individual parts for $\delta > 1/2$, and in the end use analytic continuation to $\delta \ll 1$. The integrals are (using $p = kx$)

$$\begin{aligned} \int_0^1 dx x^{-2+2\delta} (1+x)^{-1+2\delta} &= \sum_{n=0}^{\infty} \frac{(-1)^n}{n!} \frac{\Gamma(1+n-2\delta)}{\Gamma(1-2\delta)} \int_0^1 dx x^{-2+n+2\delta} \\ &= -\frac{1}{2\delta} + \ln 2 + \mathcal{O}(\delta), \quad (\text{E.54}) \end{aligned}$$

$$\int_0^1 dx x^{-2+2\delta} (1-x)^{-1+2\delta} = B(-1+2\delta, 2\delta) = \frac{1}{\delta} - 2 + \mathcal{O}(\delta), \quad (\text{E.55})$$

$$\begin{aligned} \int_1^{M_{\text{cm}}/k} dx x^{-2+2\delta} (1+x)^{-1+2\delta} &= \int_{k/M_{\text{cm}}}^1 dy \frac{y^{1-4\delta}}{(1+y)^{1-2\delta}} \\ &= 1 - \frac{k}{M_{\text{cm}}} - \ln 2 + \ln \left(1 + \frac{k}{M_{\text{cm}}} \right) + \mathcal{O}(\delta), \quad (\text{E.56}) \end{aligned}$$

$$\begin{aligned} \int_1^{M_{\text{cm}}/k} dx x^{-2+2\delta} (x-1)^{-1+2\delta} &= \int_{k/M_{\text{cm}}}^1 dy \frac{y^{1-4\delta}}{(1-y)^{1-2\delta}} \\ &= \int_0^{1-k/M_{\text{cm}}} dz z^{-1+2\delta} (1-z) + \mathcal{O}(\delta) \\ &= \frac{1}{2\delta} - 1 + \frac{k}{M_{\text{cm}}} + \ln \left(1 - \frac{k}{M_{\text{cm}}} \right) + \mathcal{O}(\delta), \quad (\text{E.57}) \end{aligned}$$

where we have used analytic continuation in the first two integrals and $y = 1/x$ and $z = 1 - y$ in the latter two. The right hand side of equation (E.53) becomes

$$\begin{aligned} & \frac{-\lambda^2 (k^2 \tau_1 \tau_2)^{2\delta}}{8(2\pi)^2 k^3 H^4 (\tau_1 \tau_2)^4 (2\delta - 1)} \left(\frac{-2}{\delta} + 4 - 2 \frac{k}{M_{\text{cm}}} + \ln \frac{1+k/M_{\text{cm}}}{1-k/M_{\text{cm}}} + \mathcal{O}(\delta) \right) = \\ & \frac{-\lambda^2}{4(2\pi)^2 k^3 H^4 (\tau_1 \tau_2)^4} \left(\frac{1}{\delta} + \frac{k}{M_{\text{cm}}} - \frac{1}{2} \ln \frac{M_{\text{cm}} + k}{M_{\text{cm}} - k} + 2 \ln(k^2 \tau_1 \tau_2) + \mathcal{O}(\delta) \right). \quad (\text{E.58}) \end{aligned}$$

Diagram C. From equations (E.52) and (E.10) we see directly that diagram C does not give late time contributions and also does not have an infrared divergence.

E.2.2 AMPUTATED DIAGRAMS FOR LARGE INTERNAL MOMENTA

The contributions from large internal momenta can be calculated in a similar way as is used for diagram A in section E.1.2.

Diagram B. The sum of integrals

$$\sum_{i=1}^3 \sum_{j=1}^3 \int_{M_{\text{cm}}}^{\Lambda a(\tau_\beta)} dp p F_i(p, \tau_1, \tau_2) \int_{p-k}^{p+k} dp' p' F_j(p', \tau_1, \tau_2), \quad (\text{E.59})$$

(where $\tau_\beta = \tau_1, \tau_2$, depending on which time is earlier), is equal to

$$\begin{aligned} & \left[\frac{\cos p \Delta \tau}{p} \left(\frac{\cos(p+k)\Delta \tau}{p+k} - \frac{\cos(p-k)\Delta \tau}{p-k} \right) + \right. \\ & \quad - \tau_1 \tau_2 \sin k \Delta \tau \left(\text{Si}(2p \Delta \tau) + 2 \frac{\cos^2 p \Delta \tau}{p \Delta \tau} \right) + \\ & \quad \left. \frac{(\tau_1 \tau_2)^2}{\Delta \tau} \sin k \Delta \tau \left(p + \frac{\sin 2p \Delta \tau}{2 \Delta \tau} \right) \right]_{M_{\text{cm}}}^{\Lambda a(\tau_\beta)} + \\ & \int_{M_{\text{cm}}}^{\Lambda a(\tau_\beta)} dp \frac{\cos p \Delta \tau}{p} \left\{ \frac{\cos(p+k)\Delta \tau}{(p+k)^2} - \frac{\cos(p-k)\Delta \tau}{(p-k)^2} + \right. \\ & \quad \Delta \tau \left(\frac{\sin(p+k)\Delta \tau}{p+k} - \frac{\sin(p-k)\Delta \tau}{p-k} \right) + \\ & \quad \left. - p \tau_1 \tau_2 \left(\frac{\cos(p+k)\Delta \tau}{p+k} - \frac{\cos(p-k)\Delta \tau}{p-k} \right) \right\}. \quad (\text{E.60}) \end{aligned}$$

The only ultraviolet term comes from the last term of the boundary term and is, including the correct prefactor:

$$\frac{-\lambda^2 \sin k \Delta \tau}{8(2\pi)^2 k H^4 (\tau_1 \tau_2)^2 \Delta \tau} \left[p + \frac{\sin 2p \Delta \tau}{2 \Delta \tau} \right]_{M_{\text{cm}}}^{\Lambda a(\tau_\beta)}. \quad (\text{E.61})$$

The only term that gives late time contributions is the first line in the integral. It is

$$\frac{-\lambda^2}{4(2\pi)^2 k^3 H^4 (\tau_1 \tau_2)^4} \left(-\frac{k}{M_{\text{cm}}} + \frac{1}{2} \ln \frac{M_{\text{cm}} + k}{M_{\text{cm}} - k} + \mathcal{O}(\tau_i^2) \right). \quad (\text{E.62})$$

Diagram C. The sum of integrals

$$\sum_{i=1}^3 \sum_{j=1}^3 \int_{M_{\text{cm}}}^{\Lambda a(\tau_\beta)} dp p G_i^R(p, \tau_1, \tau_2) \int_{p-k}^{p+k} dp' p' G_j^R(p', \tau_1, \tau_2), \quad (\text{E.63})$$

is equal to

$$\begin{aligned} & \left[\frac{\sin p \Delta \tau}{p} \left(\frac{\sin(p+k)\Delta\tau}{p+k} - \frac{\sin(p-k)\Delta\tau}{p-k} \right) + \right. \\ & \quad \left. + \tau_1 \tau_2 \sin k \Delta \tau \left(3 \text{Si}(2p\Delta\tau) - 2 \frac{\sin^2 p \Delta \tau}{p \Delta \tau} \right) + \right. \\ & \quad \left. \frac{(\tau_1 \tau_2)^2}{\Delta \tau} \sin k \Delta \tau \left(p - \frac{\sin 2p \Delta \tau}{2 \Delta \tau} \right) \right]_{M_{\text{cm}}}^{\Lambda a(\tau_\beta)} + \\ & \int_{M_{\text{cm}}}^{\Lambda a(\tau_\beta)} dp \frac{\sin p \Delta \tau}{p} \left\{ \frac{\sin(p+k)\Delta\tau}{(p+k)^2} - \frac{\sin(p-k)\Delta\tau}{(p-k)^2} + \right. \\ & \quad \left. - \Delta \tau \left(\frac{\cos(p+k)\Delta\tau}{p+k} - \frac{\cos(p-k)\Delta\tau}{p-k} \right) - \right. \\ & \quad \left. p \tau_1 \tau_2 \left(\frac{\sin(p+k)\Delta\tau}{p+k} - \frac{\sin(p-k)\Delta\tau}{p-k} \right) \right\}. \quad (\text{E.64}) \end{aligned}$$

Only the last term of the boundary term is ultraviolet divergent:

$$\frac{\lambda^2 \theta(\tau_1 - \tau_2) \sin k \Delta \tau}{8(2\pi)^2 k H^4 (\tau_1 \tau_2)^2 \Delta \tau} \left[p - \frac{\sin 2p \Delta \tau}{2 \Delta \tau} \right]_{M_{\text{cm}}}^{\Lambda a(\tau_\beta)}. \quad (\text{E.65})$$

The diagram with the vertices interchanged gives the same result, except that $\theta(\tau_1 - \tau_2)$ is replaced by $\theta(\tau_2 - \tau_1)$. There are no further late time contributions.

Ultraviolet divergences. The ultraviolet divergent terms of diagrams B (E.61), C (E.65), and C with the vertices interchanged, add up to

$$\left[\frac{-\lambda^2 \sin k \Delta \tau}{8(2\pi)^2 k H^4 (\tau_1 \tau_2)^2 \Delta \tau} \frac{\sin 2p \Delta \tau}{\Delta \tau} \right]_{M_{\text{cm}}}^{\Lambda a(\tau_\beta)}, \quad (\text{E.66})$$

which is finite and does not give late time contributions.

E.2.3 ATTACHING THE EXTERNAL LINES

Adding the small and large momenta contributions, we obtain for the amputated diagrams B and C:

$$B_{\text{amp}}(k, \tau_1, \tau_2) + C_{\text{amp}}(k, \tau_1, \tau_2) = \frac{-\lambda^2}{4(2\pi)^2 k^3 H^4 (\tau_1 \tau_2)^4} \left(\frac{1}{\delta} + 2 \ln(k^2 \tau_1 \tau_2) + \mathcal{O}(\tau_i) + \mathcal{O}(\delta) \right), \quad (\text{E.67})$$

where the dependence on M_{cm} has dropped out. The full correlation function is obtained by

$$- \int_{\tau_H}^{\tau} d\tau_1 \int_{\tau_H}^{\tau} d\tau_2 G^R(k, \tau, \tau_1) G^R(k, \tau, \tau_2) \left(B_{\text{amp}}(k, \tau_1, \tau_2) + C_{\text{amp}}(k, \tau_1, \tau_2) \right). \quad (\text{E.68})$$

Because the external momentum k is small, i.e. $|k\tau_i| \ll 1$, we can use the expanded version of the G^R propagator (7.38) (or the one of (E.10), but this gives only corrections of $\mathcal{O}(\delta)$). Using the integrals

$$\begin{aligned} \int_{\tau_H}^{\tau} d\tau_1 \int_{\tau_H}^{\tau} d\tau_2 \frac{(\tau^3 - \tau_1^3)(\tau^3 - \tau_2^3)}{(\tau_1 \tau_2)^4} &= \frac{1}{9} + \frac{2}{3} \ln \frac{\tau}{\tau_H} + \ln^2 \frac{\tau}{\tau_H} + \mathcal{O}\left(\frac{\tau}{\tau_H}\right), \quad (\text{E.69}) \\ \int_{\tau_H}^{\tau} d\tau_1 \int_{\tau_H}^{\tau} d\tau_2 \frac{(\tau^3 - \tau_1^3)(\tau^3 - \tau_2^3)}{(\tau_1 \tau_2)^4} \ln(k^2 \tau_1 \tau_2) &= \frac{1}{27} \left(2 + 6 \ln(-k\tau_H) + \right. \\ &12 \left(1 + 3 \ln(-k\tau_H) \right) \ln \frac{\tau}{\tau_H} + 27 \left(1 + 2 \ln(-k\tau_H) \right) \ln^2 \frac{\tau}{\tau_H} + 27 \ln^3 \frac{\tau}{\tau_H} \left. \right) + \\ &\mathcal{O}\left(\frac{\tau}{\tau_H}\right), \quad (\text{E.70}) \end{aligned}$$

this becomes

$$\begin{aligned} \frac{\lambda^2}{36(2\pi)^2 k^3} \left(\frac{1}{9\delta} + \frac{4}{27} + \frac{4}{9} \ln(-k\tau_H) + \left(\frac{2}{3\delta} + \frac{8}{9} + \frac{8}{3} \ln(-k\tau_H) \right) \ln \frac{\tau}{\tau_H} + \right. \\ \left. \left(\frac{1}{\delta} + 2 + 4 \ln(-k\tau_H) \right) \ln^2 \frac{\tau}{\tau_H} + 2 \ln^3 \frac{\tau}{\tau_H} + \mathcal{O}\left(\frac{\tau}{\tau_H}\right) + \mathcal{O}(\delta) \right). \quad (\text{E.71}) \end{aligned}$$

BIBLIOGRAPHY

- [1] E. W. Kolb and M. S. Turner, *The early universe*, Addison-Wesley (Frontiers in physics), Redwood City (USA), 1988.
- [2] S. Dodelson, *Modern cosmology*, Academic Pr., Amsterdam (Netherlands), 2003.
- [3] V. Mukhanov, *Physical foundations of cosmology*, Cambridge University Press, 2005.
- [4] *COBE website*, <http://lambda.gsfc.nasa.gov/product/cobe>.
- [5] *WMAP website*, <http://lambda.gsfc.nasa.gov/product/map>.
- [6] D. H. Lyth and A. Riotto, *Particle physics models of inflation and the cosmological density perturbation*, *Phys. Rept.* **314** (1999) 1–146 [hep-ph/9807278].
- [7] A. R. Liddle and D. H. Lyth, *Cosmological inflation and large-scale structure*, Cambridge University Press, 2000.
- [8] B. A. Bassett, S. Tsujikawa and D. Wands, *Inflation dynamics and reheating*, *Rev. Mod. Phys.* **78** (2006) 537–589 [astro-ph/0507632].
- [9] **WMAP** Collaboration, D. N. Spergel *et. al.*, *Wilkinson Microwave Anisotropy Probe (WMAP) three year results: Implications for cosmology*, *Astrophys. J. Suppl.* **170** (2007) 377 [astro-ph/0603449].
- [10] A. D. Linde, *Chaotic inflation*, *Phys. Lett.* **B129** (1983) 177–181.
- [11] A. D. Linde, *Eternal extended inflation and graceful exit from old inflation without Jordan-Brans-Dicke*, *Phys. Lett.* **B249** (1990) 18–26.
- [12] A. D. Linde, *Axions in inflationary cosmology*, *Phys. Lett.* **B259** (1991) 38–47.
- [13] A. D. Linde, *Hybrid inflation*, *Phys. Rev.* **D49** (1994) 748–754 [astro-ph/9307002].

- [14] L. F. Abbott, E. Farhi and M. B. Wise, *Particle production in the new inflationary cosmology*, *Phys. Lett.* **B117** (1982) 29.
- [15] A. Albrecht, P. J. Steinhardt, M. S. Turner and F. Wilczek, *Reheating an inflationary universe*, *Phys. Rev. Lett.* **48** (1982) 1437.
- [16] L. Kofman, A. D. Linde and A. A. Starobinsky, *Reheating after inflation*, *Phys. Rev. Lett.* **73** (1994) 3195–3198 [hep-th/9405187].
- [17] Y. Shtanov, J. H. Traschen and R. H. Brandenberger, *Universe reheating after inflation*, *Phys. Rev.* **D51** (1995) 5438–5455 [hep-ph/9407247].
- [18] D. Boyanovsky, M. D’Attanasio, H. J. de Vega, R. Holman and D. S. Lee, *Reheating and thermalization: Linear versus nonlinear relaxation*, *Phys. Rev.* **D52** (1995) 6805–6827 [hep-ph/9507414].
- [19] D. I. Kaiser, *Post inflation reheating in an expanding universe*, *Phys. Rev.* **D53** (1996) 1776–1783 [astro-ph/9507108].
- [20] L. Kofman, A. D. Linde and A. A. Starobinsky, *Towards the theory of reheating after inflation*, *Phys. Rev.* **D56** (1997) 3258–3295 [hep-ph/9704452].
- [21] D. Boyanovsky, H. J. de Vega, R. Holman and J. F. J. Salgado, *Analytic and numerical study of preheating dynamics*, *Phys. Rev.* **D54** (1996) 7570–7598 [hep-ph/9608205].
- [22] S. Y. Khlebnikov and I. I. Tkachev, *Resonant decay of bose condensates*, *Phys. Rev. Lett.* **79** (1997) 1607–1610 [hep-ph/9610477].
- [23] J. Garcia-Bellido and A. D. Linde, *Preheating in hybrid inflation*, *Phys. Rev.* **D57** (1998) 6075–6088 [hep-ph/9711360].
- [24] A. Rajantie, P. M. Saffin and E. J. Copeland, *Electroweak preheating on a lattice*, *Phys. Rev.* **D63** (2001) 123512 [hep-ph/0012097].
- [25] G. N. Felder *et. al.*, *Dynamics of symmetry breaking and tachyonic preheating*, *Phys. Rev. Lett.* **87** (2001) 011601 [hep-ph/0012142].
- [26] G. N. Felder, L. Kofman and A. D. Linde, *Tachyonic instability and dynamics of spontaneous symmetry breaking*, *Phys. Rev.* **D64** (2001) 123517 [hep-th/0106179].
- [27] J. Garcia-Bellido, M. Garcia Perez and A. Gonzalez-Arroyo, *Symmetry breaking and false vacuum decay after hybrid inflation*, *Phys. Rev.* **D67** (2003) 103501 [hep-ph/0208228].
- [28] W.-M. Yao *et al.*, *Review of Particle Physics*, *Journal of Physics G* **33** (2006) 1.

- [29] A. G. Cohen, D. B. Kaplan and A. E. Nelson, *Progress in electroweak baryogenesis*, *Ann. Rev. Nucl. Part. Sci.* **43** (1993) 27–70 [hep-ph/9302210].
- [30] V. A. Rubakov and M. E. Shaposhnikov, *Electroweak baryon number non-conservation in the early universe and in high-energy collisions*, *Usp. Fiz. Nauk* **166** (1996) 493–537 [hep-ph/9603208].
- [31] M. Trodden, *Electroweak baryogenesis*, *Rev. Mod. Phys.* **71** (1999) 1463–1500 [hep-ph/9803479].
- [32] M. Dine and A. Kusenko, *The origin of the matter-antimatter asymmetry*, *Rev. Mod. Phys.* **76** (2004) 1 [hep-ph/0303065].
- [33] J. M. Cline, *Baryogenesis*, hep-ph/0609145.
- [34] A. D. Sakharov, *Violation of CP invariance, C asymmetry, and baryon asymmetry of the universe*, *Pisma Zh. Eksp. Teor. Fiz.* **5** (1967) 32–35.
- [35] M. Fukugita and T. Yanagida, *Baryogenesis Without Grand Unification*, *Phys. Lett.* **B174** (1986) 45.
- [36] V. A. Kuzmin, V. A. Rubakov and M. E. Shaposhnikov, *On the anomalous electroweak baryon number nonconservation in the early universe*, *Phys. Lett.* **B155** (1985) 36.
- [37] M. Kobayashi and T. Maskawa, *CP violation in the renormalizable theory of weak interaction*, *Prog. Theor. Phys.* **49** (1973) 652–657.
- [38] F. Csikor, Z. Fodor and J. Heitger, *Endpoint of the hot electroweak phase transition*, *Phys. Rev. Lett.* **82** (1999) 21–24 [hep-ph/9809291].
- [39] M. Gurtler, E.-M. Ilgenfritz and A. Schiller, *Where the electroweak phase transition ends*, *Phys. Rev.* **D56** (1997) 3888–3895 [hep-lat/9704013].
- [40] K. Kajantie, M. Laine, K. Rummukainen and M. E. Shaposhnikov, *Is there a hot electroweak phase transition at $m(H) \gtrsim m(W)$?*, *Phys. Rev. Lett.* **77** (1996) 2887–2890 [hep-ph/9605288].
- [41] K. Kajantie, M. Laine, K. Rummukainen and M. E. Shaposhnikov, *A non-perturbative analysis of the finite T phase transition in $SU(2) \times U(1)$ electroweak theory*, *Nucl. Phys.* **B493** (1997) 413–438 [hep-lat/9612006].
- [42] K. Rummukainen, M. Tsy-pin, K. Kajantie, M. Laine and M. E. Shaposhnikov, *The universality class of the electroweak theory*, *Nucl. Phys.* **B532** (1998) 283–314 [hep-lat/9805013].

- [43] F. Karsch, T. Neuhaus, A. Patkos and J. Rank, *Critical Higgs mass and temperature dependence of gauge boson masses in the SU(2) gauge-Higgs model*, *Nucl. Phys. Proc. Suppl.* **53** (1997) 623–625 [hep-lat/9608087].
- [44] K. Kajantie, M. Laine, J. Peisa, K. Rummukainen and M. E. Shaposhnikov, *The electroweak phase transition in a magnetic field*, *Nucl. Phys.* **B544** (1999) 357–373 [hep-lat/9809004].
- [45] **LEP Working Group for Higgs boson searches** Collaboration, R. Barate *et al.*, *Search for the standard model Higgs boson at LEP*, *Phys. Lett.* **B565** (2003) 61–75 [hep-ex/0306033].
- [46] M. E. Shaposhnikov, *Possible appearance of the baryon asymmetry of the universe in an electroweak theory*, *JETP Lett.* **44** (1986) 465–468.
- [47] M. E. Shaposhnikov, *Baryon asymmetry of the universe in standard electroweak theory*, *Nucl. Phys.* **B287** (1987) 757–775.
- [48] C. Jarlskog, *Commutator of the quark mass matrices in the standard electroweak model and a measure of maximal CP violation*, *Phys. Rev. Lett.* **55** (1985) 1039.
- [49] J. M. Cline and P.-A. Lemieux, *Electroweak phase transition in two Higgs doublet models*, *Phys. Rev.* **D55** (1997) 3873–3881 [hep-ph/9609240].
- [50] L. Fromme, S. J. Huber and M. Seniuch, *Baryogenesis in the two-Higgs doublet model*, *JHEP* **11** (2006) 038 [hep-ph/0605242].
- [51] C. Grojean, G. Servant and J. D. Wells, *First-order electroweak phase transition in the standard model with a low cutoff*, *Phys. Rev.* **D71** (2005) 036001 [hep-ph/0407019].
- [52] J. Garcia-Bellido, D. Y. Grigoriev, A. Kusenko and M. E. Shaposhnikov, *Non-equilibrium electroweak baryogenesis from preheating after inflation*, *Phys. Rev.* **D60** (1999) 123504 [hep-ph/9902449].
- [53] L. M. Krauss and M. Trodden, *Baryogenesis below the electroweak scale*, *Phys. Rev. Lett.* **83** (1999) 1502–1505 [hep-ph/9902420].
- [54] L. Knox and M. S. Turner, *Inflation at the electroweak scale*, *Phys. Rev. Lett.* **70** (1993) 371–374 [astro-ph/9209006].
- [55] G. German, G. G. Ross and S. Sarkar, *Low-scale inflation*, *Nucl. Phys.* **B608** (2001) 423–450 [hep-ph/0103243].
- [56] E. J. Copeland, D. Lyth, A. Rajantie and M. Trodden, *Hybrid inflation and baryogenesis at the TeV scale*, *Phys. Rev.* **D64** (2001) 043506 [hep-ph/0103231].

- [57] B. van Tent, J. Smit and A. Tranberg, *Electroweak-scale inflation, inflaton-Higgs mixing and the scalar spectral index*, *JCAP* **0407** (2004) 003 [hep-ph/0404128].
- [58] J. Smit and A. Tranberg, *Chern-simons number asymmetry from CP violation at electroweak tachyonic preheating*, *JHEP* **12** (2002) 020 [hep-ph/0211243].
- [59] J.-I. Skullerud, J. Smit and A. Tranberg, *W and Higgs particle distributions during electroweak tachyonic preheating*, *JHEP* **08** (2003) 045 [hep-ph/0307094].
- [60] J. Garcia-Bellido, M. Garcia-Perez and A. Gonzalez-Arroyo, *Chern-Simons production during preheating in hybrid inflation models*, *Phys. Rev.* **D69** (2004) 023504 [hep-ph/0304285].
- [61] A. Tranberg and J. Smit, *Baryon asymmetry from electroweak tachyonic preheating*, *JHEP* **11** (2003) 016 [hep-ph/0310342].
- [62] M. van der Meulen, D. Sexty, J. Smit and A. Tranberg, *Chern-Simons and winding number in a tachyonic electroweak transition*, *JHEP* **02** (2006) 029 [hep-ph/0511080].
- [63] A. Tranberg and J. Smit, *Simulations of cold electroweak baryogenesis: Dependence on Higgs mass and strength of CP-violation*, *JHEP* **08** (2006) 012 [hep-ph/0604263].
- [64] A. Tranberg, J. Smit and M. Hindmarsh, *Simulations of cold electroweak baryogenesis: Finite time quenches*, *JHEP* **01** (2007) 034 [hep-ph/0610096].
- [65] A. Diaz-Gil, J. Garcia-Bellido, M. G. Perez and A. Gonzalez-Arroyo, *Magnetic field production during preheating at the electroweak scale*, [arXiv:0712.4263](https://arxiv.org/abs/0712.4263) [hep-ph].
- [66] M. E. Peskin and D. V. Schroeder, *An introduction to quantum field theory*, Addison-Wesley, Reading (USA), 1995.
- [67] S. Weinberg, *The quantum theory of fields. vol. 1: Foundations*, Cambridge University Press, 1995.
- [68] S. Weinberg, *The quantum theory of fields. vol. 2: Modern applications*, Cambridge University Press, 1996.
- [69] J. Smit, *Student seminar theoretical physics 2001/02*, <http://staff.science.uva.nl/~jsmit>.
- [70] G. 't Hooft, *Symmetry breaking through Bell-Jackiw anomalies*, *Phys. Rev. Lett.* **37** (1976) 8–11.

- [71] J. S. Bell and R. Jackiw, *A PCAC puzzle: $\pi^0 \rightarrow \gamma \gamma$ in the sigma model*, *Nuovo Cim.* **A60** (1969) 47–61.
- [72] S. L. Adler, *Axial vector vertex in spinor electrodynamics*, *Phys. Rev.* **177** (1969) 2426–2438.
- [73] N. S. Manton, *Topology in the Weinberg-Salam theory*, *Phys. Rev.* **D28** (1983) 2019.
- [74] F. R. Klinkhamer and N. S. Manton, *A saddle point solution in the Weinberg-Salam theory*, *Phys. Rev.* **D30** (1984) 2212.
- [75] A. Riotto and M. Trodden, *Recent progress in baryogenesis*, *Ann. Rev. Nucl. Part. Sci.* **49** (1999) 35–75 [hep-ph/9901362].
- [76] K. Kajantie, M. Laine, K. Rummukainen and M. E. Shaposhnikov, *The electroweak phase transition: A non-perturbative analysis*, *Nucl. Phys.* **B466** (1996) 189–258 [hep-lat/9510020].
- [77] M. B. Gavela, P. Hernandez, J. Orloff and O. Pene, *Standard model CP violation and baryon asymmetry*, *Mod. Phys. Lett.* **A9** (1994) 795–810 [hep-ph/9312215].
- [78] P. Huet and E. Sather, *Electroweak baryogenesis and standard model CP violation*, *Phys. Rev.* **D51** (1995) 379–394 [hep-ph/9404302].
- [79] J. Garcia-Bellido, M. Garcia Perez and A. Gonzalez-Arroyo, *Symmetry breaking and false vacuum decay after hybrid inflation*, *Phys. Rev.* **D67** (2003) 103501 [hep-ph/0208228].
- [80] J. Smit, *Effective CP violation in the standard model*, *JHEP* **09** (2004) 067 [hep-ph/0407161].
- [81] N. Turok and J. Zadrozny, *Dynamical generation of baryons at the electroweak transition*, *Phys. Rev. Lett.* **65** (1990) 2331–2334.
- [82] N. Turok and J. Zadrozny, *Electroweak baryogenesis in the two doublet model*, *Nucl. Phys.* **B358** (1991) 471–493.
- [83] A. Lue, K. Rajagopal and M. Trodden, *Semi-analytical approaches to local electroweak baryogenesis*, *Phys. Rev.* **D56** (1997) 1250–1261 [hep-ph/9612282].
- [84] N. Turok, *Global texture as the origin of cosmic structure*, *Phys. Rev. Lett.* **63** (1989) 2625.
- [85] G. H. Derrick, *Comments on nonlinear wave equations as models for elementary particles*, *J. Math. Phys.* **5** (1964) 1252–1254.

- [86] T. Prokopec, A. Sornborger and R. H. Brandenberger, *Texture collapse*, *Phys. Rev.* **D45** (1992) 1971–1981.
- [87] T. Asaka, W. Buchmuller and L. Covi, *False vacuum decay after inflation*, *Phys. Lett.* **B510** (2001) 271–276 [hep-ph/0104037].
- [88] A. Arrizabalaga, J. Smit and A. Tranberg, *Tachyonic preheating using 2PI - 1/N dynamics and the classical approximation*, *JHEP* **10** (2004) 017 [hep-ph/0409177].
- [89] G. J. Stephens, *Unraveling critical dynamics: The formation and evolution of topological textures*, *Phys. Rev.* **D61** (2000) 085002 [hep-ph/9911247].
- [90] M. Broadhead and J. McDonald, *Simulations of the end of supersymmetric hybrid inflation and non-topological soliton formation*, *Phys. Rev.* **D72** (2005) 043519 [hep-ph/0503081].
- [91] E. Farhi, N. Graham, V. Khemani, R. Markov and R. Rosales, *An oscillon in the SU(2) gauged Higgs model*, *Phys. Rev.* **D72** (2005) 101701 [hep-th/0505273].
- [92] J. Baacke and S. Junker, *Quantum fluctuations around the electroweak sphaleron*, *Phys. Rev.* **D49** (1994) 2055–2073 [hep-ph/9308310].
- [93] A. Hernandez, T. Konstandin and M. G. Schmidt, *Effective action in a general chiral model: Next to leading order derivative expansion in the worldline method*, arXiv:0708.0759 [hep-th].
- [94] L. L. Salcedo, *Derivative expansion for the effective action of chiral gauge fermions: The normal parity component*, *Eur. Phys. J.* **C20** (2001) 147–159 [hep-th/0012166].
- [95] L. L. Salcedo, *Derivative expansion for the effective action of chiral gauge fermions: The abnormal parity component*, *Eur. Phys. J.* **C20** (2001) 161–184 [hep-th/0012174].
- [96] T. Konstandin, T. Prokopec and M. G. Schmidt, *Axial currents from CKM matrix CP violation and electroweak baryogenesis*, *Nucl. Phys.* **B679** (2004) 246–260 [hep-ph/0309291].
- [97] G. R. Farrar and M. E. Shaposhnikov, *Baryon asymmetry of the universe in the minimal standard model*, *Phys. Rev. Lett.* **70** (1993) 2833–2836 [hep-ph/9305274].
- [98] G. R. Farrar and M. E. Shaposhnikov, *Baryon asymmetry of the universe in the standard electroweak theory*, *Phys. Rev.* **D50** (1994) 774 [hep-ph/9305275].

- [99] G. R. Farrar and M. E. Shaposhnikov, *Note added to 'baryon asymmetry of the universe in the standard model'*, [hep-ph/9406387](https://arxiv.org/abs/hep-ph/9406387).
- [100] M. B. Gavela, P. Hernandez, J. Orloff, O. Pene and C. Quimbay, *Standard model CP violation and baryon asymmetry. part 2: Finite temperature*, *Nucl. Phys.* **B430** (1994) 382–426 [[hep-ph/9406289](https://arxiv.org/abs/hep-ph/9406289)].
- [101] *Planck website*, <http://www.rssd.esa.int/Planck>.
- [102] S. Weinberg, *Quantum contributions to cosmological correlations*, *Phys. Rev.* **D72** (2005) 043514 [[hep-th/0506236](https://arxiv.org/abs/hep-th/0506236)].
- [103] S. Weinberg, *Quantum contributions to cosmological correlations. II: Can these corrections become large?*, *Phys. Rev.* **D74** (2006) 023508 [[hep-th/0605244](https://arxiv.org/abs/hep-th/0605244)].
- [104] M. S. Sloth, *On the one loop corrections to inflation and the CMB anisotropies*, *Nucl. Phys.* **B748** (2006) 149–169 [[astro-ph/0604488](https://arxiv.org/abs/astro-ph/0604488)].
- [105] M. S. Sloth, *On the one loop corrections to inflation. II: The consistency relation*, *Nucl. Phys.* **B775** (2007) 78–94 [[hep-th/0612138](https://arxiv.org/abs/hep-th/0612138)].
- [106] A. Bilandzic and T. Prokopec, *Quantum radiative corrections to slow-roll inflation*, *Phys. Rev.* **D76** (2007) 103507 [[arXiv:0704.1905](https://arxiv.org/abs/astro-ph/0704.1905) [[astro-ph](https://arxiv.org/abs/astro-ph)]].
- [107] C. T. Byrnes, K. Koyama, M. Sasaki and D. Wands, *Diagrammatic approach to non-Gaussianity from inflation*, *JCAP* **0711** (2007) 027 [[arXiv:0705.4096](https://arxiv.org/abs/astro-ph/0705.4096) [[hep-th](https://arxiv.org/abs/hep-th)]].
- [108] I. Zaballa, Y. Rodriguez and D. H. Lyth, *Higher order contributions to the primordial non-Gaussianity*, *JCAP* **0606** (2006) 013 [[astro-ph/0603534](https://arxiv.org/abs/astro-ph/0603534)].
- [109] M. van der Meulen and J. Smit, *Classical approximation to quantum cosmological correlations*, *JCAP* **0711** (2007) 023 [[arXiv:0707.0842](https://arxiv.org/abs/astro-ph/0707.0842) [[hep-th](https://arxiv.org/abs/hep-th)]].
- [110] V. F. Mukhanov, H. A. Feldman and R. H. Brandenberger, *Theory of cosmological perturbations. Part 1. Classical perturbations. Part 2. Quantum theory of perturbations. Part 3. Extensions*, *Phys. Rept.* **215** (1992) 203–333.
- [111] C. Gordon, D. Wands, B. A. Bassett and R. Maartens, *Adiabatic and entropy perturbations from inflation*, *Phys. Rev.* **D63** (2001) 023506 [[astro-ph/0009131](https://arxiv.org/abs/astro-ph/0009131)].
- [112] R. Bean, J. Dunkley and E. Pierpaoli, *Constraining isocurvature initial conditions with WMAP 3-year data*, *Phys. Rev.* **D74** (2006) 063503 [[astro-ph/0606685](https://arxiv.org/abs/astro-ph/0606685)].
- [113] R. Trotta, *The isocurvature fraction after WMAP 3-year data*, *Mon. Not. Roy. Astron. Soc. Lett.* **375** (2007) L26–L30 [[astro-ph/0608116](https://arxiv.org/abs/astro-ph/0608116)].

- [114] N. D. Birrell and P. C. W. Davies, *Quantum fields in curved space*, Cambridge University Press, 1982.
- [115] S. W. Hawking, *Black hole explosions*, *Nature* **248** (1974) 30–31.
- [116] J. M. Maldacena, *Non-Gaussian features of primordial fluctuations in single field inflationary models*, *JHEP* **05** (2003) 013 [astro-ph/0210603].
- [117] R. Arnowitt, S. Deser and C. W. Misner, *The dynamics of general relativity*, in *Gravitation: An Introduction to Current Research*, edited by L. Witten, (Wiley, New York, 1962), pp 227-265 [gr-qc/0405109].
- [118] D. H. Lyth, K. A. Malik and M. Sasaki, *A general proof of the conservation of the curvature perturbation*, *JCAP* **0505** (2005) 004 [astro-ph/0411220].
- [119] A. R. Liddle, A. Mazumdar and F. E. Schunck, *Assisted inflation*, *Phys. Rev.* **D58** (1998) 061301 [astro-ph/9804177].
- [120] S. Dimopoulos, S. Kachru, J. McGreevy and J. G. Wacker, *N-flation*, hep-th/0507205.
- [121] D. H. Lyth and D. Wands, *Generating the curvature perturbation without an inflaton*, *Phys. Lett.* **B524** (2002) 5–14 [hep-ph/0110002].
- [122] T. Moroi and T. Takahashi, *Effects of cosmological moduli fields on cosmic microwave background*, *Phys. Lett.* **B522** (2001) 215–221 [hep-ph/0110096].
- [123] K. Enqvist and M. S. Sloth, *Adiabatic CMB perturbations in pre big bang string cosmology*, *Nucl. Phys.* **B626** (2002) 395–409 [hep-ph/0109214].
- [124] A. A. Starobinsky, *Stochastic de Sitter (inflationary) stage in the early universe*, in *Field Theory, Quantum Gravity and Strings (Lecture Notes in Physics vol 246)*, editors H.J. De Vega and N. Sanchez (Springer, Berlin, 1986), pp 107-126.
- [125] A. A. Starobinsky and J. Yokoyama, *Equilibrium state of a selfinteracting scalar field in the de sitter background*, *Phys. Rev.* **D50** (1994) 6357–6368 [astro-ph/9407016].
- [126] G. I. Rigopoulos, E. P. S. Shellard and B. J. W. van Tent, *A simple route to non-Gaussianity in inflation*, *Phys. Rev.* **D72** (2005) 083507 [astro-ph/0410486].
- [127] G. I. Rigopoulos, E. P. S. Shellard and B. J. W. van Tent, *Non-linear perturbations in multiple-field inflation*, *Phys. Rev.* **D73** (2006) 083521 [astro-ph/0504508].
- [128] G. I. Rigopoulos, E. P. S. Shellard and B. W. van Tent, *Large non-Gaussianity in multiple-field inflation*, *Phys. Rev.* **D73** (2006) 083522 [astro-ph/0506704].

-
- [129] G. I. Rigopoulos, E. P. S. Shellard and B. J. W. van Tent, *Quantitative bispectra from multifield inflation*, *Phys. Rev.* **D76** (2007) 083512 [astro-ph/0511041].
- [130] R. P. Woodard, *A leading logarithm approximation for inflationary quantum field theory*, *Nucl. Phys. Proc. Suppl.* **148** (2005) 108–119 [astro-ph/0502556].
- [131] N. C. Tsamis and R. P. Woodard, *Stochastic quantum gravitational inflation*, *Nucl. Phys.* **B724** (2005) 295–328 [gr-qc/0505115].
- [132] T. Prokopec, N. C. Tsamis and R. P. Woodard, *Stochastic inflationary scalar electrodynamics*, arXiv:0707.0847 [gr-qc].
- [133] M. Sasaki and E. D. Stewart, *A general analytic formula for the spectral index of the density perturbations produced during inflation*, *Prog. Theor. Phys.* **95** (1996) 71–78 [astro-ph/9507001].
- [134] D. H. Lyth and Y. Rodriguez, *The inflationary prediction for primordial non-Gaussianity*, *Phys. Rev. Lett.* **95** (2005) 121302 [astro-ph/0504045].
- [135] A. Chambers and A. Rajantie, *Lattice calculation of non-gaussianity from preheating*, arXiv:0710.4133 [astro-ph].
- [136] N. Bartolo, E. Komatsu, S. Matarrese and A. Riotto, *Non-Gaussianity from inflation: Theory and observations*, *Phys. Rept.* **402** (2004) 103–266 [astro-ph/0406398].
- [137] J. M. Bardeen, *Gauge invariant cosmological perturbations*, *Phys. Rev.* **D22** (1980) 1882–1905.
- [138] F. Bernardeau and J.-P. Uzan, *Non-Gaussianity in multi-field inflation*, *Phys. Rev.* **D66** (2002) 103506 [hep-ph/0207295].
- [139] F. Bernardeau and J.-P. Uzan, *Inflationary models inducing non-Gaussian metric fluctuations*, *Phys. Rev.* **D67** (2003) 121301 [astro-ph/0209330].
- [140] K. Enqvist and A. Vaihkonen, *Non-Gaussian perturbations in hybrid inflation*, *JCAP* **0409** (2004) 006 [hep-ph/0405103].
- [141] D. H. Lyth and Y. Rodriguez, *Non-Gaussianity from the second-order cosmological perturbation*, *Phys. Rev.* **D71** (2005) 123508 [astro-ph/0502578].
- [142] F. Vernizzi and D. Wands, *Non-Gaussianities in two-field inflation*, *JCAP* **0605** (2006) 019 [astro-ph/0603799].
- [143] L. E. Allen, S. Gupta and D. Wands, *Non-Gaussian perturbations from multi-field inflation*, *JCAP* **0601** (2006) 006 [astro-ph/0509719].

- [144] H.-C. Lee, M. Sasaki, E. D. Stewart, T. Tanaka and S. Yokoyama, *A new delta N formalism for multi-component inflation*, *JCAP* **0510** (2005) 004 [astro-ph/0506262].
- [145] S. A. Kim and A. R. Liddle, *Nflation: Non-Gaussianity in the horizon-crossing approximation*, *Phys. Rev.* **D74** (2006) 063522 [astro-ph/0608186].
- [146] C. T. Byrnes, M. Sasaki and D. Wands, *The primordial trispectrum from inflation*, *Phys. Rev.* **D74** (2006) 123519 [astro-ph/0611075].
- [147] D. Seery and J. E. Lidsey, *Non-Gaussianity from the inflationary trispectrum*, *JCAP* **0701** (2007) 008 [astro-ph/0611034].
- [148] L. Alabidi, *Non-Gaussianity for a two component hybrid model of inflation*, *JCAP* **0610** (2006) 015 [astro-ph/0604611].
- [149] D. Seery, J. E. Lidsey and M. S. Sloth, *The inflationary trispectrum*, *JCAP* **0701** (2007) 027 [astro-ph/0610210].
- [150] T. Battefeld and R. Easther, *Non-Gaussianities in multi-field inflation*, *JCAP* **0703** (2007) 020 [astro-ph/0610296].
- [151] D. Battefeld and T. Battefeld, *Non-Gaussianities in N-flaton*, *JCAP* **0705** (2007) 012 [hep-th/0703012].
- [152] K.-Y. Choi, L. M. H. Hall and C. van de Bruck, *Spectral running and non-Gaussianity from slow-roll inflation in generalised two-field models*, *JCAP* **0702** (2007) 029 [astro-ph/0701247].
- [153] S. Yokoyama, T. Suyama and T. Tanaka, *Primordial non-Gaussianity in multi-scalar slow-roll inflation*, [arXiv:0705.3178](https://arxiv.org/abs/0705.3178) [astro-ph].
- [154] D. H. Lyth and D. Seery, *Classicality of the primordial perturbations*, [astro-ph/0607647](https://arxiv.org/abs/astro-ph/0607647).
- [155] E. Calzetta and B. L. Hu, *Closed time path functional formalism in curved space-time: Application to cosmological back reaction problems*, *Phys. Rev.* **D35** (1987) 495.
- [156] E. Calzetta and B. L. Hu, *Nonequilibrium quantum fields: Closed time path effective action, Wigner function and Boltzmann equation*, *Phys. Rev.* **D37** (1988) 2878.
- [157] D. Polarski and A. A. Starobinsky, *Semiclassicality and decoherence of cosmological perturbations*, *Class. Quant. Grav.* **13** (1996) 377–392 [gr-qc/9504030].

- [158] C. Kiefer, D. Polarski and A. A. Starobinsky, *Quantum-to-classical transition for fluctuations in the early universe*, *Int. J. Mod. Phys. D* **7** (1998) 455–462 [gr-qc/9802003].
- [159] C. Kiefer, I. Lohmar, D. Polarski and A. A. Starobinsky, *Pointer states for primordial fluctuations in inflationary cosmology*, *Class. Quant. Grav.* **24** (2007) 1699–1718 [astro-ph/0610700].
- [160] P. Martineau, *On the decoherence of primordial fluctuations during inflation*, *Class. Quant. Grav.* **24** (2007) 5817–5834 [astro-ph/0601134].
- [161] C. P. Burgess, R. Holman and D. Hoover, *On the decoherence of primordial fluctuations during inflation*, astro-ph/0601646.
- [162] T. Prokopec and G. I. Rigopoulos, *Decoherence from Isocurvature Perturbations in Inflation*, *JCAP* **0711** (2007) 029 [astro-ph/0612067].
- [163] N. C. Tsamis and R. P. Woodard, *Strong infrared effects in quantum gravity*, *Ann. Phys.* **238** (1995) 1–82.
- [164] N. C. Tsamis and R. P. Woodard, *The quantum gravitational back-reaction on inflation*, *Annals Phys.* **253** (1997) 1–54 [hep-ph/9602316].
- [165] V. K. Onemli and R. P. Woodard, *Super-acceleration from massless, minimally coupled ϕ^4* , *Class. Quant. Grav.* **19** (2002) 4607 [gr-qc/0204065].
- [166] T. Brunier, V. K. Onemli and R. P. Woodard, *Two loop scalar self-mass during inflation*, *Class. Quant. Grav.* **22** (2005) 59–84 [gr-qc/0408080].
- [167] V. K. Onemli and R. P. Woodard, *Quantum effects can render $w < -1$ on cosmological scales*, *Phys. Rev. D* **70** (2004) 107301 [gr-qc/0406098].
- [168] E. O. Kahya and V. K. Onemli, *Quantum Stability of a $w_j - 1$ Phase of Cosmic Acceleration*, *Phys. Rev. D* **76** (2007) 043512 [gr-qc/0612026].
- [169] T. Prokopec, O. Tornkvist and R. P. Woodard, *One loop vacuum polarization in a locally de Sitter background*, *Ann. Phys.* **303** (2003) 251–274 [gr-qc/0205130].
- [170] T. Prokopec and R. P. Woodard, *Production of massless fermions during inflation*, *JHEP* **10** (2003) 059 [astro-ph/0309593].
- [171] T. Prokopec, N. C. Tsamis and R. P. Woodard, *Two loop scalar bilinears for inflationary SQED*, *Class. Quant. Grav.* **24** (2007) 201–230 [gr-qc/0607094].
- [172] D. Boyanovsky *et. al.*, *Scalar field dynamics in Friedman Robertson Walker spacetimes*, *Phys. Rev. D* **56** (1997) 1939–1957 [hep-ph/9703327].

- [173] D. Boyanovsky and H. J. de Vega, *Dynamical renormalization group approach to relaxation in quantum field theory*, *Ann. Phys.* **307** (2003) 335–371 [hep-ph/0302055].
- [174] D. Boyanovsky and H. J. de Vega, *Particle decay in inflationary cosmology*, *Phys. Rev.* **D70** (2004) 063508 [astro-ph/0406287].
- [175] D. Boyanovsky, H. J. de Vega and N. G. Sanchez, *Particle decay during inflation: Self-decay of inflaton quantum fluctuations during slow roll*, *Phys. Rev.* **D71** (2005) 023509 [astro-ph/0409406].
- [176] D. Boyanovsky, H. J. de Vega and N. G. Sanchez, *Quantum corrections to slow roll inflation and new scaling of superhorizon fluctuations*, *Nucl. Phys.* **B747** (2006) 25–54 [astro-ph/0503669].
- [177] K. Chaicherdsakul, *Quantum cosmological correlations in an inflating universe: Can fermion and gauge fields loops give a scale free spectrum?*, *Phys. Rev.* **D75** (2007) 063522 [hep-th/0611352].
- [178] G. Aarts and J. Smit, *Classical approximation for time-dependent quantum field theory: Diagrammatic analysis for hot scalar fields*, *Nucl. Phys.* **B511** (1998) 451–478 [hep-ph/9707342].
- [179] P. R. Anderson, W. Eaker, S. Habib, C. Molina-Paris and E. Mottola, *Attractor states and infrared scaling in de sitter space*, *Phys. Rev.* **D62** (2000) 124019 [gr-qc/0005102].
- [180] P. R. Anderson, C. Molina-Paris and E. Mottola, *Short distance and initial state effects in inflation: Stress tensor and decoherence*, *Phys. Rev.* **D72** (2005) 043515 [hep-th/0504134].
- [181] M. Musso, *A new diagrammatic representation for correlation functions in the in-in formalism*, hep-th/0611258.
- [182] G. Aarts and J. Smit, *Finiteness of hot classical scalar field theory and the plasmon damping rate*, *Phys. Lett.* **B393** (1997) 395–402 [hep-ph/9610415].
- [183] S.-P. Miao and R. P. Woodard, *Leading log solution for inflationary Yukawa*, *Phys. Rev.* **D74** (2006) 044019 [gr-qc/0602110].
- [184] L. R. W. Abramo and R. P. Woodard, *One loop back reaction on power law inflation*, *Phys. Rev.* **D60** (1999) 044011 [astro-ph/9811431].
- [185] G. Aarts, B.-J. Nauta and C. G. van Weert, *Divergences in real-time classical field theories at non- zero temperature*, *Phys. Rev.* **D61** (2000) 105002 [hep-ph/9911463].

- [186] M. Abramowitz and I. A. Stegun (eds), *Handbook of Mathematical Functions with Formulas, Graphs and Mathematical Tables*, (Dover, New York, 1965), ISBN 0-486-61272-4.

SUMMARY

Throughout the course of time there have been many different ideas about cosmology, which is the study of the development of the universe on the largest scales. Nowadays the consensus is that the universe has reached its current state after a long period of expansion and cooling down. This idea is supported by ample observational evidence. Fred Hoyle, a scientist who was critical of the model of an expanding universe, described it derisively in a BBC radio show in 1950 as “*this Big Bang model*”, a term which has eventually become the name of this model.

There have also been many different ideas about the fundamental building blocks of nature. The branch of modern science that investigates nature at the smallest scales is called high energy physics or elementary particle physics. Particles are collided in accelerators, and the particles that are created in this process are studied. All the elementary particles and their interactions discovered in this way, are described very precisely by a quantum field theory called the Standard Model of particle physics. Despite the fact that the Standard Model explains the experimental data very well, there are indications that it is not yet complete.

Even though cosmology deals with the largest scales and high energy physics with the smallest, these two fields are connected. Many of the indications that the Standard Model is incomplete come from cosmology. An example that plays an important role in this thesis is inflation. This is a period in the early universe in which space expanded at an accelerated rate (in contrast with the decelerated expansion that occurred afterwards). From cosmology there are strong arguments that a period of inflation has occurred, but it seems impossible to explain this using the laws of the Standard Model. Apparently some extra ingredients have to be added. Other examples of the interconnection of cosmology and high energy physics are dark matter, dark energy and baryogenesis. This interconnection implies that cosmology provides an interesting alternative way to investigate the fundamental laws of nature.

This has only become a realistic possibility due to the many developments in cosmology over the past decades. New technologies, such as telescopes on satellites and large arrays

of detectors on earth, are providing large amounts of precise data. These developments changed the character of cosmology into a precision science. Expectations are that these developments will continue in the future and that cosmology will become more and more interesting for high energy physics.

In this thesis two subjects on the border between cosmology and high energy physics are treated. These are described more precisely in the following.

COLD ELECTROWEAK BARYOGENESIS

The first part of this thesis deals with the matter–anti-matter asymmetry. For every charged particle in the Standard Model there is a corresponding anti-particle with the opposite charge but otherwise identical characteristics. When a particle meets its anti-particle, they annihilate each other and radiation is emitted. Because we seldom see particle annihilation in everyday life, we know that there are nearly no anti-particles. There are also no indications of large amounts of anti-matter elsewhere in the universe. This leads us to conclude that there is a matter–anti-matter asymmetry. The process by which such an asymmetry is created is called baryogenesis.

It is not easy to determine whether or not such a process could have occurred within the laws of the Standard Model. For baryogenesis different numbers of particles and anti-particles have to be created, and there has to be a bias in favor of particles. Moreover, baryogenesis has to take place in a state that deviates strongly from thermal equilibrium. The Standard Model satisfies these conditions qualitatively in a scenario that is called *Electroweak Baryogenesis*. But quantitative analyses show that the asymmetry produced in this scenario is far too small. Therefore it is not possible to explain baryogenesis using purely Standard Model physics.

Over the course of time many other baryogenesis scenarios have been proposed, based on extensions of the Standard Model. One of these is *Cold Electroweak Baryogenesis*, which is based on a small extension of the Standard Model in which only an inflaton field is added. The interaction between the inflaton field and the fields of the Standard Model is such that it is possible for baryogenesis to take place directly after inflation, when the universe is still cold.

In the first part of this thesis the Cold Electroweak Baryogenesis model is studied more precisely. In chapter 3 the mechanism of particle production is studied using numerical simulations. The main conclusion is that certain field configurations, called ‘*half-knots*’, play an important role. These occur in the initial conditions, but can also be created later on. Those created later are likely to play a role in the generation of the asymmetry in this model.

In chapter 4 the possible degree of the asymmetry is investigated. This investigation leads

to the expectation that the asymmetry in Cold Electroweak baryogenesis is comparable to that of the original model of Electroweak Baryogenesis and therefore not large enough. Apparently this extension of the Standard Model by only an inflaton field is not sufficient to explain the asymmetry.

QUANTUM COSMOLOGICAL CORRELATIONS

The second part of the thesis deals with density fluctuations in the early universe. From observations of the background radiation (the radiation that was emitted approximately 380 000 years after the Big Bang) we know that the matter in the universe was distributed very homogeneously at that time: fluctuations in the density were smaller than the average density by a factor of about 100 000. Under the influence of gravity these fluctuations have grown into the structure we observe today: stars, galaxies, clusters of galaxies and structures on even larger scales.

The question is where the first small density fluctuations come from. It is generally assumed that they were generated by amplification of vacuum fluctuations during inflation. This effect, which applies to fluctuations with a large wavelength, is similar to the Hawking radiation that is emitted by black holes.

The observed fluctuations are characterized by correlation functions. Current observations indicate that their distribution is close to Gaussian, i.e. they are completely characterized by their two point function, and that the power of the fluctuations is nearly scale-independent. This corresponds to what one would expect for fluctuations generated during inflation. It will be interesting to see if more precise observations will lead to corrections to this distribution, because these corrections may teach us lessons about the physics of inflation.

For this reason a lot of effort is being put into the calculation of these *quantum cosmological correlations* generated in different models of inflation, in order to compare them to observations. These calculations use techniques from non-equilibrium quantum field theory and are rather complicated. Often, a part of the calculation is simplified by using classical field theory. One expects this to be a good approximation for a number of reasons.

In chapter 7 a toy model is used to study these calculations more precisely. For this model the calculations (in quantum field theory) are formulated in such a way that they can easily be compared to those in classical field theory. The main conclusion is that a calculation in classical field theory can indeed be a good approximation of the corresponding one in quantum field theory, but that some higher order corrections cannot be reproduced. In addition we find that there is a certain freedom in defining the classical field theory and we discuss how this can be resolved. A detailed calculation is given as example.

SAMENVATTING

In de loop der tijden zijn er zeer uiteenlopende ideeën geweest over kosmologie, de studie naar de ontwikkeling van het heelal op de grootste schalen in ruimte en tijd. Tegenwoordig is de wetenschappelijke consensus dat het heelal in zijn huidige toestand is gekomen na een lange periode van uitdijning en afkoeling, wat ondersteund wordt door een ruime verscheidenheid aan waarnemingen. In een radioshow van de BBC in 1950 gebruikte Fred Hoyle, een wetenschapper die kritisch tegenover het model van een uitdijend heelal stond, de spottende beschrijving “*this Big Bang model.*” Sindsdien is de naam Big Bang, in het Nederlands vertaald met oerknal, als geuzennaam in gebruik gebleven.

Hiernaast is ook altijd veel nagedacht over de fundamentele bouwstenen van de natuur. De tak van wetenschap die onderzoek doet naar de allerkleinste schalen is de hoge energie fysica (ook wel elementaire deeltjesfysica genoemd). In versnellers worden deeltjes met grote snelheden met elkaar in botsing gebracht en worden de deeltjes die hierbij vrijkomen bestudeerd. Alle elementaire deeltjes en wisselwerkingen die op deze manier zijn ontdekt worden met grote precisie beschreven door een quantumveldentheorie met de naam Standaardmodel. Ondanks het feit dat het Standaardmodel alle experimentele data goed kan verklaren, zijn er allerlei aanwijzingen die doen vermoeden dat het niet compleet is.

Hoewel kosmologie over de grootste schalen gaat en hoge energie fysica over de kleinste schalen, zijn deze vakgebieden toch met elkaar verbonden. Veel van de aanwijzingen dat het Standaardmodel incompleet is komen uit de kosmologie. Een voorbeeld daarvan, dat ook een belangrijke rol speelt in dit proefschrift, is inflatie. Dit is een periode in het vroege heelal waarin de ruimte versneld is uitgedijd (in tegenstelling tot de vertraagde uitdijning die daarna plaatsvond). Er zijn sterke kosmologische argumenten dat er zo'n periode is geweest, maar het lijkt onmogelijk om inflatie binnen de wetten van het Standaardmodel te verklaren. Blijkbaar moeten er nieuwe ingrediënten worden toegevoegd. Ook donkere materie, donkere energie en baryogenese zijn voorbeelden van de verwevenheid van kosmologie en hoge energie fysica. Kosmologie is dus, naast de deeltjesversnellers, een interessante manier om onderzoek te doen naar de fundamentele natuurwetten.

Dit is pas echt mogelijk geworden door de snelle ontwikkeling die de kosmologie in de

laatste paar decennia heeft doorgemaakt. Nieuwe technologieën, zoals telescopen op satellieten en grote arrays van meetinstrumenten op aarde, leveren een omvangrijke stroom aan nauwkeurige meetgegevens op. Hierdoor is de kosmologie veranderd in een precisiewetenschap. De verwachting is dat deze ontwikkeling zich voortzet in de toekomst en dat kosmologie daardoor steeds interessanter wordt voor de hoge energie fysica.

In dit proefschrift worden twee onderwerpen op het grensvlak van kosmologie en hoge energie fysica behandeld, die hieronder nader worden beschreven.

KOUDE ELECTROZWAKKE BARYOGENESE

Het eerste deel van het proefschrift gaat over de asymmetrie tussen materie en antimaterie. Voor elk geladen deeltje in het Standaardmodel is er ook een anti-deeltje met een tegenovergestelde lading, maar met voor het overige dezelfde eigenschappen. Als een deeltje zijn anti-deeltje ontmoet, verdwijnen beide onder uitzending van straling. Omdat er in de wereld om ons heen niet vaak deeltjes plotseling verdwijnen, weten we dat er bijna geen anti-deeltjes zijn. Ook verder bij ons vandaan in het heelal zijn er geen aanwijzingen voor grote aantallen anti-deeltjes. Er is dus een asymmetrie tussen materie (deeltjes) en anti-materie (anti-deeltjes). Het proces waarin deze asymmetrie is gecreëerd heet baryogenese.

Het is niet eenvoudig om vast te stellen of baryogenese kan hebben plaatsgevonden binnen de wetten van het Standaardmodel. Voor baryogenese moeten er processen plaats kunnen vinden waarin verschillende aantallen deeltjes en anti-deeltjes worden gecreëerd en daarbij moet er een voorkeur zijn voor deeltjes boven anti-deeltjes. Bovendien moet het plaatsvinden in een toestand die ver uit thermisch evenwicht is. Op kwalitatief niveau kan het Standaardmodel aan al deze eisen voldoen in een scenario dat *electrozwakke baryogenese* heet. Maar kwantitatieve analyses laten zien dat de geproduceerde asymmetrie in electrozwakke baryogenese veel te klein is. Blijkbaar kan baryogenese niet binnen de fysica van het Standaardmodel verklaard worden.

In de loop van de tijd zijn er veel alternatieve modellen voor baryogenese bedacht, gebaseerd op uitbreidingen van het Standaardmodel. Eén daarvan, *koude electrozwakke baryogenese*, is gebaseerd op een kleine uitbreiding van het Standaardmodel waarin slechts een inflaton veld wordt toegevoegd. De wisselwerking tussen dit veld en de velden van het Standaardmodel is zodanig dat baryogenese direct na inflatie, als het heelal nog koud is, plaats kan vinden.

In het eerste deel van dit proefschrift wordt het model van koude electrozwakke baryogenese nader bestudeerd. Het mechanisme waarmee deeltjes en anti-deeltjes worden geproduceerd, wordt in hoofdstuk 3 onderzocht met behulp van numerieke simulaties. De belangrijkste conclusie die daar getrokken wordt is dat bepaalde veldconfiguraties, zoge-

naamde ‘*half-knots*,’ een belangrijke rol spelen. Deze configuraties kunnen al voorkomen in de begincondities, maar kunnen ook pas later ontstaan. Vooral de versies die later ontstaan zijn waarschijnlijk belangrijk voor het creëren van een asymmetrie in dit model.

In hoofdstuk 4 wordt onderzocht of de geproduceerde asymmetrie groot genoeg zou kunnen zijn. De conclusie is dat verwacht kan worden dat de asymmetrie in koude elektrozwakke baryogenese vergelijkbaar klein is als die in het oorspronkelijke model van elektrozwakke baryogenese, en dus niet groot genoeg is. Blijkbaar is de hier gebruikte toevoeging aan het Standaardmodel niet voldoende om de asymmetrie te verklaren.

QUANTUM KOSMOLOGISCHE CORRELATIES

Het tweede deel van het proefschrift gaat over dichtheidsfluctuaties in het vroege heelal. Uit waarnemingen van de achtergrondstraling (de straling die ongeveer 380 000 jaar na de oerknal werd uitgezonden) weten we dat vroeger de materie in het heelal zeer homogeen verdeeld was: de fluctuaties in de dichtheid waren 100 000 keer zo klein als de gemiddelde dichtheid. Onder invloed van de zwaartekracht zijn deze fluctuaties in de loop van de tijd gegroeid en is het heelal steeds klonteriger geworden. Op deze manier zijn uiteindelijk de sterren, sterrenstelsels, clusters van sterrenstelsels en nog grotere structuren, die we tegenwoordig waarnemen, gegroeid.

De vraag is nu waar de eerste, kleine dichtheidsfluctuaties vandaan kwamen. In de kosmologie wordt meestal aangenomen dat deze fluctuaties zijn veroorzaakt tijdens een periode van inflatie. Het blijkt namelijk dat tijdens inflatie vacuümfluctuaties versterkt worden als de golflengte van de fluctuaties groot is. Dit effect is vergelijkbaar met de Hawking straling die door zwarte gaten wordt uitgezonden.

De waargenomen fluctuaties in de achtergrondstraling worden gekarakteriseerd door correlatiefuncties. Uit deze correlatiefuncties kan tot nu toe worden afgeleid dat de fluctuaties in goede benadering Gaussisch verdeeld zijn, d.w.z. dat ze volledig door hun tweepuntsfunctie zijn bepaald, en dat het vermogen van de fluctuaties bijna schaalonafhankelijk is. Dit is in overeenstemming met wat men zou verwachten als de fluctuaties tijdens inflatie zijn veroorzaakt. Het wordt echt interessant als de waarnemingen nauwkeuriger worden en er correcties op deze verdeling zullen worden gevonden, omdat deze correcties meer inzicht kunnen geven in de fysica van inflatie.

Daarom wordt er veel moeite gedaan om deze *quantum kosmologische correlaties* te berekenen uitgaande van verschillende modellen van inflatie, om deze uiteindelijk te vergelijken met de waarnemingen. Dit zijn ingewikkelde berekeningen waarvoor niet-evenwichtsquantumveldentheorie nodig is. Om zo’n berekening te versimpelen wordt vaak een gedeelte van de berekening gedaan met behulp van klassieke veldentheorie. Er zijn allerlei redenen om aan te nemen dat dit een goede benadering oplevert.

In hoofdstuk 7 wordt een versimpeld model gebruikt om deze berekeningen nader te bestuderen. Voor dit model worden de berekeningen (in quantumveldentheorie) geformuleerd op een manier dat ze makkelijk te vergelijken zijn met klassieke veldentheorie. De belangrijkste conclusie is dat berekeningen in klassieke veldentheorie inderdaad goede benaderingen kunnen zijn voor die in quantumveldentheorie, maar dat sommige hogere orde correcties niet gereproduceerd kunnen worden. Verder vinden we dat er een bepaalde vrijheid is in het definiëren van de klassieke veldentheorie en we bespreken hoe dit opgelost kan worden. Als voorbeeld is een berekening volledig uitgewerkt.

DANKWOORD

Allereerst gaat mijn dank uit naar mijn promotor Jan Smit die mij de mogelijkheid heeft gegeven dit proefschrift te schrijven. Ik heb grote waardering voor zijn vele wijze woorden, het feit dat hij altijd beschikbaar is, en zijn eindeloze geduld. Ook bedank ik Pierre van Baal die mijn interesse in de hoge energie fysica heeft gewekt.

Especially in my first year as PhD student, but also afterwards, I have often collaborated with Anders Tranberg, who is always good-humoured and enthusiastic. I thank him for the many times that I could ask him for information and assistance, and for his detailed and constructive comments on this thesis. Thanks also to Dénes Sexty for the collaboration.

In het begin van het onderzoek dat heeft geleid tot het tweede deel van dit proefschrift, heb ik veelvuldig en op een prettige manier gediscussieerd met Leo Kampmeijer, Koenraad Schalm en Jan Pieter van der Schaar. Ook na deze periode heb ik nog vaak kunnen profiteren van hun kennis en hulp. Met Leo heb ik bovendien regelmatig de dagelijkse besommeringen doorgenomen. Hiervoor mijn dank.

In mijn tijd op het Instituut voor Theoretische Fysica heb ik twee kamergenoten gehad: Ioannis Papadimitriou en Sheer El-Showk. Ik bedank beiden voor de gezelligheid, discussies en hulp bij allerlei dingen. Sheer heeft bovendien altijd een goed gevulde voorraadkast en heeft mij ook veelvuldig geholpen met het Engels.

Verder bedank ik alle andere collega's en oud-collega's op het Instituut voor Theoretische Fysica voor de prettige werksfeer. In het bijzonder noem ik Leo van den Horn die betrokken is geweest bij de meeste van mijn onderwijs-activiteiten, en altijd geïnteresseerd is gebleven in mijn reilen en zeilen; Alejandro Arrizabalaga die een belangrijke rol heeft gespeeld bij het maken van de drie-dimensionale plaatjes in deel I; en Rutger Boels aan wie ik mijn huisvesting te danken heb.

Voor het ontwerpen van de omslag bedank ik Haakon Brouwer, en voor het uitgebreid becommentariëren van de samenvatting bedank ik Robert Noordam en Erikjan Cuperus.

Tenslotte bedank ik mijn zusjes en paranimfen Hiske en Froukje, en mijn ouders, voor het lezen van de samenvatting, maar bovenal voor hun onvoorwaardelijke steun.